Scientific Report No. 109

DESIGN AND ANALYSIS OF SERIES-FED ARRAYS OF GAP-COUPLED RECTANGULAR MICROSTRIP PATCHES

by

Abdelaziz Benalla and K.C. Gupta

Electromagnetics Laboratory
Department of Electrical and Computer Engineering
Campus Box 425
University of Colorado
Boulder, Colorado 80309-0425

September 1992

ACKNOWLEDGEMENTS

The research work presented in this report has been supported by the Department of Navy, Naval Weapons Center, China Lake (California) under Research Contract No. N60530-89-C-0311 entitled, "Control of the Fractional Power Radiated by Two-Port Patches in a LInear Series-Fed Array of Microstrip Antennas" awarded to the University of Colorado during the period September 1989 through March 1993. Along with the software documentation report being prepared separately, this scientific report constitutes the final report for this project.

Several discussions with Mr. Richard Chew, technical monitor for this contract at Navel Weapons Center, are gratefully acknowledged. The experimental results included in Chapter 3 were provided by Mr. Chew based on the fabrication and measurements carried out at the Naval Weapons Center, China Lake.

CONTENTS

TABLES

TABLE

FIGURES

FIGURE

CHAPTER 1

INTRODUCTION

1.1 Motivation of Research Work

Series-fed arrays of printed microstrip patches (shown in *Fig.* 1.1) provide a convenient compact configuration for obtaining a fan-shaped radiation pattern with reasonably low side lobe levels. Low values of side lobe level are obtained by tailoring the amplitude distribution along the array, which in turn is acheived by adjusting the amount of the power radiated by each of the individual elements in the array. Rectangular microstrip patches have been widely used as elements of series-fed arrays [1-4]. For microstrip patches fed along the radiating edges (shown in *Fig* 1.1.*b*), the power radiated is controlled by adjusting the dimension of the radiating edge [1-3]. For rectangular microstrip patches fed along the non-radiating edges, the power radiated can be controlled by the locations of the input and output ports [4].

For series-fed arrays with a large number of elements, the first few elements are required to radiate very small fractions of the input power. Example of power distribution for a 19 element series-fed array with -30 dB side lobe level Taylor distribution is shown in Table 1.1. As shown in *Table* 1.1, the required fraction of power radiated for the first two elements is less than 1%. For these two elements, the width of the designed patches will be very small (less than 1 mm). With the commonly used microstrip fabrication techniques, accurate etching of patches of dimensions less than 1 mm in a large substrate

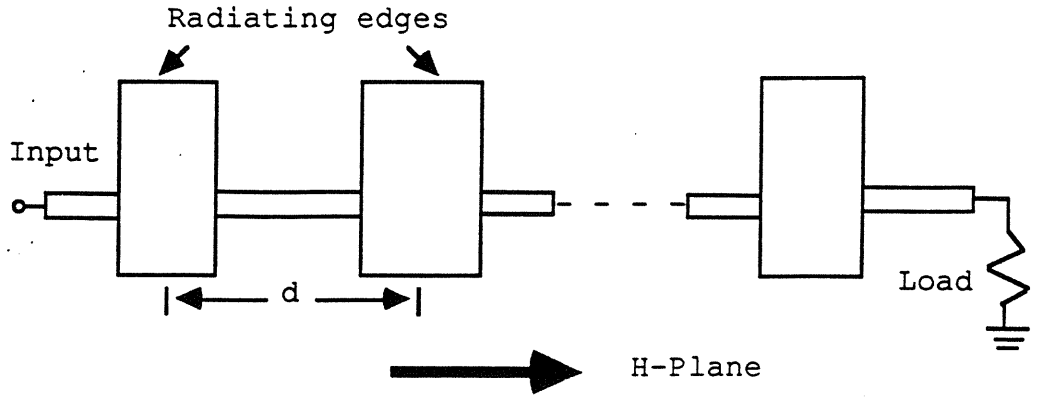

a) Series-fed array with polarization in the plane perpendicular to the array axis

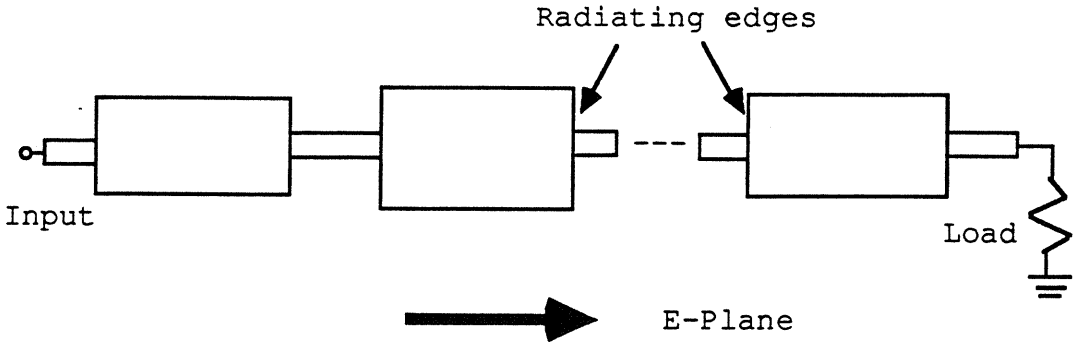

b) Series-fed array with polarization in the plane parallel to the array axis

Figure 1.1: Series-fed linear arrays of rectangular microstrip patches

Table 1.1. Typical power radiated and $|S_{21}|$ distributions in a 19-element series-fed linear array

Element#	Prad/Pin	$\|S_{21}\|$
1	0.00729	0.9963
2	0.00961	0.9952
3	0.01590	0.9920
4	0.02776	0.9860
5	0.04452	0.9775
6	0.06486	0.9670
7	0.08911	0.9544
8	0.11716	0.9396
9	0.14721	0.9235
10	0.17831	0.9065
11	0.21014	0.8887
12	0.23978	0.8719
13	0.26333	0.8583
14	0.27824	0.8496
15	0.41379	0.8503
16	0.24563	0.8685
17	0.18956	0.9002
18	0.14281	0.9258
19	0.12734	0.9342

- Taylor distribution with -30 SLL and NA=5.
- 5% of input power dissipated in the load.

becomes difficult and this limitation puts restriction on the achievable side lobe level. Furthermore, the conductor loss associated with narrow patches is very high and reduces the overall efficiency of the array. In order to avoid these problems it is desirable to introduce alternative configurations that allow the percentage of the radiated power to be reduced without reducing drastically the width of the patch.

1.2 Proposed Alternative Two-Port Configurations

Figures 1.2 and 1.3 show two proposed configurations which may yield low values of power radiated without reducing the width of the patch. Figure 1.2 shows a rectangular microstrip patch gap-coupled to a microstrip line. Example of series-fed linear array of capacitively-coupled rectangular microstrip patches with E-plane parallel to the array axis (non-radiating edge coupling) is reported in [5]. No analysis or design procedure for such arrays has been reported in the open literature. For the configuration shown in Fig 1.2, the patch is coupled to the line along the radiating edge because of polarization requirement. The excitation of the patch is accomplished by the fields fringing across the gap. The amount of power radiated is controlled by varying the gap width S (spacing between the patch and the line) and also the patch width b. A perfect input match is obtained by varying the characteristic impedances of the input and the output microstrip lines. Since these lines may have different widths, it is assumed that their edges (at the gap side) are colinear with the edge of the line coupled to the patch.

Figure 1.3 shows the configuration of a directly-fed one-port rectangular microstrip patch. In this configuration, the power radiated is controlled by varying the width of the patch b as well as the characteristic impedances of

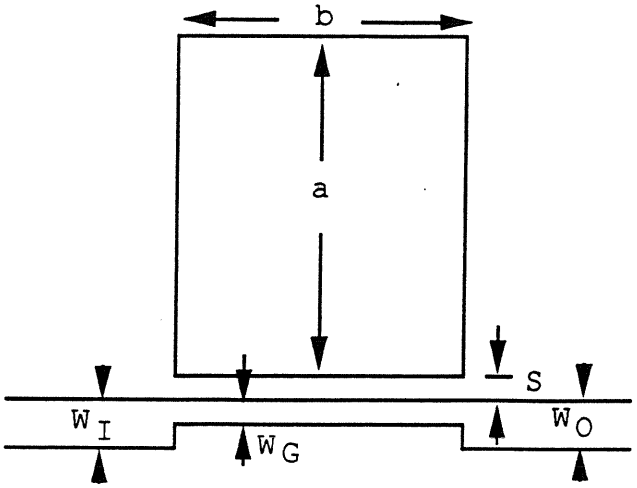

Figure 1.2. Two-port rectangular microstrip patch gap-coupled to a microstrip feed line

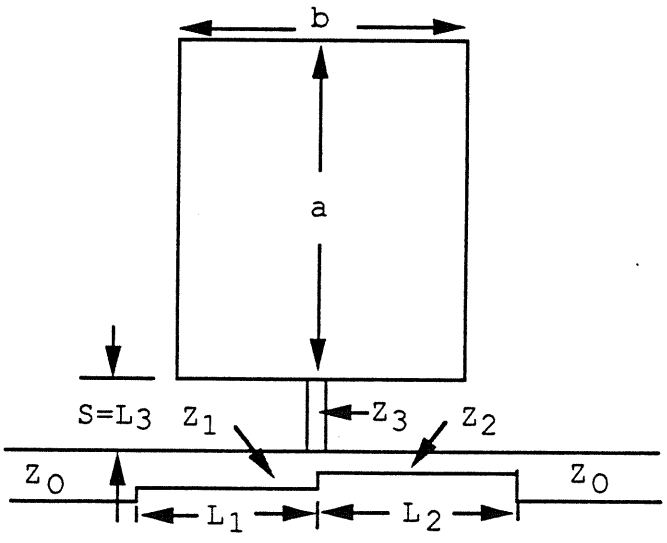

Figure 1.3. Two-port rectangular microstrip patch directly-coupled to a microstrip feed line

the microstrip lines in the power dividing network.

1.3 Organization of the Report

In Chapter Two, the directly-fed rectangular microstrip patch configuration is investigated. We consider the case of microstrip patches on a thin substrate (dielectric constant ϵ_r and thickness h) with and without a dielectric cover layer. The MNM approach for this structure is presented. Analysis of this configuration based on the transmission line model for the feed is used to obtain a first order design.

The configuration of the gap-coupled rectangular microstrip patch is investigated in details in Chapter Three. We consider also the case of microstrip patches on a thin substrate (dielectric constant ϵ_r and thickness h) with and without any dielectric cover layer. The MNM approach [6] is used to model the gap in terms of an equivalent network containing inductance and capacitance elements. The radiation from the patch and from the gap is modeled in terms of the self conductances in the mutual coupling (MCN) network. Computation of elements of the equivalent gap network by modeling the structure as section of asymmetric coupled line is also discussed. Analysis of the configuration using segmentation method to yield the two-port antenna characteristics is also discussed in Chapter Three. A step by step design procedure and optimization of the configuration for input match (for given patch dimensions) is also presented in this Chapter. Numerical results for a typical gap-coupled patch based on the MNM approach are also included in Chapter Three. Results given include scattering parameters, fractional power radiated and plots of both E-plane and H-plane far-field patterns. A comparison of MNM approach and moment method and measurement is also given in Chapter 3.

In Chapter Four, a computer-aided design pakcage based on the MNM approach has been developed for the design, analysis and sensitivity analysis of series-fed arrays of gap-coupled patches. A series-fed array is analyzed by using the concept of unit cells. Each unit cell consists of radiating patch gap-coupled to a microstrip line and sections of input and output microstrip lines. The dielectric and conductor losses are included in the design procedure. The CAD procedure is used for the design of a sample array without any cover layer and a sample array with a dielctric cover layer. Sensistivity of the sample arrays with respect to various design parameters is also included in chapter Four. Chapter Five contains some concluding remarks.

CHAPTER 2

DIRECTLY-FED RECTANGULAR MICROSTRIP PATCH

2.1 MNM Approach

An equivalent multiport network for the directly-fed rectangular microstrip patch configuration shown in *Fig.* 1.3 is shown in *Fig.* 2.1. This model is similar to the MNM model for a microstrip fed patch [4], except for that the junction of microstrip lines Z_1, Z_2 and Z_3 is also modeled by three planar segments as shown. The computation of the elements of the Z-matrices characterizing different subnetworks is carried out using the analysis technique reported in [6]. Modeling of the feed network in terms of equivalent planar segments allows for accounting for the effects of junction discontinuity reactances. Application of the segmentation method yields the two-port transmission characteristics as well as the radiation characteristics.

2.2 Transmission Line Approach

When the effect of the mutual coupling between the feed network and the patch is neglected, a first order design of the configuration is obtained by using the feed line model shown in *Fig.* 2.2. Z_{in}^{p} (shown in the figure) is the input impedance of the patch and is computed using the MNM approach for the patch. At the resonance frequency Z_{in}^{p} is purely real. The design approach is to find the lengths and the characteristic impedances of the three sections of transmission lines to achieve $S_{11} = 0$ and S_{21} equal to a pre-specified value.

Let Z_{in}^{2} denote the equivalent input impedance at reference plane 2′

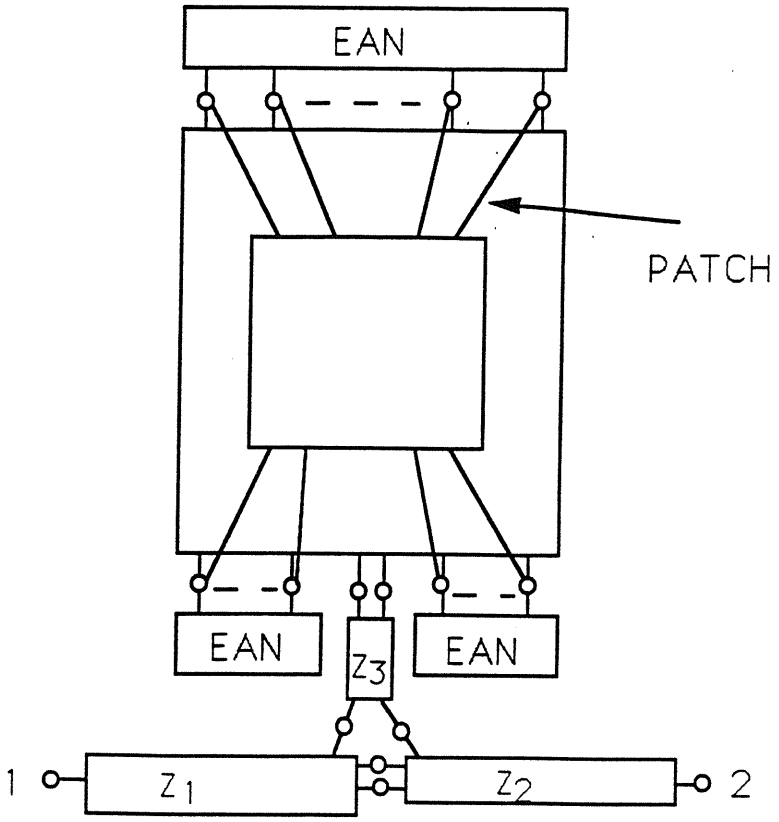

Figure 2.1. Equivalent multiport network model of the directly-fed rectangular microstrip patch

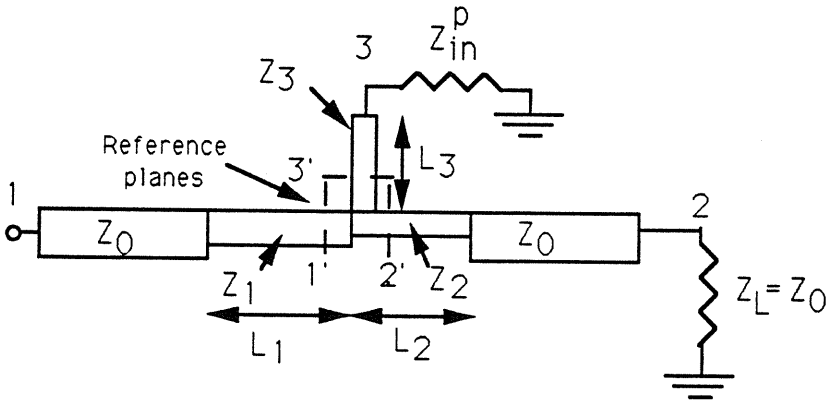

Figure 2.2. Equivalent transmission line model of the directly-fed rectangular microstrip patch

(looking into branch #2) when port 2 is terminated by a matched resistive load (Z_L=Z_0). Z_{in}^2 is a function of Z_0, L_2 and Z_2. Let Z_{in}^3 denote the input impedance at reference plane 3′ (looking into branch #3). Z_{in}^3 is a function of Z_{in}^p, L_3 and Z_3. Then, the input impedance Z_{in}^1 at reference plane 1′ is given by

$$Z_{in}^1 = \frac{Z_{in}^2 Z_{in}^3}{Z_{in}^2 + Z_{in}^3} \tag{2.1}$$

To get a match at the input port we require that Z_{in}^1 be real. If we choose $L_1 = \frac{\lambda}{4}$ then Z_1 has to be

$$Z_1 = \sqrt{Z_{in}^1 Z_0} \tag{2.2}$$

Let the ratio of power radiated to the input power of an element be denoted by α

$$\alpha = \frac{P_{rad}}{P_{in}} \tag{2.3}$$

Then using the equivalent network shown in *Fig.* 2.2 we have

$$\frac{Z_{in}^3}{Z_{in}^2} = \frac{1-\alpha}{\alpha} \tag{2.4}$$

2.3 Numerical Results

An insight into the performance of the directly-fed patch (shown in *Fig.* 1.3) can be obtained by using the approximate transmission line approach discussed in the previous section. To get an idea about the suitability of this configuration as an element of a series-fed linear array, we consider the case of a 19–element series–fed array (with Taylor distribution for -30 dB sidelobe level, given in Table 1.1). Table 2.1 shows the variation of the input impedance Z_{in}^p of the patch as a function of the patch width. Table 2.2 shows the computed width

Table 2.1. Variation of input impedance with patch width for an edge-fed rectangular patch

Width (mm)	Input Impedance (Ohms)
1.0	3081.02
2.0	1477.39
3.0	875.42
5.0	419.70
10.0	138.35
15.0	100.00

Table 2.2. Variation of characteristic impedance of a microstrip line with its width*

Line Width (mils)	Characteristic Impedance (Ohms)
345	10
155	20
45.5	50
12.6	100
3.7	150

ε_r=2.2, h=1/64 inch tanδ =0.0009

t =18 μ m σ =4E7 S/m

of microstrip line for given values of characteristic impedance. For obtaining the results of these two tables the following parameters have been used: ϵ_r = 2.2, h=1/64 inch, $tan\delta$ = 0.0009, t=0.5 oz and $\sigma = 4 \times 10^7$ S/m. Both of these Tables are needed in the present study. In the present study, we take $Z_0 = 100\Omega$ (12.6 mils) to be the maximum impedance for the interconnecting lines. As shown in Table 1.1, α for the first array element is

$$\alpha = 7.29 \times 10^{-3} \tag{2.5}$$

Inserting this value of α into equation 2.4, we have

$$Z_{in}^3 = 137 Z_{in}^2 \tag{2.6}$$

To be able to satisfy the above equation, it is required that Z_{in}^3 be as large as possible and Z_{in}^2 be as small as possible. To acheive these requirements the following options are available.

Option #1:

To obtain a large value of Z_{in}^3, we select the following parameters for microstrip line section #3

$$L_3 = \frac{\lambda}{2} \tag{2.7}$$

$$Z_3 \quad arbitrary \tag{2.8}$$

The transmission line analysis of branch line #3 yields

$$Z_{in}^3 = Z_{in}^p \tag{2.9}$$

Hence, the values of Z_{in}^3 can be selected from Table 2.1. To obtain a small value for Z_{in}^2, the length of line section #2 is selected to be

$$L_2 = \frac{\lambda}{4} \tag{2.10}$$

Using transmission line analysis for branch line #2 and making use of equation 2.4 we have

$$Z_2 = \sqrt{Z_0 Z_{in}^2} \tag{2.11}$$

$$= \sqrt{Z_0 Z_{in}^3 \frac{\alpha}{1-\alpha}} \tag{2.12}$$

For example, letting $Z_{in}^p = 3000\Omega$ (Patch Width = 1 mm) and using $Z_0 = 100\Omega$ (12.6 mil wide line) will yield

$$Z_2 = \sim 47.0\Omega \text{ (Line Width = 1.28 mm)} \tag{2.13}$$

This is an acceptabe value of Z_2. However, the space needed for length $L_3 = \frac{\lambda}{2}$ will double the dimension of the array in the transverse direction (perpendicular to the array axis).

Option #2

To obtain a large value of Z_{in}^3, we select the following values for microstrip line section #3

$$L_3 = \frac{\lambda}{4} \tag{2.14}$$

$$Z_3 = 100\Omega \tag{2.15}$$

Hence, we have

$$Z_{in}^3 = \frac{(Z_3)^2}{Z_{in}^p} \tag{2.16}$$

For Z_{in}^3 to be as large as possible, we need Z_{in}^p to be as small as possible. The smallest value of Z_{in}^p (from Table 2.1) is 138Ω (Patch Width = 10 mm). This maximum value of patch width is limited by the inter-element spacing which is taken to be

$$\frac{\lambda_o}{2} = 11.5\text{mm} \tag{2.17}$$

Even at these extreme values, the maximum value of Z_{in}^3 which can be used is 163Ω. This value yields

$$Z_2 = 10.95\Omega \text{ (Line Width} = 7.93 \text{ mm)} \tag{2.18}$$

Such a line width is of the same order as the patch width and hence is not practical to work with.

Option #3

In this case we select the following values for the parameters of the microstrip line section #3

$$Z_3 = Z_{in}^p \tag{2.19}$$

$$L_3 \qquad arbitrary \tag{2.20}$$

The maximum achievable value of Z_{in}^3 in this case will be

$$Z_{in}^3 = Z_3 = Z_{in} = 100\Omega \tag{2.21}$$

This value is lower than the 163Ω obtained in option #2 which leads to an even smaller value for Z_2. Hence, this option is not also useful.

2.4 Discussion

To acheive a small value for fractional of power radiated, the approximate transmission line analysis carried out in Section 2.3 presents three different options. Numerical example for the case of a 19-element array shows that only one option may be acceptabe. Even this option requires an increase in the array dimension in the E-plane. This configuration may be suitable for smaller arrays, but is not very useful for large arrays when the required fractional power radiated from the first few elements is very small.

CHAPTER 3

GAP-COUPLED RECTANGULAR MICROSTRIP PATCH

3.1 MNM Approach

An equivalent multiport network model for the configuration of the gap-coupled rectangular microstrip patch shown in *Fig.* 1.2 is shown in *Fig.* 3.1. As in the MNM approach for other configurations of radiating microstrip patches [6], the fields underneath the patch, the external fields and the fields underneath the microstrip feed lines are modeled separately in terms of multiport subnetworks. As shown in *Fig.* 3.1, the antenna structure is divided into eight subnetworks. The fields on the two sides of an interface between any two subnetworks are matched at discrete number of points by subdividing the common continuous interface into a number of sections (or ports). Various multiport subnetworks are characterized in terms of either Z- or Y-matrices. Descriptions of the internal field networks (PATCH, TLI, TLG and TLO) as well as the edge admittance networks (EANP and EANL) are summarized in the following subsections. Modeling of the gap in terms of an equivalent network and a detailed derivation of the elements of the Y-matrix characterizing the gap is given in Section 3.2. The elements of the Y-matrix are derived by modeling the structure as a pair of asymmetric coupled line section. The radiation from the patch and the coupling section of line as well as the mutual coupling among them are modeled in terms of an MCN network. Description of this network and derivation of the Y-matrix characterizing this network are

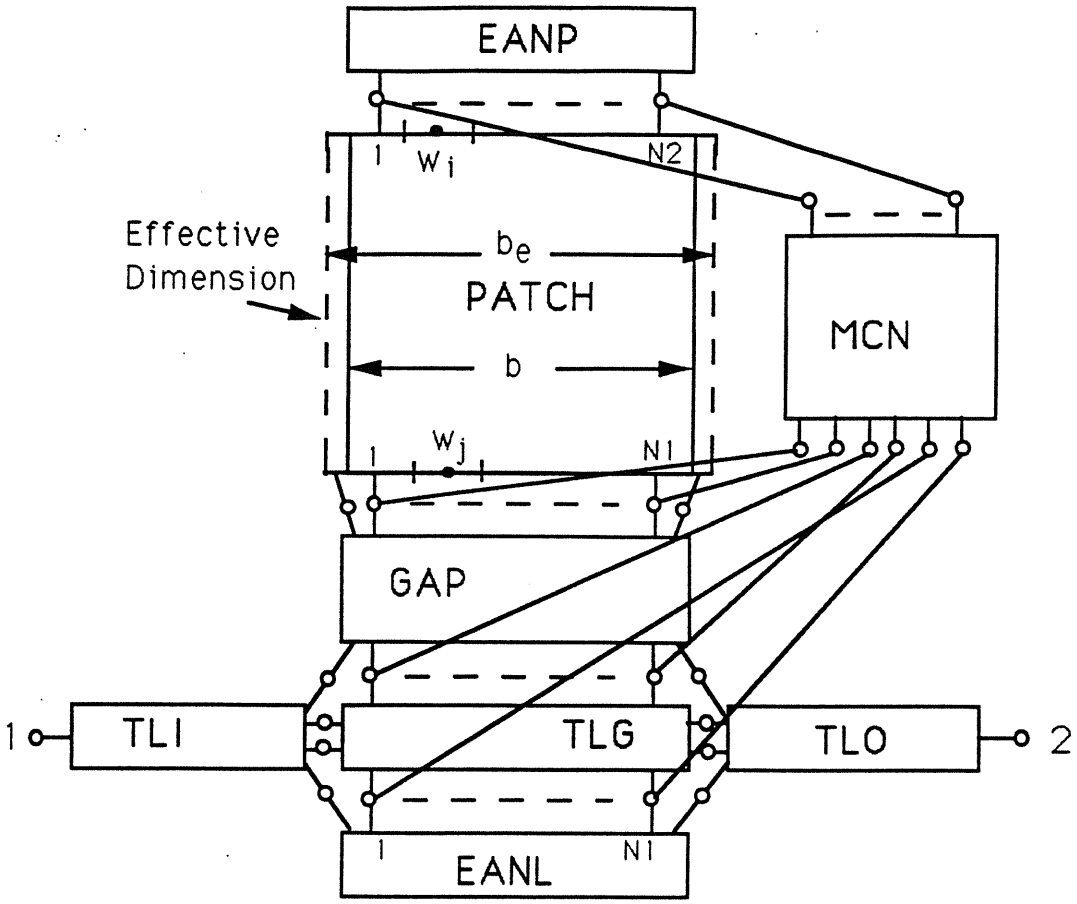

Figure 3.1. Equivalent multiport network model for the gap-coupled rectangular microstrip patch shown in *Fig.* 1.3

given in *Section* 3.3.

Segmentation analysis of the configuration, by combining various sub-networks modeling the structure, is discussed in *Section* 3.4. The segmentation analysis of the structure yields its two-port transmission characteristics as well as its radiation performance. A step-by-step design of a two-port patch for input match and a prescribed value of S_{21} is given in *Section* 3.5. The CAD methodology, based on the MNM approach, is used for the design and analysis of sample gap-coupled patches with and without a dielectric cover layer. Comparisons of MNM approach, moment method and experimental results are given for sample gap-coupled patches.

3.1.1 Internal Field Networks In most applications of microstrip antennas, the thickness h of the substrate is small compared to the operating wavelength ($k_0 h << 1$). For this cases the solution for the electromagnetic fields in the region between the patch and the ground plane (denoted by PATCH in Fig 3.1) is obtained by considering this region as a two-dimensional structure. The z-varying fields along the non-radiating edges (of dimension a) are included in modeling of PATCH, by defining an equivalent width and an effective dielectric constant for the two-dimensional PATCH component. The method for computing effective width and effective dielectric constant for a microstrip line without a cover layer is given in [9]. Expressions for computing effective width and effective dielectric constant with a cover layer are given in [13]. The z-varying fields at the inner radiating edge (dimension b) at the gap side is included in the modeling of the GAP and the MCN networks. On the other hand, the z-varying fields at the outer radiating edges of the patch and the feed line are included in the modeling of the EANP and MCN networks.

The elements of the Z-matrix characterizing the PATCH network are derived from the Green's function as follows [6]:

$$Z_{ij} = \frac{1}{W_i W_j} \int_{W_i} \int_{W_j} G(x_i, y_i | x_j, y_j) ds_i ds_j \tag{3.1}$$

where (x_i, y_i) and (x_j, y_j) denote the locations of the ports of widths W_i and W_j respectively (as shown in *Fig.* 3.1). The two line integrals are along the widths of the ports i and j. As shown in *Fig.* 3.1, The PATCH network has N2 ports connected simultaneously to the EANP and MCN networks, N1 ports connected simultaneously to the GAP and MCN networks and 2 ports on either side of the N1 ports connected to the GAP network only. The N1 and N2 ports (connected to the MCN network) are confined only to the physical width b.

The electromagnetic fields in the region underneatch the microstrip lines are also obtained by modeling these lines as two-dimensional components. The TLG network shown in *Fig.* 3.1 is considered as a two dimensional component of width W_G (physical width of line) and length b (width of the patch) and filled with the dielectric constant ϵ_r. The z-varying fields along the length of the line are included in the EANL, GAP and MCN networks as discussed later. The elements of the Z-matrix characterizing this network are also obtained by using equation 3.1. The TLG network has N1 ports connected simultaneously to the GAP and MCN networks, N1 ports connected simultaneously to the EANL and MCN networks, ND ports connected to the TLI network and ND ports connected to the TLO network.

The z-varying fields along the length of the input and output line sections (denoted by TLI and TLO in *Fig.* 3.1) are included by using effective widths and effective dielectric constants for the two-dimensional components modeling these lines. The length of the input and the output lines should

be long enough ($> \lambda/8$, where λ is the wavelength in the microstrip line), so that only the dominant mode is present at the external ports of the lines (not connected to the GAP network). Hence, only one port is taken at those ends of the lines. At the other ends of both TLI and TLO networks, there are ND ports connected to the TLG network, 1 port connected to the GAP network and another port connected to the EANL network. The two ports connected to the EANL and the GAP networks are required for continuity of edge current flowing tangential to the feed lines. The input and the output feed lines shown in *Fig.* 1.3 consist of one section only. If these lines contain more than one section (of different widths), additional sections are also modeled as two-dimensional components.

The effect of dielectric losses, associated with the internal fields, is incorporated by considering ϵ_r and ϵ_{re} to be a complex quantities. The imaginary part of these quantities, denoted by $tan\delta_d$, accounts for the dielectric losses. Conductor losses are also included in an approximate manner by adding to $tan\delta_d$ an equivalent loss tangent $tan\delta_c$ given by

$$tan\delta_c = \frac{P_c}{P_d} tan\delta_d \tag{3.2}$$

where P_c is the power dissipation because of the conductor loss and P_d is the power dissipation in the dielectric substrate. In the case of magnetic wall boundary, $tan\delta_c$ is independent of the component geometry [7] and is equal to $\sqrt{2/(\omega\mu\sigma)}/h$, where σ is the conductivity of the patch metalization.

3.1.2 Edge Field Networks The edge field networks account for the stored energy in the fringing electric and magnetic fields. The EANP network, shown in *Fig.* 3.1, accounts for the energy stored in the fringing electric fields at the outer radiating edge of the patch. The elements of the

Y-matrix characterizing this network are all zero except the diagonal terms which are equal to the total edge susceptance divided by the number of ports (N2). The radiation from this edge is included in the MCN network described in *Section* 3.3. Evaluation of edge capacitance based on [17] has been used in this work (for the cases with and without cover layer).

The EANL network connected to the outer edge of the section of line coupled to the patch accounts for both the fringing electric and magnetic fields at that edge. Addition of inductances to account for fringing magnetic fields becomes necessary because, unlike for EANP, voltage is not constant along the outer edge of TLG. As shown in *Fig.* 3.2, the EANL network consists of the parallel combinations of capacitances and inductances.

If the effective width of the coupling line W_G^e is larger than the width of the input line W_I, then one port is used to connect the EANL network to the TLI network. Also, if W_G^e is larger than the width of the output line W_O then one port is used to connect the EANL network to the TLO network. These connections assure the continuity of the tangential component of the current flowing along the outer edge of the microstrip feed line.

Edge Capacitance. The edge capacitance networks accounts for the energy stored in the fringing electric fields at the outer edges (inside and outside) of the microstrip line. The edge capacitance is divided uniformly along the N1 ports. The edge capacitance per unit length C_e (shown in *Fig.* 3.2) is equal to the fringing capacitance per unit length C_f of an isolated microstrip line given by

$$C_f = (C_T - C_m)/2 \tag{3.3}$$

where C_m is the parallel plate capacitance associated with the physical width

per unit length of the line

$$C_m = \epsilon_0 \epsilon_r W_G / h, \tag{3.4}$$

and the total capacitance per unit length of the line C_T is given by

$$C_T = \epsilon_0 \epsilon_{re} W_G^e / h, \tag{3.5}$$

where $W_G^e = \eta_0 h / (Z_0 \sqrt{\epsilon_{re}})$ (where η_0 is the free space impedance). Values of effective dielectric constant ϵ_{re} and characteristic impedance Z_0 are given in [9] for a microstrip line without a cover layer and the method in [13] is used for a microstrip line with a cover layer.

Edge Inductance. The edge inductance accounts for the energy stored in the fringing magnetic fields along the outer edge of the line. As in the case of edge capacitance, the edge inductance is also distributed uniformly over the N1 ports and is computed from the fringing inductance per unit length of an isolated microstrip line. The edge inductance per unit length L_e (shown in *Fig.* 3.2) is equal to the fringing inductance L_f per unit length given by

$$L_f = \frac{2 L_m L_T}{L_m - L_T} \tag{3.6}$$

where L_T is the total inductance per unit length of the line

$$L_T = \mu_0 h / W_G^e \tag{3.7}$$

and L_m is the inductance per unit length of the line is given by:

$$L_m = \mu_0 h / W_G \tag{3.8}$$

The elements of the Y-matrix [Y] characterizing the EANL network are computed from the equivalent circuit shown in *Fig.* 3.2. The [Y] matrix is

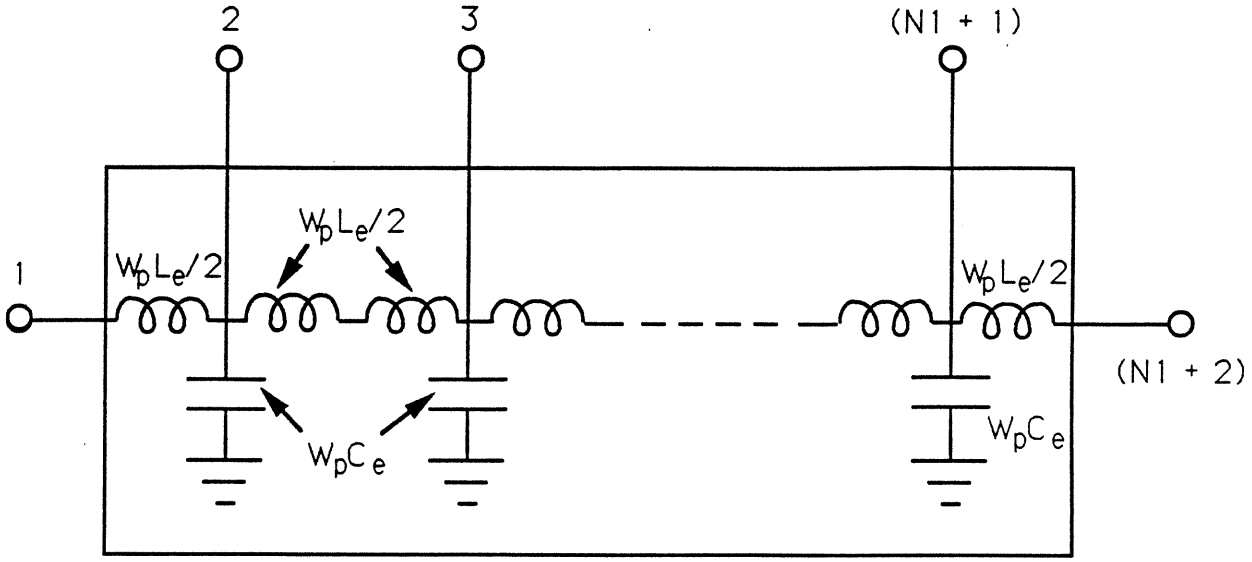

Figure 3.2. Elements of the edge admittance network EANL at the outer edge of the feed line

symmetrical, with:

$$Y(1,1) = Y(N1+2, N1+2) = 2/X_e \tag{3.9}$$

$$Y(1,2) = Y(N1+2, N1+1) = -2/X_e \tag{3.10}$$

$$Y(2,2) = Y(N1+1, N1+1) = B_e + 3/X_e \tag{3.11}$$

$$Y(2,3) = Y(N1+1, N1) = -1/X_e \tag{3.12}$$

$$Y(i,i) = B_e + 2/X_e, \qquad i = 3, N1 \tag{3.13}$$

$$Y(i,i+1) = -1/X_e, \qquad i = 3, N1 \tag{3.14}$$

where $X_e = j\omega W_p L_e$ and $B_e = j\omega W_p C_e$ (where $W_p = b/N1$ is the width of the ports and b is the width of the patch). All other terms in the Y-matrix are zeros.

3.2 Modeling of the GAP network

A model for the gap region in the gap-coupled rectangular microstrip patch antenna configuration shown in *Fig.* 1.2 is developed in this section. When a TEM wave is propagating along the microstrip feed line, fringing fields (both electric and magnetic) are set up along the edges of the line. If the width of the gap (denoted by S in *Fig.* 1.2) is small (less than few times the substrate thickness h) the fringing fields will extend to the patch thereby exciting the patch. The configuration of the patch and the feed line can be considered as a section of an asymmetric coupled line. An asymmetric coupled line can be described in terms of a (2×2) capacitance matrix [C] and a (2×2) inductance matrix [L]. The microstrip line is considered as conductor #1 and the patch is considered as conductor #2. A two-dimensional planar-lumped model of an asymmetric coupled line is shown in *Fig.* 3.3. Based on this model, an equivalent multiport network of the gap is shown in *Fig.* 3.4. Also

shown in *Fig* 3.4, is the numbering of ports, where the ports along the feed line side are numbered first. As shown in *Fig.* 3.4, the GAP network consists of the parallel combination of a capacitive network and an inductance network. The two-dimensional planar segment SEGP accounts for the capacitance and inductance associated with fields underneath the patch and the fringing fields at the outer edge of the patch. The two-dimensional planar component SEGL accounts for the capacitance and the inductance associated with the fields underneath the feed line and the fringing fields at the outer edge of the feed line.

The various parameters modeling the gap (as shown in *Fig* 3.4) are evaluated such that the capacitance and inductance matrices of the configuration (shown in *Fig.* 3.3) are identical to [C] and [L] matrices of the asymmetric coupled line.

3.2.1 Modeling of the Capacitive Part The capacitive part of the GAP network accounts for the fringing electric fields at the inner edge of the patch (modeled by the mutual capacitance C_f^p) and at the inner edge of the feed line (in terms of C_f^ℓ) and the interaction between them (modeled by the mutual capacitance C_g). The capacitive part of the two-dimensional model shown in *Fig.* 3.3 is shown in *Fig.* 3.5. Capacitances C_p^p and C_p^ℓ (shown in *Fig.* 3.5) are computed from the patch and the line dimensions respectively as follows:

$$C_p^\ell = \frac{\epsilon_o[\epsilon_{re}(W_G)W_G^e + \epsilon_r W_G]}{2h} \tag{3.15}$$

$$C_p^p = \frac{\epsilon_o[\epsilon_{re}(a)a^e + \epsilon_r a]}{2h} \tag{3.16}$$

where $\epsilon_{re}(W_G)$ and $\epsilon_{re}(a)$ are the effective dielectric constant of microstrip lines of width W_G and a respectively. Capacitances C_f^ℓ, C_f^p and C_g are obtained by

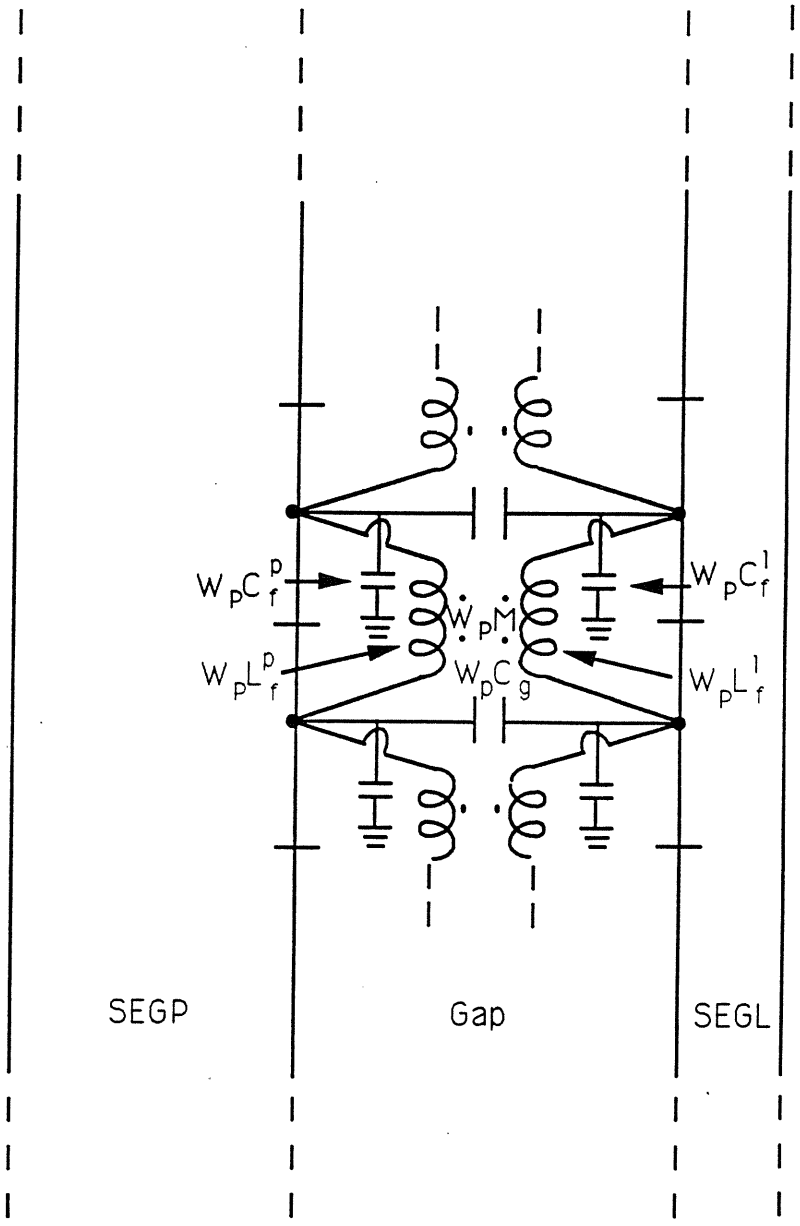

Figure 3.3. Two-dimensional planar-lumped model of an asymmetric coupled line

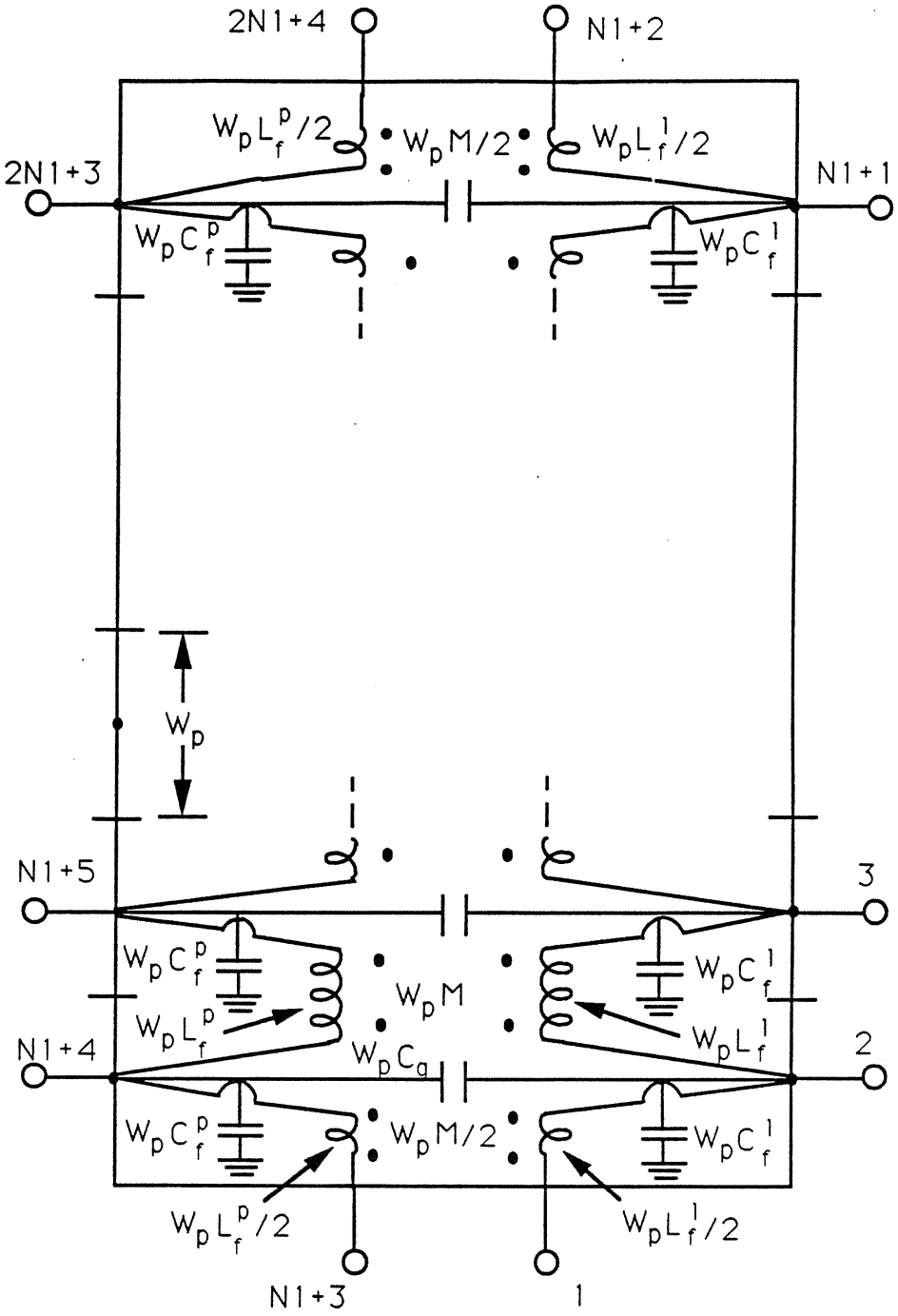

Figure 3.4: Multiport network model of the gap region

equating the elements of the [C]-matrix computed from *Fig.* 3.5 with those of the [C]-matrix of the asymmetrical coupled line as follows:

$$C_{11} = C_p^\ell + C_f^\ell + C_g \tag{3.17}$$

$$C_{22} = C_p^p + C_f^p + C_g \tag{3.18}$$

$$C_{12} = C_{21} = -C_g \tag{3.19}$$

Therefore, we have

$$C_f^\ell = C_{11} + C_{12} - C_p^\ell \tag{3.20}$$

$$C_f^p = C_{22} + C_{12} - C_p^p \tag{3.21}$$

$$C_g = -C_{12} \tag{3.22}$$

From the equivalent multiport network of the gap (shown in *Fig.* 3.4), the elements of the Y-matrix $[Y_g^c]$ of the capacitive part of the gap are given by

$$[Y_g^c] = j\omega W_p \left[\begin{array}{ccc|ccc} 0 & & & 0 & & \\ & C_g^\ell & & & -C_g & \\ & & \ddots & & & \ddots \\ & & C_g^\ell & & & -C_g \\ & & 0 & & & 0 \\ \hline 0 & & & 0 & & \\ & -C_g & & & C_g^p & \\ & & \ddots & & & \ddots \\ & & -C_g & & & C_g^p \\ & & 0 & & & 0 \end{array}\right] \tag{3.23}$$

where

$$W_p = Port\ Width, \tag{3.24}$$

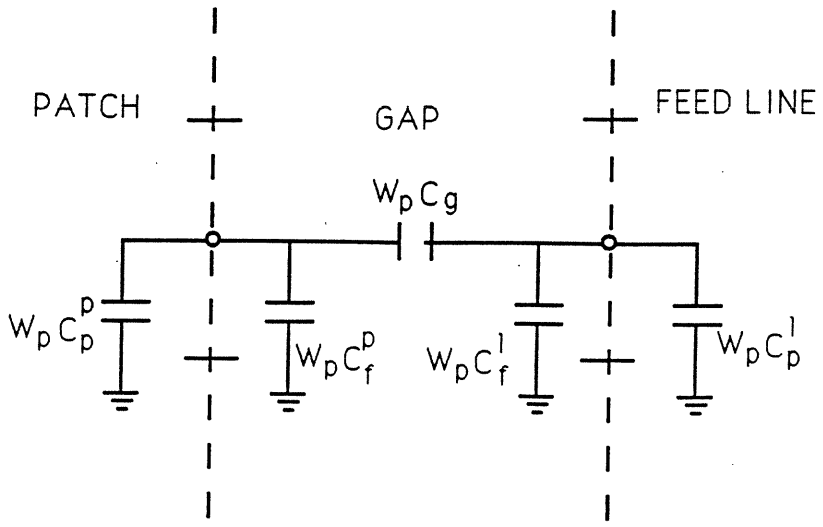

Figure 3.5: Capacitive part of the two-dimensional model shown in *Fig.* 3.3

$$C_g^\ell = C_f^\ell + C_g, \tag{3.25}$$

$$C_g^p = C_f^p + C_g. \tag{3.26}$$

Elements of the matrix $[Y_g^c]$ which are not given explicitely in equation (3.23) are equal to zero.

3.2.2 Modeling of the Inductive Part. The inductive part of the gap model (shown in *Fig.* 3.4) accounts for the fringing magnetic fields at the inner edge of the patch (in terms of L_f^p) and at the inner edge of the feed line (in terms of L_f^ℓ) and the interaction between them (in terms of the mutual inductance M). The inductive part of the two-dimensional model of the asymmetrical coupled line (composed of patch and feedline) is shown in *Fig.* 3.6. Inductances L_p^ℓ and L_p^p (shown in *Fig.* 3.6) associated with the fields underneath the planar waveguides of widths a^p and W_G^p are given by

$$L_p^\ell = L_m^\ell L_e^\ell / (L_m^\ell + L_e^\ell) \tag{3.27}$$

$$L_p^p = L_m^p L_e^p / (L_m^p + L_e^p) \tag{3.28}$$

where L_m^p and L_m^ℓ are the main inductances per unit length of the patch and line respectively

$$L_m^p = \frac{\mu_o h}{a} \tag{3.29}$$

$$L_m^\ell = \frac{\mu_o h}{W_G} \tag{3.30}$$

and L_e^p and L_e^ℓ are the edge inductances per unit length at the outer edge of the patch and the feed line respectively:

$$L_e^\ell = \frac{2\mu_o h}{W_G^e - W_G} \tag{3.31}$$

$$L_e^p = \frac{2\mu_o h}{a^e - a} \tag{3.32}$$

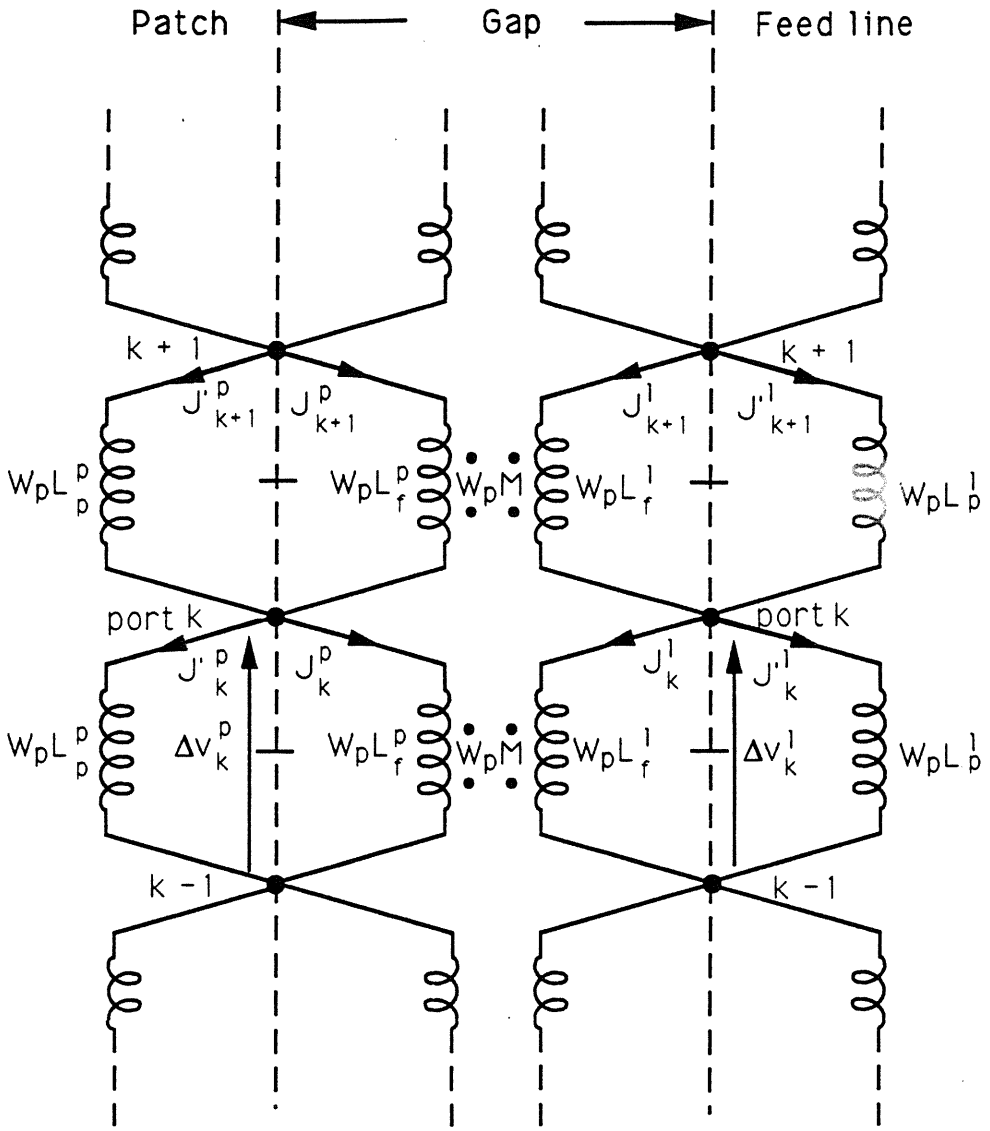

Figure 3.6: Inductive part of the two-dimensional model shown in *Fig.* 3.3

The inductances per unit length, L_f^ℓ, L_f^p and M are computed from the equivalent lumped circuit shown in *Fig.* 3.6. Let us denote

$$\Delta v_i^\ell = V_i^\ell - V_{i-1}^\ell \tag{3.33}$$

$$\Delta v_j^p = V_j^p - V_{j-1}^p \tag{3.34}$$

where superscript ℓ denotes the (N1+2) ports along the feed line side and superscript p denotes the (N1+2) ports along the patch side. values of subscripts i and j vary from 2 to (N1+2). The $i = k$ port in *Fig.* 3.6 corresponds to a k port in *Fig.* 3.4, however the $j = k$ port in *Fig.* 3.6 corresponds to the $(N1 + 2 + k)$ port in *Fig.* 3.4. From the equivalent circuit shown in *Fig.* 3.6 we have

$$\Delta v_k^\ell = j\omega W_p L_f^\ell J_k^\ell + j\omega W_p M J_k^p \tag{3.35}$$

$$\Delta v_k^p = j\omega W_p M J_k^\ell + j\omega W_p L_f^p J_k^p \tag{3.36}$$

where J_k^ℓ and J_k^p are the currents flowing from port k to port $(k-1)$ along inductances L_f^ℓ and L_f^p respectively and W_p is the width of ports. Also from *Fig.* 3.6, we have

$$\Delta v_k^\ell = j\omega W_p L_p^\ell J_k'^\ell \tag{3.37}$$

$$\Delta v_k^p = j\omega W_p L_p^p J_k'^p \tag{3.38}$$

where $J_k'^\ell$ and $J_k'^p$ are the currents flowing flowing from ports k to $(k-1)$ along the inductances L_p^ℓ and L_p^p respectively. In matrix form, the above relations can be expressed as

$$\begin{bmatrix} J_k^\ell \\ J_k^p \end{bmatrix} = \frac{1}{j\omega W_p} \begin{bmatrix} L_f^\ell & M \\ M & L_f^p \end{bmatrix}^{-1} \begin{bmatrix} \Delta v_k^\ell \\ \Delta v_k^p \end{bmatrix} \tag{3.39}$$

$$\begin{bmatrix} J_k'^{\ell} \\ J_k'^{p} \end{bmatrix} = \frac{1}{j\omega W_p} \begin{bmatrix} L_p^{\ell} & 0 \\ 0 & L_p^{p} \end{bmatrix}^{-1} \begin{bmatrix} \Delta v_k^{\ell} \\ \Delta v_k^{p} \end{bmatrix} \tag{3.40}$$

The current $(I_k^{\ell})^T$ and $(I_k^{p})^T$, flowing from port k to port $(k-1)$ along L_{11} and L_{22} as shown in *Fig.* 3.7, are related to Δv_k^{ℓ} and Δv_k^{p} by

$$\begin{bmatrix} (I_k^{\ell})^T \\ (I_k^{p})^T \end{bmatrix} = \begin{bmatrix} J_k^{\ell} \\ J_k^{p} \end{bmatrix} + \begin{bmatrix} J_k'^{\ell} \\ J_k'^{p} \end{bmatrix} = \frac{1}{j\omega W_p} \begin{bmatrix} L_{11} & L_{12} \\ L_{21} & L_{22} \end{bmatrix}^{-1} \begin{bmatrix} \Delta v_k^{\ell} \\ \Delta v_k^{p} \end{bmatrix} \tag{3.41}$$

Using the above relations we get

$$\begin{bmatrix} L_f^{\ell} & M \\ M & L_f^{p} \end{bmatrix}^{-1} = \begin{bmatrix} L_{11} & L_{12} \\ L_{21} & L_{22} \end{bmatrix}^{-1} - \begin{bmatrix} L_p^{\ell} & 0 \\ 0 & L_p^{p} \end{bmatrix}^{-1} \tag{3.42}$$

Hence,

$$L_f^{\ell} = (L_{11} - \Delta/L_p^{p})/DEN \tag{3.43}$$

$$L_f^{p} = (L_{22} - \Delta/L_p^{\ell})/DEN \tag{3.44}$$

$$M = L_{21}/DEN \tag{3.45}$$

where

$$DEN = 1 - L_{11}/L_p^{\ell} - L_{22}/L_p^{p} + \Delta/L_p^{p}L_p^{\ell} \tag{3.46}$$

$$\Delta = L_{11}L_{22} - L_{21}L_{12} \tag{3.47}$$

Admittance matrix (inductance part for the gap) $[Y_g^{\ell}]$: From *Figs.* 3.4 and 3.6, we have

$$V_2^{\ell} - V_1^{\ell} = j\omega W_p \frac{L_f^{\ell}}{2} J_2^{\ell} + j\omega W_p \frac{M}{2} J_2^{p} \tag{3.48}$$

$$V_k^{\ell} - V_{k-1}^{\ell} = j\omega W_p L_f^{\ell} J_k^{\ell} + j\omega W_p M J_k^{p}, \quad 2 < k < (N1+1) \tag{3.49}$$

$$V_{N1+2}^{\ell} - V_{N1+1}^{\ell} = j\omega W_p \frac{L_f^{\ell}}{2} J_{N1+2}^{\ell} + j\omega W_p \frac{M}{2} J_{N1+2}^{p} \tag{3.50}$$

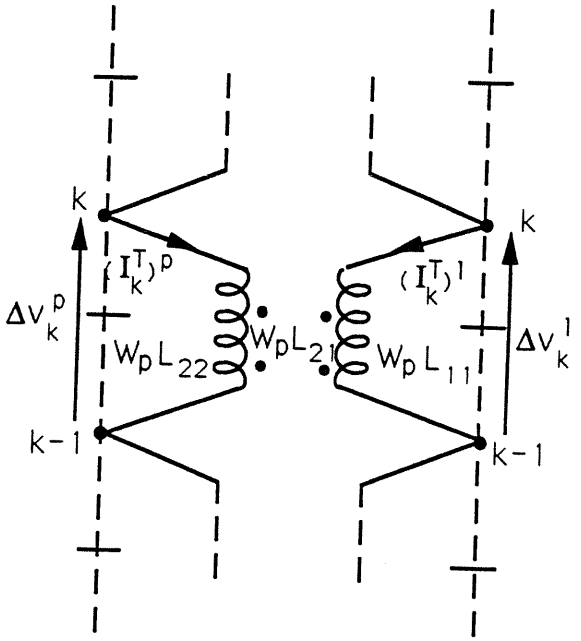

Figure 3.7. Equivalent lumped network for L-parameters of an asymmetric coupled line

Similar expressions are derived for the ports along the patch side by interchanging superscripts ℓ and p and replacing L_f^ℓ by L_f^p. In matrix form we can write

$$\begin{bmatrix} J_2^\ell \\ J_2^p \end{bmatrix} = \frac{1}{j\omega W_p} \begin{bmatrix} \frac{L_f^\ell}{2} & \frac{M}{2} \\ \frac{M}{2} & \frac{L_f^p}{2} \end{bmatrix}^{-1} \begin{bmatrix} V_2^\ell - V_1^\ell \\ V_2^p - V_1^p \end{bmatrix} \tag{3.51}$$

$$= \frac{2}{\Delta'} \begin{bmatrix} L_f^p & -M \\ -M & L_f^\ell \end{bmatrix} \begin{bmatrix} V_2^\ell - V_1^\ell \\ V_2^p - V_1^p \end{bmatrix} \tag{3.52}$$

$$\begin{bmatrix} J_k^\ell \\ J_k^p \end{bmatrix} = \frac{1}{\Delta'} \begin{bmatrix} L_f^p & -M \\ -M & L_f^\ell \end{bmatrix} \begin{bmatrix} V_k^\ell - V_{k-1}^\ell \\ V_k^p - V_{k-1}^p \end{bmatrix} \tag{3.53}$$

$$\begin{bmatrix} J_{N1+2}^\ell \\ J_{N1+2}^p \end{bmatrix} = \frac{2}{\Delta'} \begin{bmatrix} L_f^p & -M \\ -M & L_f^\ell \end{bmatrix} \begin{bmatrix} V_{N1+2}^\ell - V_{N1+1}^\ell \\ V_{N1+2}^p - V_{N1+1}^p \end{bmatrix} \tag{3.54}$$

where subscript k is such that $2 < k < (N1 + 1)$ and

$$\Delta' = j\omega W_p (L_f^\ell L_f^p - M^2) \tag{3.55}$$

The port currents I^ℓ are related to the J^ℓ currents as follows

$$I_1^\ell = - J_1^\ell \tag{3.56}$$

$$I_k^\ell = J_k^\ell - J_{k+1}^\ell, \qquad 2 < k < (N1 + 1) \tag{3.57}$$

$$I_{N1+2}^\ell = J_{N1+2}^\ell \tag{3.58}$$

Using the above relations, the port currents at the transmission line side are obtained as

$$I_1^\ell = \frac{2}{\Delta'}[L_f^p(V_1^\ell - V_2^\ell) - M(V_1^p - V_2^p)] \tag{3.59}$$

$$I_2^\ell = \frac{1}{\Delta'}[L_f^p(3V_2^\ell - 2V_1^\ell - V_3^\ell) - M(3V_2^p - 2V_1^p - V_3^p)] \tag{3.60}$$

$$I_k^\ell = \frac{1}{\Delta'}[L_f^p(2V_k^\ell - V_{k-1}^\ell - V_{k+1}^\ell) - M(2V_k^p - V_{k-1}^p - V_{k+1}^p)] \tag{3.61}$$

$$I^{\ell}_{N1+1} = \frac{1}{\Delta'}[L^p_f(3V^{\ell}_{N1+1} - 2V^{\ell}_{N1+2} - V^{\ell}_{N1}) - M(3V^p_{N1+1} - 2V^p_{N1+2} - V^p_{N1})] \quad (3.62)$$

$$I^{\ell}_{N1+2} = \frac{2}{\Delta'}[L^p_f(V^{\ell}_{N1+2} - V^{\ell}_{N1+1}) - M(V^p_{N1+2} - V^p_{N1+1})] \quad (3.63)$$

Similarly the port currents at the patch side are obtained as

$$I^p_1 = \frac{2}{\Delta'}[L^{\ell}_f(V^p_1 - V^p_2) - M(V^{\ell}_1 - V^{\ell}_2)] \quad (3.64)$$

$$I^p_2 = \frac{1}{\Delta'}[L^{\ell}_f(3V^p_2 - 2V^p_1 - V^p_3) - M(3V^{\ell}_2 - 2V^{\ell}_1 - V^{\ell}_3)] \quad (3.65)$$

$$I^p_k = \frac{1}{\Delta'}[L^{\ell}_f(2V^p_k - V^p_{k-1} - V^p_{k+1}) - M(2V^{\ell}_k - V^{\ell}_{k-1} - V^{\ell}_{k+1})] \quad (3.66)$$

$$I^p_{N1+1} = \frac{1}{\Delta'}[L^{\ell}_f(3V^p_{N1+1} - 2V^p_{N1+2} - V^p_{N1}) - M(3V^{\ell}_{N1+1} - 2V^{\ell}_{N1+2} - V^{\ell}_{N1})] \quad (3.67)$$

$$I^p_{N1+2} = \frac{2}{\Delta'}[L^{\ell}_f(V^p_{N1+2} - V^p_{N1+1}) - M(V^{\ell}_{N1+2} - V^{\ell}_{N1+1})] \quad (3.68)$$

In matrix form, the port currents and port voltages are related by

$$[Y^{\ell}_g] = \frac{1}{\Delta'}\begin{bmatrix} A & B \\ C & D \end{bmatrix} \quad (3.69)$$

where

$$A = \begin{bmatrix} 2L^p_f & -2L^p_f & & & & & \\ -2L^p_f & 3L^p_f & -L^p_f & & & & \\ & -L^p_f & 2L^p_f & -L^p_f & & & \\ & & \ddots & \ddots & \ddots & & \\ & & & -L^p_f & 2L^p_f & -L^p_f & \\ & & & & -L^p_f & 3L^p_f & -2L^p_f \\ & & & & & -2L^p_f & 2L^p_f \end{bmatrix} \quad (3.70)$$

$$D = \begin{bmatrix} 2L_f^\ell & -2L_f^\ell & & & & & \\ -2L_f^\ell & 3L_f^\ell & -L_f^\ell & & & & \\ & -L_f^\ell & 2L_f^\ell & -L_f^\ell & & & \\ & & \ddots & \ddots & \ddots & & \\ & & & -L_f^\ell & 2L_f^\ell & -L_f^\ell & \\ & & & & -L_f^\ell & 3L_f^\ell & -2L_f^\ell \\ & & & & & -2L_f^\ell & 2L_f^\ell \end{bmatrix} \tag{3.71}$$

$$B = C = \begin{bmatrix} -2M & 2M & & & & & \\ 2M & -3M & M & & & & \\ & M & -2M & M & & & \\ & & \ddots & \ddots & \ddots & & \\ & & & M & -2M & M & \\ & & & & M & -3M & 2M \\ & & & & & 2M & -2M \end{bmatrix} \tag{3.72}$$

Note that A, B, C *and* D are all tri-diagonal sub-matrices.

The admittance matrix $[Y_g]$, characterizing the GAP network, is the sum of $[Y_g^c]$ and $[Y_g^\ell]$ matrices obtained above:

$$[Y_g] = [Y_g^c] + [Y_g^\ell] \tag{3.73}$$

3.3 Modeling of MCN Network

The mutual coupling network (denoted by MCN in *Fig.* 3.1) accounts for the power radiated (in free space and through surface waves) from the edges of the patch and the coupling section of feed line as well as the mutual coupling among these edges. The MCN network is characterized by an admittance

matrix which is constructed as follow

$$[Y]_{MCN} = \begin{bmatrix} REAL(Y_{11}) & REAL(Y_{12}) & REAL(Y_{13}) & Y_{14} \\ REAL(Y_{21}) & REAL(Y_{22}) & REAL(Y_{23}) & Y_{24} \\ REAL(Y_{31}) & REAL(Y_{32}) & REAL(Y_{33}) & Y_{34} \\ Y_{41} & Y_{42} & Y_{43} & REAL(Y_{44}) \end{bmatrix} \quad (3.74)$$

In the above expression, subscript 1 denotes the outer edge of the feed line (which is divided into N1 ports), subscript 2 denotes the inner edge of the feedline (divided into N1 ports), subscript 3 denotes the inner edge of the patch (divided into N1 ports) and subscript 4 denotes the outer edge of the patch (divided into N2 ports). The submatrices $REAL(Y_{11})$, $REAL(Y_{22})$, $REAL(Y_{33})$ and $REAL(Y_{44})$ account for the radiation from the edges of the feed line and the patch respectively. The energy stored in the near fields at those edges has been included in the edge networks and the gap network as discussed in the previous sections. Other submatrices account for the mutual coupling among the various edges. In the evaluation of mutual couplings among edges 1, 2 and 3 only the real part of the mutual admittance is considered since the imaginary (reactive) part of this coupling gets included in the GAP network.

Evaluation of Elements of $[Y]_{MCN}$: For microstrip antennas on electrically thin substrates (as is the case in this work) and without any cover layer, the radiation from an edge and mutual coupling between two edges may be evaluated by representing the edge fields by line sources of equivalent magnetic currents and their images with respect to the ground plane [10]. This approximation ignores the effects of surface waves along the dielectric substrate. Experimental results of Jedlicka [11] have shown that surface waves have negligible effects on mutual coupling when the substrate is electrically

thin. The magnetic current line source at each edge is divided into a number of small sections (equal to the number of ports considered in the modeling of internal networks). The self radiation conductance G_e of each section is

$$G_e = W_p^2/(90\lambda_0^2) \tag{3.75}$$

For the evaluation of the mutual coupling between any two sections, each section is subdivided into smaller subsections, so that each subsection can be modeled as a magnetic current element. Typically we consider 4 subsections per section. Amplitudes M of the magnetic currents elements are equal to the voltages at the corresponding ports of the edge. Hence, the computation of the various elements of the MCN network requires the evaluation of the mutual admittances among various subsections (e.g subsections i and j shown in *Fig.* 3.8) belonging to two distinct sections p and q. The mutual admittance Y_{ij} between subsections i and j is evaluated considering the two correspondingly located magnetic current elements as shown in the figure. The magnetic current element i, located at (x_i, y_i) in the z=0 plane, produces magnetic field at the location of the current element j (located at (x_j, y_j) at the z=0 plane) given by

$$H_\theta = -j\frac{k_0(2V_iW_i)\sin(\theta+\alpha_i)}{4\pi\eta_0}(1+\frac{1}{jk_0R}-\frac{1}{(k_0R)^2})\frac{e^{-jk_0R}}{R} \tag{3.76}$$

$$H_r = -j\frac{k_0(2V_iW_i)\cos(\theta+\alpha_i)}{2\pi\eta_0}(\frac{1}{jk_0R}-\frac{1}{(k_0R)^2})\frac{e^{-jk_0R}}{R} \tag{3.77}$$

where $W_i = W_p/4$, $j = \sqrt{(-1)}$, $R = \sqrt{(x_i-x_j)^2+(y_i-y_j)^2}$, $\theta = \tan^{-1}[(x_j - x_i)/(y_j - y_i)]$ and α_i is the angle between the normal $\vec{n}_i$ to the edge at (x_i, y_i) and the X-axis. The angle α_i is positive when measured from the X-axis towards the normal in the anticlockwise direction. The current density J_j induced in the jth subsection because of the magnetic fields generated by the ith current

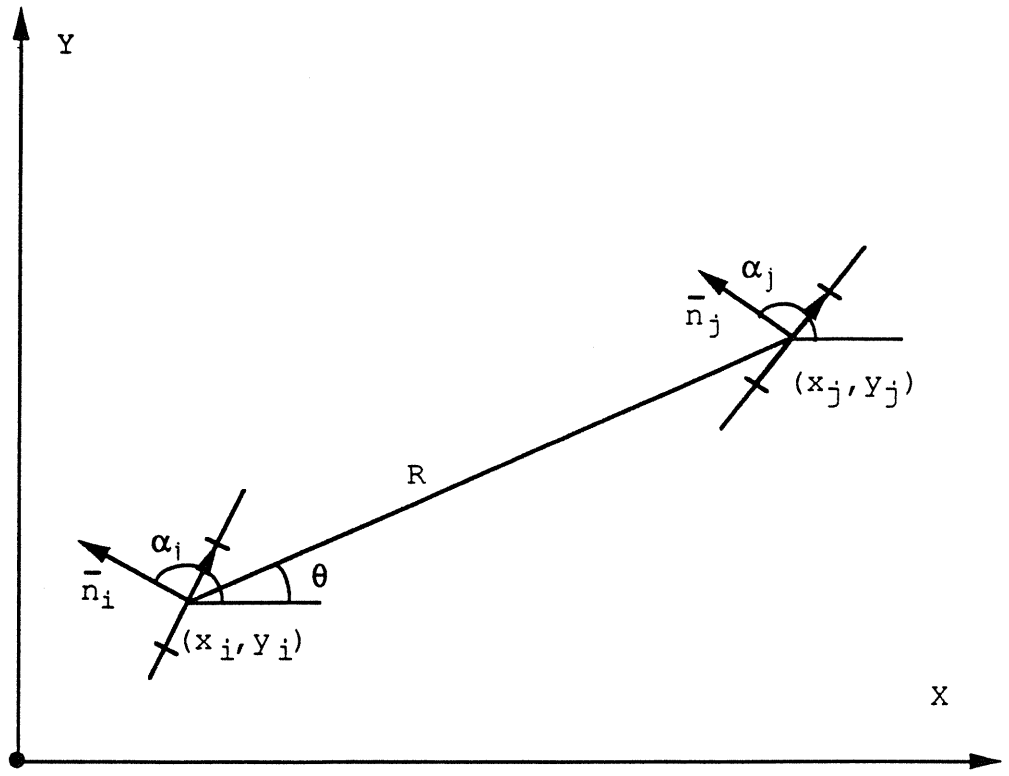

Figure 3.8. Coordinate definition for the computation of mutual coupling between two magnetic current elements

element is

$$J_j = -(\vec{a}_z \times \bar{H}).(\vec{n}_j) \tag{3.78}$$

In the x-y-z coordinates, $\vec{n}_j$ can be expressed as

$$\vec{n}_j = \vec{a}_x \cos\alpha_j \; + \; \vec{a}_y \sin\alpha_j \tag{3.79}$$

Using the above expressions, J_j is then

$$J_j = H_y \cos\alpha_j \; - \; H_r \sin\alpha_j \tag{3.80}$$

where

$$H_x \; = \; H_r \sin\theta \; + \; H_\theta \cos\theta \tag{3.81}$$

$$H_y \; = \; H_r \cos\theta \; - \; H_\theta \sin\theta \tag{3.82}$$

Since the width $W_j = W_p/4$ of the jth subsection is taken to be very small, the surface current density is considered to be uniform over W_j. So, the line current flowing in the jth subsection is

$$I_j = J_j W_j \tag{3.83}$$

The mutual admittance Y_{ij} between the ith and jth subsections is

$$Y_{ij} = J_j W_j / V_i \tag{3.84}$$

It may be pointed out that, since J_j is linearly proportional to V_i, the value of V_i is not needed for the computation of Y_{ij}. The mutual admittance Y_{pq} between elements p and q is obtained from the mutual admittances among subsections i and j

$$Y_{pq} = \sum_{j=q1}^{q4} \sum_{i=p1}^{p4} Y_{ij} \tag{3.85}$$

where $p1$, ..., $p4$ and $q1$, ..., $q4$ denote the four elements of sections p and q respectively.

For microstrip patches on thin substrate with a thick cover layer, the elements of the Y_{MCN} matrix are computed in a similar manner as the case without cover layer. However, the radiation conductance G_e and the magnetic field components are now evaluated in the presence of the cover layer. An approach based on the spectral domain for computing these quantities is given in [14].

3.4 Analysis Technique for the Patch

In this section we discuss how the MNM approach is to be used to compute the scattering parameters of the two-port gap-coupled patch and the voltage distributions at the edges of the patch and of the coupling line. The segmentation method [6] is used to combine the eigth sub-networks shown in *Fig.* 3.1. This is done by constructing two networks; an internal network and an external network. These networks are combined using Kirchhoff's voltage and current laws. The results of this computational step is the Z-matrix of the two-port patch and the voltages at the edges of the patch and the feedline. From the Z-matrix, the S-matrix can be easily obtained. From the knowledge of the edge voltages the radiation characteristics of the patch are obtained.

Z-matrix of Internal Network: The internal network includes TLI, TLG, TLO and PATCH networks. The Z-matrix characterizing this internal network is obtained as follow; i) first the TLO and TLG networks are combined, ii) the resulting network is then combined with the TLI network, iii) the ports of this resulting network are renumbered so that the input and the output ports are numbered first, iv) this resulting network is combined with the PATCH

network. The internal network has N2+3N1+8 ports.

Z-matrix of the External Network: The external network consists of EANL, GAP, EANP and MCN networks. The Z-matrix of this network is obtained by inverting the admittance matrix $[Y]_{EXT}$ obtained by combining these networks. The Y-matrix charaterizing the external network is obtained as follows; i) A network is constructed by combining EANL, EANP and GAP networks. The Y-matrix $[Y]_1$ characterizing this network is expressed as

$$[Y_1] = \begin{bmatrix} [Y]_{EANL} & 0 & 0 \\ 0 & [Y]_{GAP} & 0 \\ 0 & 0 & [Y]_{EANP} \end{bmatrix} \tag{3.86}$$

The admittance matrix $[Y]_1$ has (3N1+N2+6) rows because submatrix $[Y]_{EANL}$ has (N1+2) rows, submatrix $[Y]_{GAP}$ has (2N1+4) rows and submatrix $[Y]_{EANP}$ has N2 rows. ii) The MCN network is added to the resulting network to form the external network. Since the admittance matrix $[Y]_{MCN}$ characterizing the MCN network has only (N2+3N1) rows and since $[Y]_1$ has (N2+3N1+6) ports, the size of the MCN network is increased by 6 ports so that the Y-matrices characterizing the two networks can be added up. The elements of the $[Y]_2$ matrix charaterizing the new MCN network are obtained from $[Y]_{MCN}$ by proper renumbering of the ports. Hence, the Y-matrix $[Y]_{EXT}$ characterizing the external network is given by

$$[Y]_{EXT} = [Y]_1 + [Y]_2 \tag{3.87}$$

3.5 Design Methodology for the Patch

In this section we discuss a CAD procedure for the design of the gap-coupled rectangular microstrip patch to achieve a specified value of S_{21} as well

as to get $S_{11} = 0$ (input match). For example, specified values of S_{21} are required to achieve given amplitude distribution in a series-fed linear array of such patches. Furthermore, series-fed array elements are designed for $S_{11} = 0$, so the radiation is controlled by the power incident on the input port and not by the power incident at the output port which is the power reflected from the next array elements.

The design specifications of a gap-coupled rectangular patch include: i) substrate and cover layer parameters ii) frequency at which the patch is to resonate. The design parameters of the patch are: i) rectangular patch dimensions (width and length), ii) gap width, iii) characteristic impedances of the input line(s), of the section of line coupled to the patch and of the output line(s), iv) lengths of input and output line(s). As shown in *Fig.* 3.9, more than one section may be used at the input and the output ends.

The patch width and the gap width are the two main parameters which can be varied to obtain wide range of S_{21} values. However, values of S_{21} are not very sensitive to the value of characteristic impedance Z_0^G of section of line coupled to the patch. For given patch width, the gap width, the impedance Z_0^G and the length of the patch are adjusted to achieve resonance at the specified frequency. The resonant length is defined as the length which maximizes the power radiated from the patch (not necessarily S_{11}=0). Lower values of patch width b (high S_{21}) are limited by etching tolerance (usually $b > 1$ mm) and high values of patch width (low S_{21}) are limited by available spacing between array elements. Low values of gap width S (low S_{21}) are limited by etching tolerance (usually $S > 5$ mil) and high values of S (high S_{21}) result in very small coupling. The input and the output line sections are used

to achieve an input match ($S_{11} = 0$).

For the design of the gap-coupled patch for specified value of S_{21} and $S_{11} = 0$, there are two approaches. In the first approach, the patch and the feed network are modeled using the MNM approach as discussed earlier. The design parameters of the patch are systematically varied until the specifications are met. This can be done using a multidimensional optimization program. This approach is very time consuming and can be used only when designing few patches. However, when a large number of patches need to be designed (e.g. when designing a series-fed linear array), this approach is not efficient. An alternative approach is to use the MNM approach for the patch and the section of coupled line (denoted by region B in *Fig.* 3.9) and to use a transmission line analysis for the input and output sections (denoted by regions A and C in *Fig.* 3.9). An equivalent transmission line model for the gap-coupled patch is shown in *Fig.* 3.10. Look-up tables are then generated for region B for discrete values of the gap width and the patch width. A flow chart depicting various steps involved in generating the look-up tables for the second approach is shown in *Fig.* 3.11.

As shown in the flow chart, starting from the design specifications (substrate parameters and frequency) and selected values of patch width b, gap width S and characteristic impedance Z_0^G, the program computes the resonant patch length which maximizes the power radiated from the patch. This resonant patch length is computed using an optimization routine based on Brent's algorithm [15]. Look-up tables for [L] and [C] matrices of the asymmetric coupled line (consisting of patch and feed line) are generated for discrete values of a. These look-up tables are necessary since numerical evaluation of

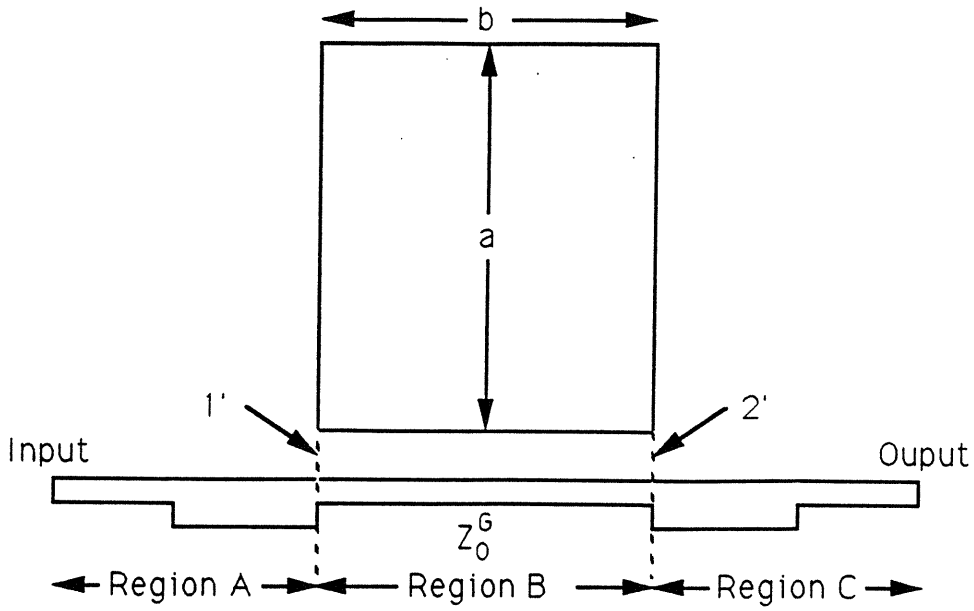

Figure 3.9. Gap-coupled patch with two sections of line connected at the input and the ouptut sides of the gap

[L] and [C] is computationaly intensive and their values depend on the patch length.

In the computation of the resonant length, additional sections of lines need to be connected to the input and the output of region B to account for feed junction reactances. The characteristic impedances of these extra sections are equal to Z_0^G and their lengths should be long enough so higher order modes will decay at the ends of these sections. Once the Z-matrix of the configuration is obtained, the S-matrix with respect to the input and the output extra sections of lines is computed. Then, the S-matrix with respect to the input and the ouput planes (1′ and 2′ shown in *Fig.* 3.9) is evaluated. The Z-matrix with respect to these planes is obtained from the S-matrix. The look-up tables

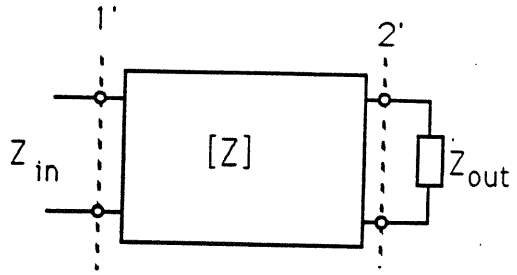

Figure 3.10. Equivalent transmission line model for computation of the input impedance of the patch at reference plane 1′

are generated for region B for various gap width and patch width and are independent of the parameters of input and the output regions (A and C).

The characteristic impedances and the lengths of the input and the output line sections are computed by using the equivalent lumped network shown in *Fig.* 3.10. The (2 × 2) Z-matrix (computed using MNM approach as discussed above) characterizes region B shown in *Fig.* 3.9. Impedance Z_{out}, shown in the figure, is the equivalent input impedance of region C. The input impedance of the combination of regions B and C is equal to

$$Z_{in} = Z_{11} - \frac{Z_{12}Z_{21}}{Z_{out} + Z_{22}} \tag{3.88}$$

Z_{out} is selected such that Z_{in} is purely real.

If the output line consists of one section only, the characteristic impedance of this section Z_0^O should be equal to Z_{out} to make Z_{in} real. If the characteristic impedance Z_0^O of the output line is chosen to be different than Z_{out} a quarter-wave section is inserted between the output line and the patch. The characteristic impedance of this quarter-wave section is equal to $\sqrt{Z_{out}Z_0^O}$. If the input line consists of one section only, the characteristic impedance of this section should be equal to Z_{in}. If the characteristic impedance of the input

line is chosen to be different from Z_{in}, a quarter-wave matching section need to be included between the patch and the input line.

3.6 Design and Analysis of Sample Patch:

As an example of the implementation of the CAD methodology, we consider a two-port gap-coupled patch with the following design parameters: substrate thickness h=1/64 inch (0.381 mm), dielectric constant $\epsilon_r = 2.2$, loss tangent $\tan\delta = 9 \times 10^{-4}$, metalization thickness $t = 18\mu m$, metalization conductivity $\sigma = 5.8 \times 10^7$ S/m, surface roughness=$1\mu m$, operating frequency f=13 GHz and without any cover layer. The characteristic impedance Z_0^G of the microstrip feed line is 50 Ω (line width =1.165 mm).

3.6.1 [L] and [C] Matrices: The asymmetric coupled line parameters [L] and [C] are evaluated using the software package based on quasi-static moment method approach [12]. [L] is the matrix of line inductances per unit length (in H/m), [C] is the matrix of line electrostatic induction coefficients per unit length (in F/m). Matrices [L] and [C] are computed for the case of an infinite ground plane with finite conductor thickness (t=18 μm) and finite conductivity ($\sigma = 5 \times 10^7$ S/m). The microstrip feed line is denoted as conductor #1 and the patch as conductor #2. Tables 4.1 to 4.8 show the elements of matrices [L] and [C] as a function of patch length a (width of conductor #2) varying from 6.8 mm to 8 mm. The discrete values of length a are selected such that the resonant length of the patch (for f=13 GHz) is within minimum (6.8 mm) and maximum (8.0 mm) values. These minimum and maximum values are 8% lower and higher than the computed resonant length of the unloaded patch (7.4 mm). The line parameters are computed for every 0.2 mm step. The discrete values of gap width 5, 10, 20 and 40 mils are selected

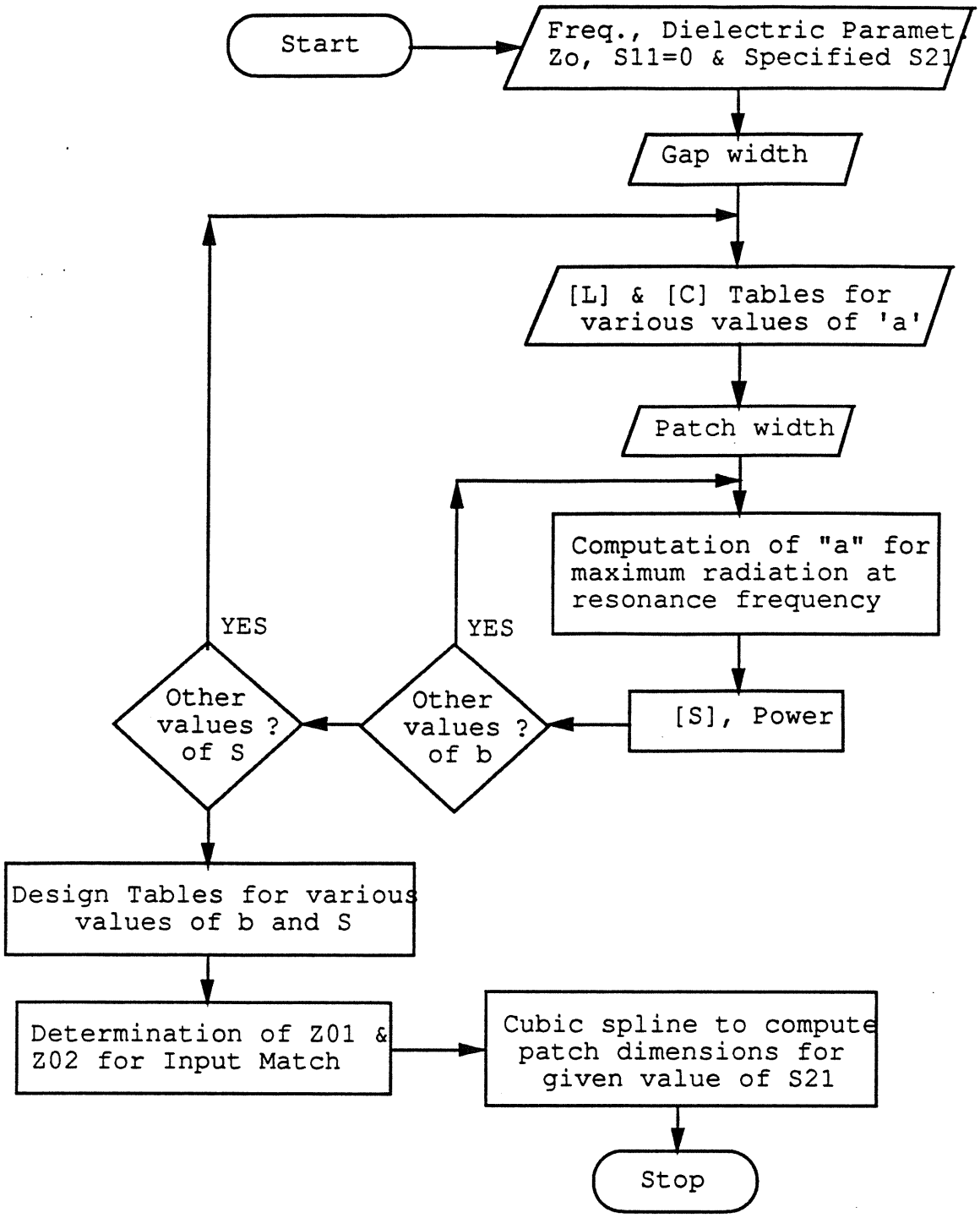

Figure 3.11. Flow chart for design procedure of gap-coupled rectangular microstrip patch

Table 3.1: Elements of capacitance matrix [C] for gap width $S = 5$ mils

amm)	C_{11}	C_{12}=C_{21}	C_{22}
6.8	98.43	-19.725	394.7
7.0	98.43	-19.670	405.0
7.2	98.43	-19.680	415.4
7.4	98.43	-19.675	425.8
7.6	98.43	-19.705	436.2
7.8	98.42	-19.680	453.8
8.0	98.42	-19.705	456.9

All capacitances are in pF/m.

to obtain a wide range of power radiated from the patch. The configuration of the designed patch is shown in *Fig.* 3.14.

3.6.2 Evaluation of resonant length: As depicted in the flow chart shown in Figure 3.11, the first part of the design procedure consists of evaluating the length of the patch a which maximizes the power radiation from the patch. Using the first program of the software (program DESIGN), Figure 3.12 shows the fractional power radiated from the patch as a function of the patch length a from 7.2 mm to 7.6 mm. The patch width is selected to be 5 mm and the gap width is selected to be 40 mil. As shown in the figure, the maximum power radiated is 4.38 % and corresponds to a patch length a=7.52 mm.

Table 3.2: Elements of inductance matrix [L] for gap width $S = 5$ mils

a (mm)	L_{11}	$L_{12}=L_{21}$	L_{22}
6.8	206.2	16.53	58.46
7.0	206.1	16.13	57.02
7.2	206.0	15.76	55.65
7.4	205.9	15.40	54.35
7.6	205.9	15.06	53.11
7.8	205.8	14.73	51.92
8.0	205.7	14.41	50.79

All inductances are nH/m.

Table 3.3: Elements of capacitance matrix [C] for gap width $S = 10$ mils

a (mm)	C_{11}	$C_{12}=C_{21}$	C_{22}
6.8	94.42	-13.315	390.6
7.0	94.42	-13.315	401.0
7.2	94.42	-13.320	411.4
7.4	94.42	-13.340	421.7
7.6	94.42	-13.340	432.1
7.8	94.42	-13.345	442.4
8.0	94.42	-13.365	453.8

All capacitances are in pF/m.

Table 3.4: Elements of inductance matrix [L] for gap width $S = 10$ mils

a (mm)	L_{11}	$L_{12}=L_{21}$	L_{22}
6.8	216.2	12.69	58.84
7.0	216.2	12.39	57.39
7.2	216.1	12.11	56.00
7.4	216.1	11.83	54.68
7.6	216.0	11.57	53.42
7.8	216.0	11.32	52.22
8.0	215.9	11.08	51.08

All inductances are nH/m.

Table 3.5: Elements of capacitance matrix [C] for gap width $S = 20$ mils

a (mm)	C_{11}	$C_{12}=C_{21}$	C_{22}
6.8	92.29	-7.8595	388.3
7.0	92.29	-7.8695	398.7
7.2	92.29	-7.8425	409.1
7.4	92.29	-7.9070	419.4
7.6	92.29	-7.8770	429.8
7.8	92.29	-7.9060	440.2
8.0	92.29	-7.9105	450.6

All capacitances are in pF/m.

Table 3.6: Elements of inductance matrix [L] for gap width $S = 20$ mils

a (mm)	L_{11}	$L_{12}=L_{21}$	L_{22}
6.8	222.8	8.7100	59.07
7.0	222.7	8.5085	57.61
7.2	222.7	8.3165	56.21
7.4	222.7	8.1335	54.88
7.6	222.7	7.9580	53.61
7.8	222.6	7.7900	52.41
8.0	222.6	7.6295	51.25

All inductances are nH/m.

Table 3.7: Elements of capacitance matrix [C] for gap width $S = 40$ mils

a (mm)	C_{11}	$C_{12}=C_{21}$	C_{22}
6.8	91.58	-3.9505	387.5
7.0	91.58	-3.9730	397.8
7.2	91.58	-3.9705	408.2
7.4	91.58	-3.9915	418.6
7.6	91.58	-3.9940	429.0
7.8	91.58	-4.0145	439.3
8.0	91.58	-4.0280	449.7

All capacitances are in pF/m.

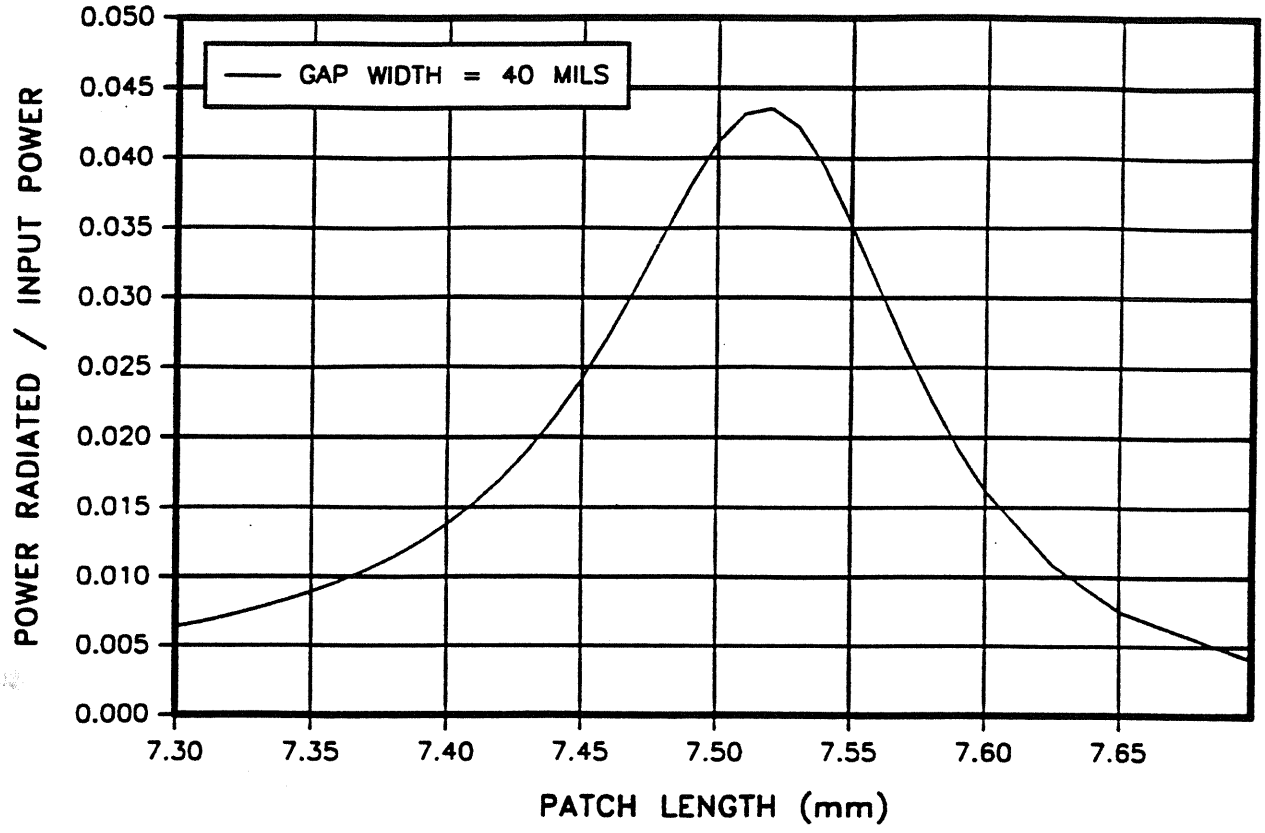

Figure 3.12. Variation of fractional power radiated as a function of the length of gap-coupled rectangular microstrip patch

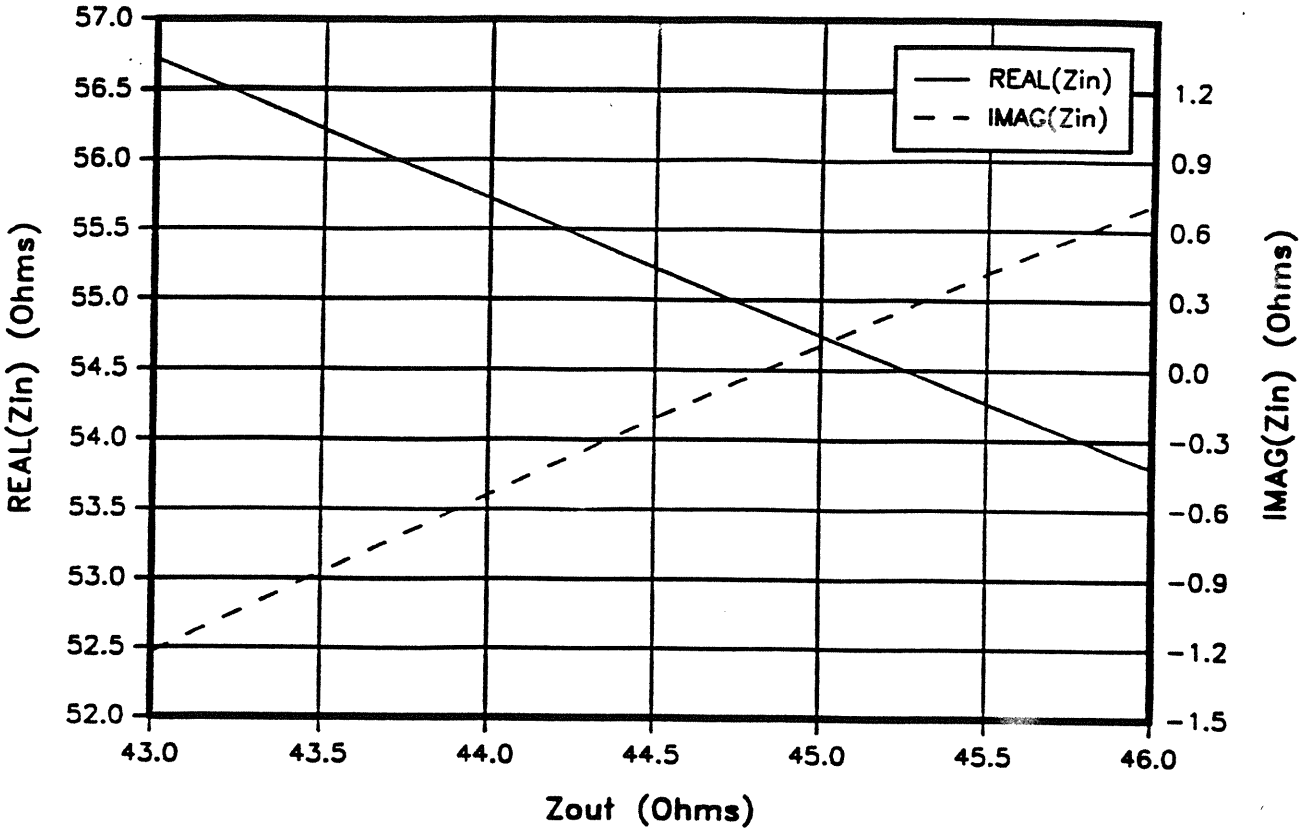

Figure 3.13. Variation of input impedance of gap-coupled rectangular microstrip patch with load impedance

Table 3.8: Elements of inductance matrix [L] for gap width $S = 40$ mils

a (mm)	L_{11}	$L_{12}=L_{21}$	L_{22}
6.8	225.5	5.1580	59.16
7.0	225.5	5.0450	57.69
7.2	225.5	4.9365	56.29
7.4	225.5	4.8330	54.96
7.6	225.5	4.7335	53.69
7.8	225.5	4.6380	52.47
8.0	225.5	4.5465	51.32

All inductances are nH/m.

3.6.3 Design of input and output feed lines: As shown in the flow chart of Figure 3.11, the second part of the design of the patch is the determination of the load impedance Z_{out} which should appear at the ouput port to achieve an input match. Figure 3.13 shows the variation of the input impedance as a function of the load impedance Z_{out} (shown in Figure 3.10). As shown in Figure 3.13, the input impedance at port 1′ is purely real (=54.98 Ω) when Z_{out} = 44.75 Ω. Hence, to realize an input match at port 1, we use one section of characteristic impedance = Z_{out} (line width =1.358 mm) at the output side. Furthermore, we use one section of characteristic impedance =54.98 Ω (line width=0.9931 mm) at the input side. The configuration of the designed patch is shown in *Fig.* 3.14.

3.6.4 Performance of the designed patch: In this section we present the performance of the patch designed above. These results are obtained using the analysis part of the software (program ANALYZE). Figure 3.15 shows the variation of input reflection coefficient S_{11} (after matching) as

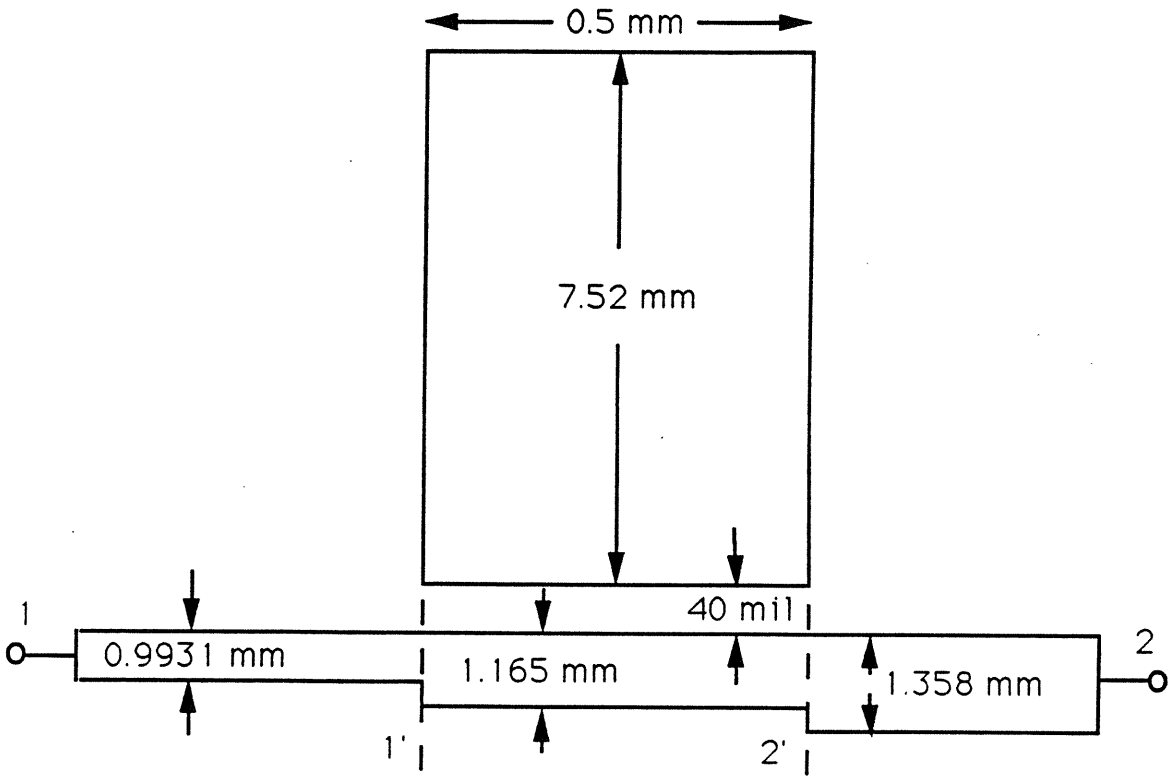

Figure 3.14. Configuration of the designed gap-coupled rectangular microstrip patch

a function of frequency from 12.5 GHz to 13.5 GHz. The reflection coefficient S_{11} (after matching) is normalized to 44.75Ω at the output and to 54.98Ω at the input. Shown also on *Fig.* 3.15 are the corresponding values of S_{11} (before matching and normalized to 50Ω at both input and the output ports) of region B shown in *Fig.* 3.9. In the range of frequency considered, S_{11} (before matching) remains better than -28 dB. Figures 3.16 and 3.17 show the magnitude and the phase of the transmission coefficient S_{21} respectively (after matching). The magnitude of S_{21} is minimum at the resonance frequency 13.5 GHz. The values of phase of S_{21} are with respect to reference planes 1′ and 2′ (shown in *Fig.* 3.9). The variation in the values of phase of S_{21} is less than 8° over the frequency range.

Figure 3.18 shows the variation of the fractional power radiated (relative to the input power) and the fractional power loss (dielectric and conductor) as a function of frequency (after matching). As shown in the figure, the fractional power radiated is still maximum at f=13 GHz and is equal to 4.46%. As shown in the figure the power loss increases slightly at resonance. Figures 3.19 and 3.20 show the H-plane and the E-plane far field patterns of the patch respectively. The beamwidth in the H-plane is 86° and is 110° in the E-plane. The computed directivity of the patch (from the integration of far-field pattern) is 6.8 dB.

3.7 Results for a patch without a cover layer

To check the accuracy of the MNM approach for gap-coupled patches, a two-port patch without a cover layer has been fabricated and tested. The patch is etched on a dielectric substrate with following specifications: substrate thickness h=1/32 inch (0.79 mm), dielectric constant $\epsilon_r = 2.2$, loss tangent

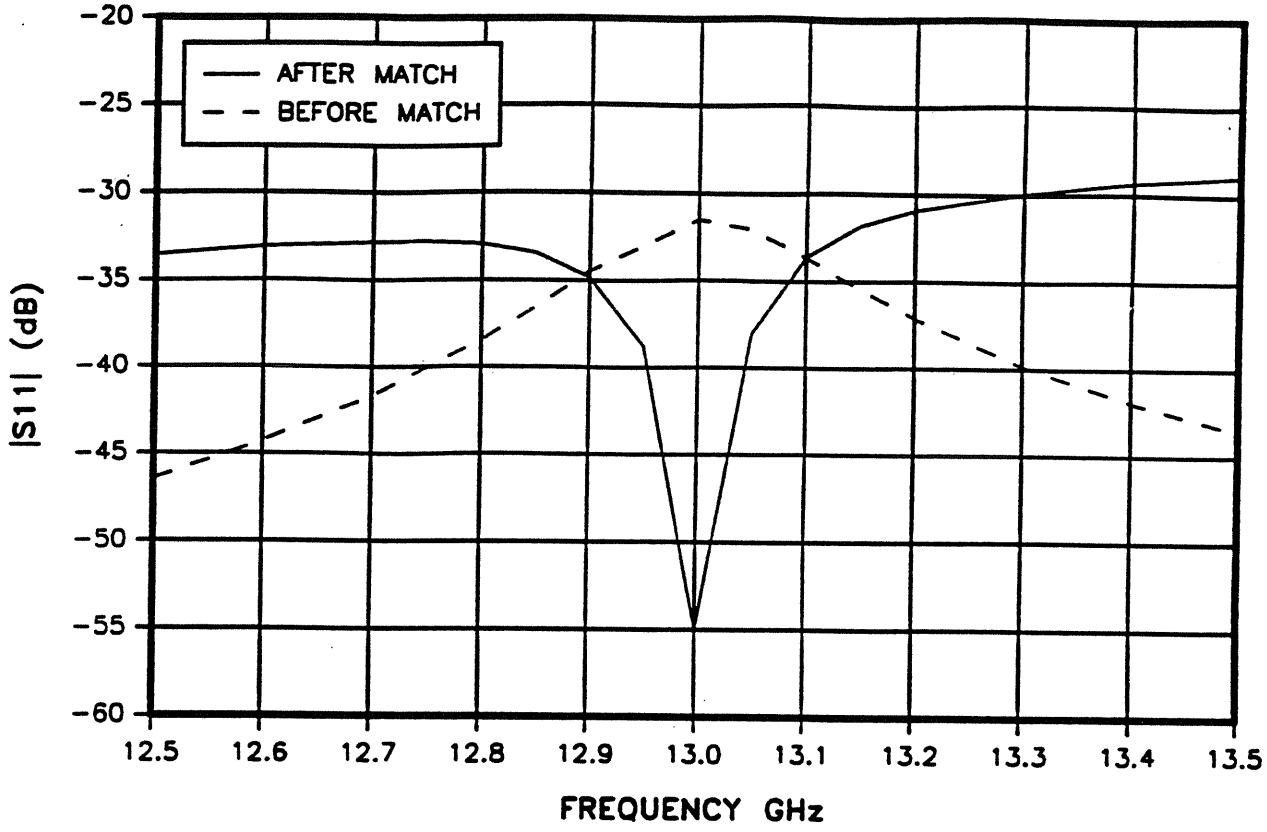

Figure 3.15. $|S_{11}|$ for the gap-coupled rectangular microstrip patch before and after match

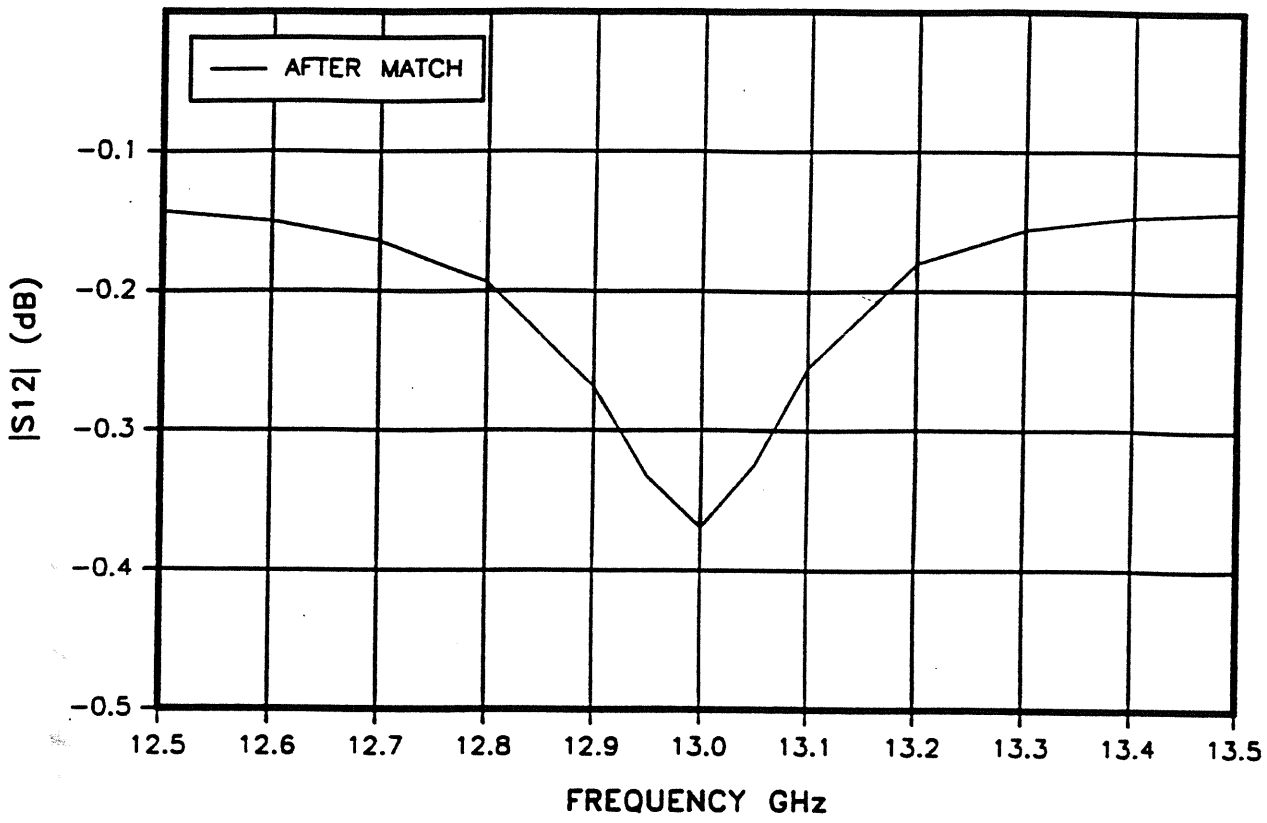

Figure 3.16: Magnitude of S_{12} for gap-coupled rectangular microstrip patch

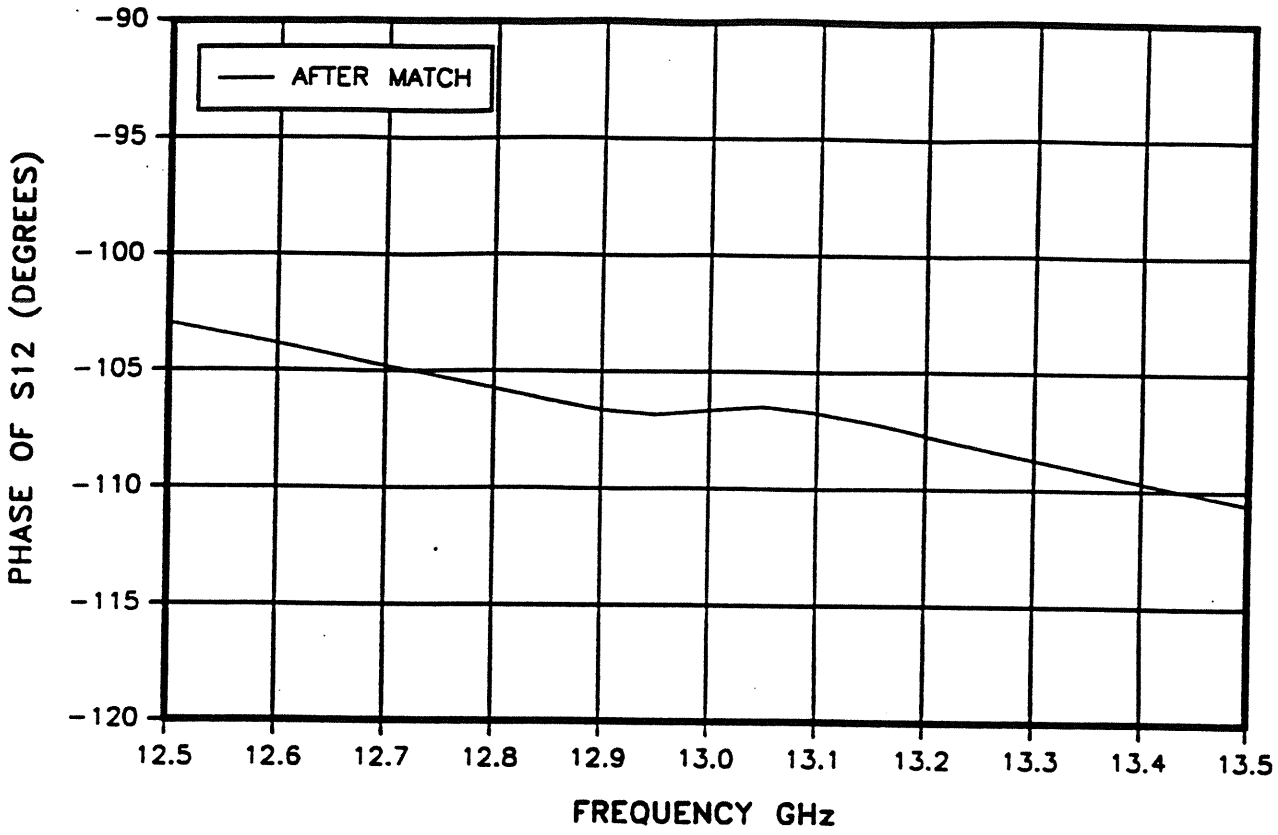

Figure 3.17: Magnitude of S_{12} for gap-coupled rectangular microstrip patch

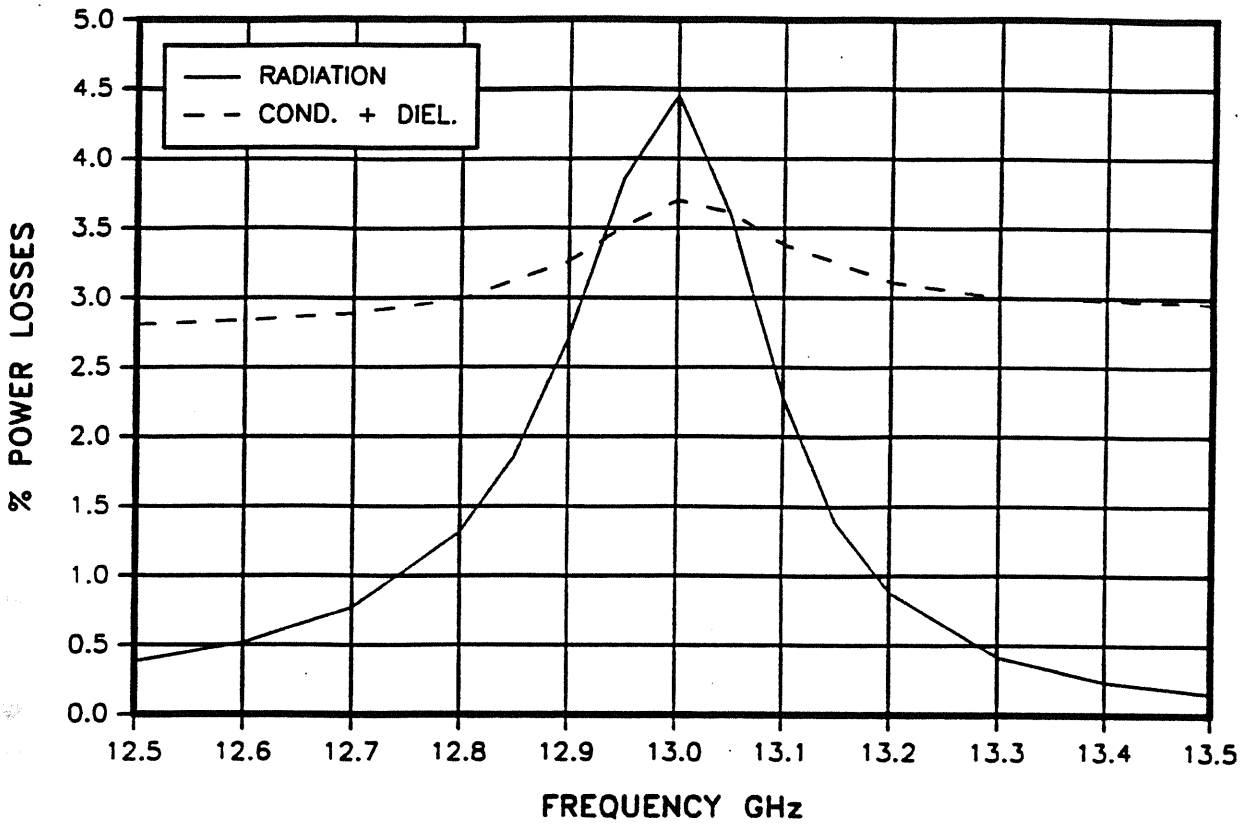

Figure 3.18. Fractional power radiated and power loss for gap-coupled rectangular microstrip patch

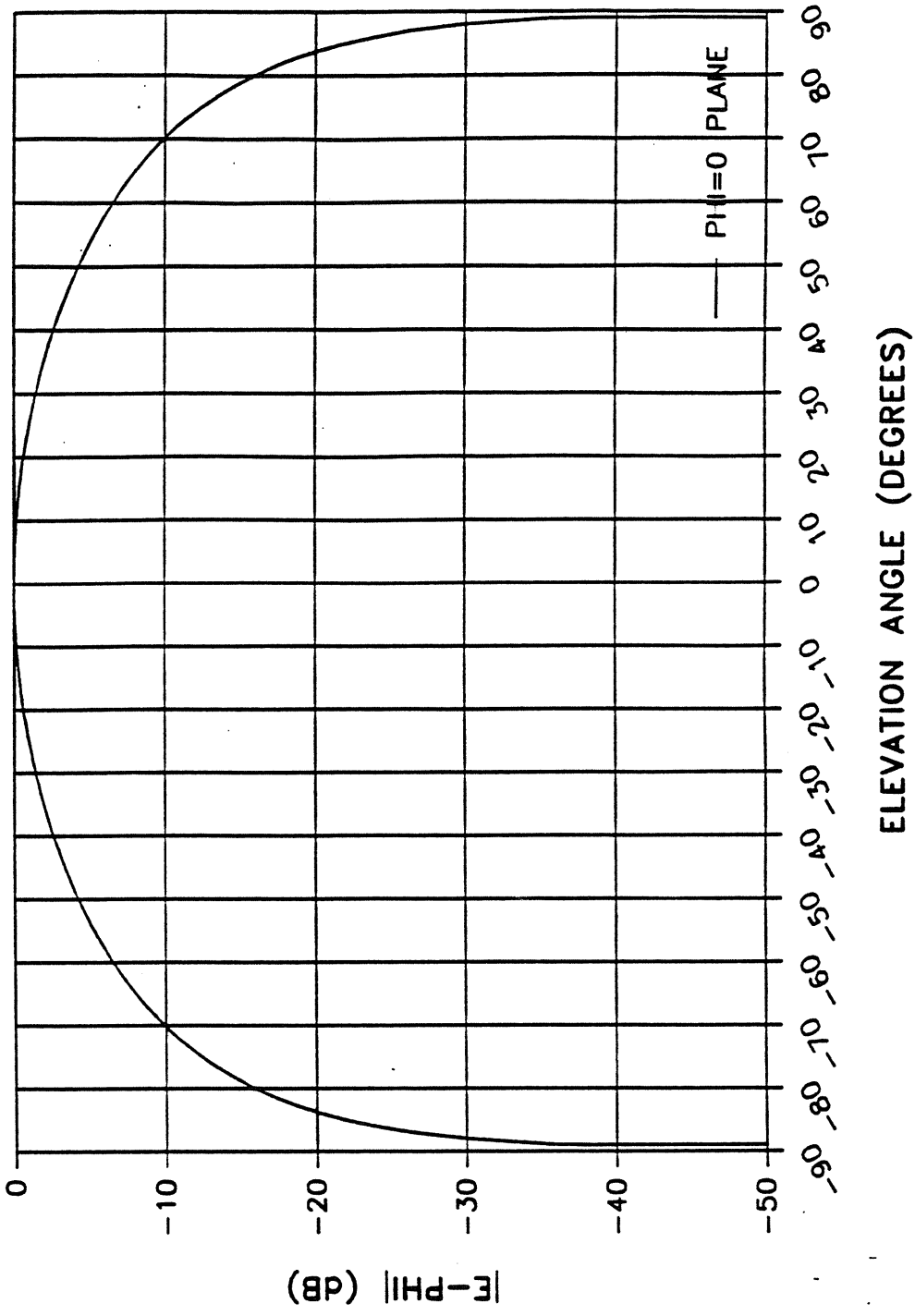

Figure 3.19. H-plane far-field pattern of the gap-coupled rectangular microstrip patch

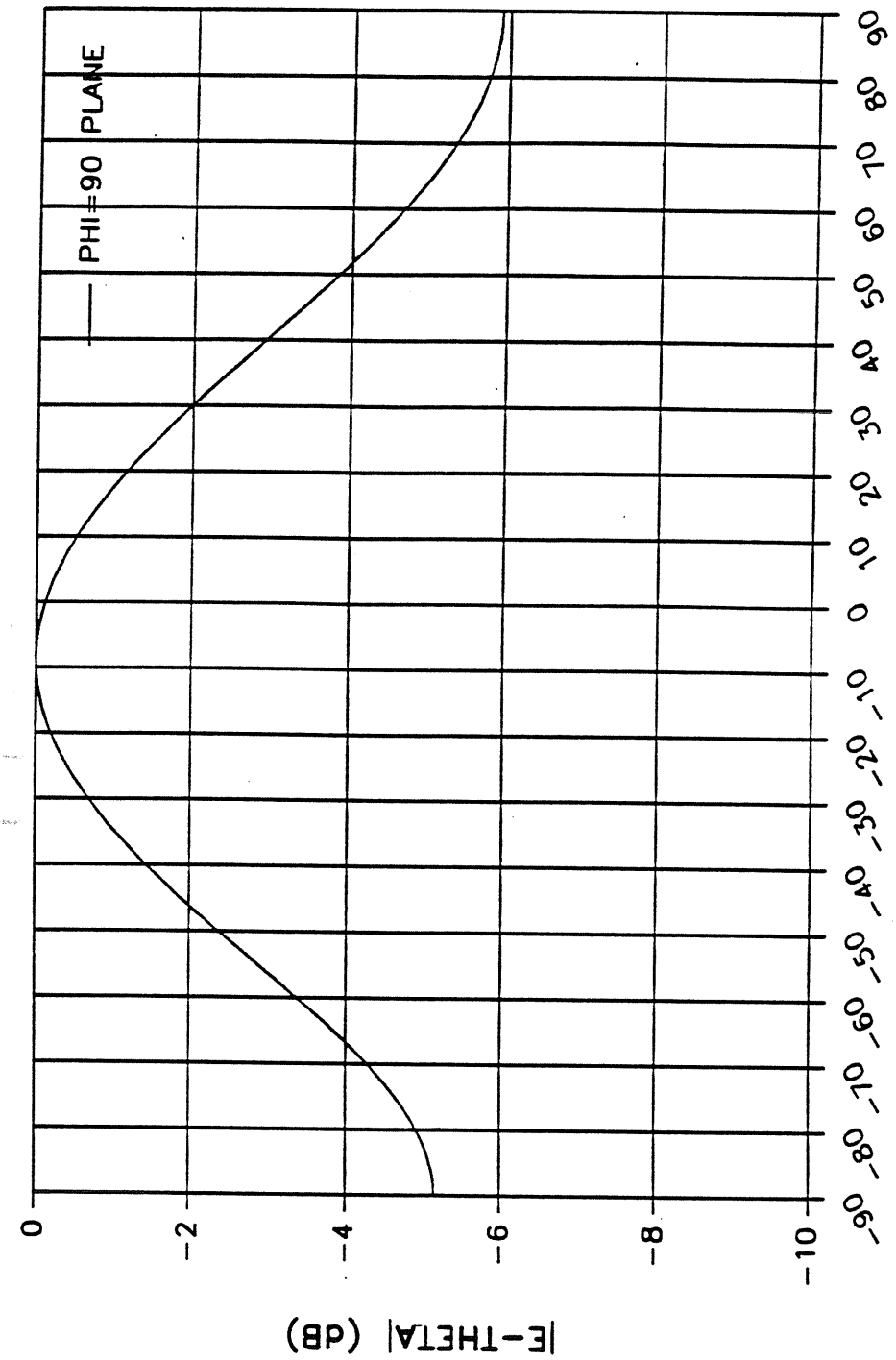

Figure 3.20. E-plane far-field pattern of the gap-coupled rectangular microstrip patch

$\tan\delta = 9 \times 10^{-4}$, metalization thickness $t = 18\mu m$, metalization conductivity $\sigma = 5.8 \times 10^7$ S/m, surface roughness=$1\mu m$. The dimensions of the patch are: a=32.84 mm, b=40 mm, s=20 mil and $W_I = W_0 = W_G = 2.44$ mm.

Figure 3.21 shows a comparison between the measured and the calculated results for $|S_{11}|$ from 2.9 GHz to 3.1 GHz. The measurement was done on the HP 8510 Network Analyzer using a TRL calibration. The discrepancy between the measured and caclulated resonance frequencies is very small. However, the measured values of $|S_{11}|$ are 3 dB lower than the calculated values. This may be due to inaccuracy in the modeling of line losses in the MNM approach. Also shown on Fig 3.21, are the results based on the full wave analysis code (PMESH) [18].

Figure 3.22 shows a comparison among MNM, PMESH and measurement for the magnitude of the transmission coefficient $|S_{21}|$. The calculated minimum value of $|S_{21}$, based on the MNM approach, is 0.55 dB lower than the measured value. However, the calculted value based on PMESH is 0.3 dB higher than the measured value.

Figure 3.23 shows a comparison among MNM, PMESH and measurement for the phase of S_{21} from2.9 GHz to 3.1 GHz. The calculated and measured values are within 2 degrees. The agreement between the measurement an the calculated results using MNM approach is very good.

A fairly good agreement between the MNM approach, the full-wave method and experiment is obatined and this proves the accuracy of the MNM approach for gap-coupled rectangular patches.

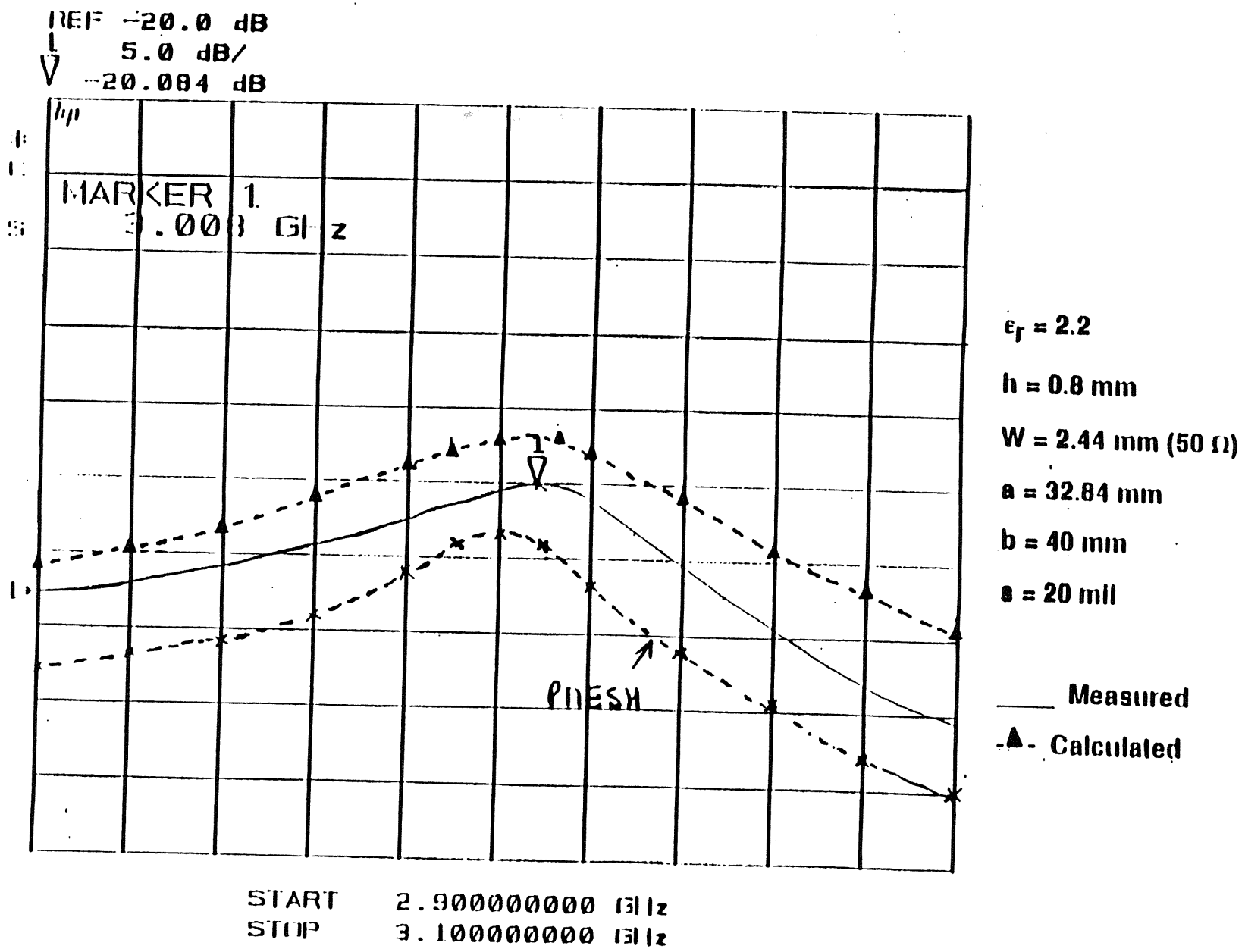

Figure 3.21. Comparison of calculated and measured values for $|S_{11}|$ of a rectangular gap-coupled patch without cover layer

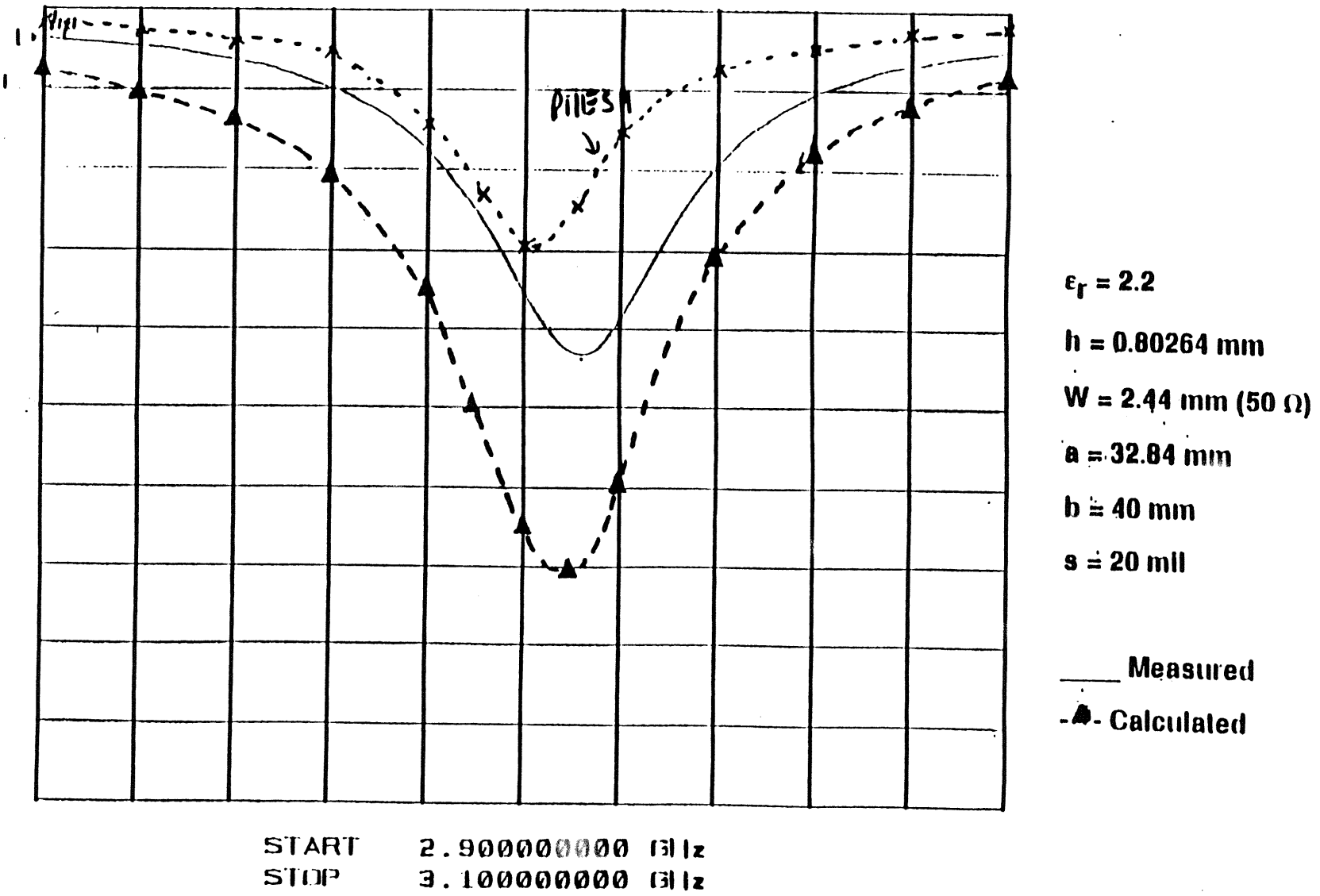

Figure 3.22. Comparison of calculated and measured values for $|S_{21}|$ of a rectangular gap-coupled patch without cover layer

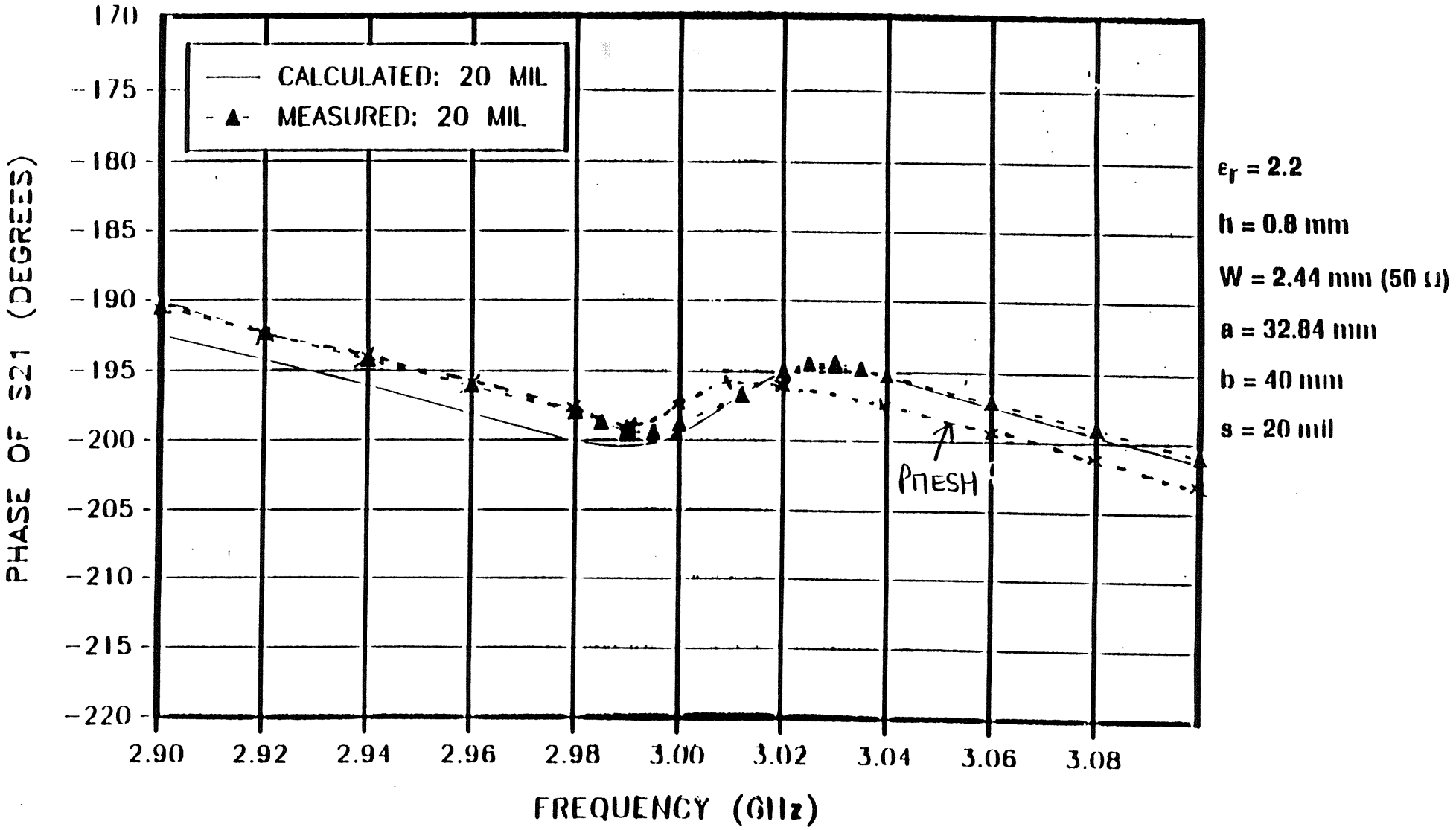

Figure 3.23. Comparison of calculated and measured values for phase of S_{21} of a rectangular gap-coupled patch without cover layer

3.8 Results for a patch with a cover layer:

In this section we compare the results based on the MNM approach and the full-wave analysis for a gap-coupled patch with a thick cover layer. The patch is etched on a dielectric substrate with following specifications: substrate thickness h=1/32 inch (0.79 mm), dielectric constant $\epsilon_r = 2.2$, loss tangent $\tan\delta = 9\times10^{-4}$, metalization thickness $t = 17.78\mu m$, metalization conductivity $\sigma = 5.8 \times 10^7$ S/m, surface roughness=$1\mu m$. The cover layer parameters are: thickness h=1/10 inch (2.54 mm), dielectric constant $\epsilon_r = 2.2$. The dimensions of the patch are: a=31.891 mm, b=20 mm, s=1 mm and $W_I = W_0 = W_G =$ 2.156 mm.

Figure 3.24 shows a comparison between the measured and the calculated results for $|S_{11}|$ from 2.5 GHz to 3.5 GHz. The calculated resonance frequency (corresponding to maximum $|S_{11}|$) using MNM approach is 3. GHz. The corresponding calculated value based on PMESH is 3.03 GHz (1% higher than MNM). Figure 3.25 shows a comparison between MNM approach and full-wave method for the magnitude of the transmission coefficient $|S_{21}|$. The calculated minimum value of $|S_{21}$, based on the MNM approach, is 0.8 dB lower than the full-wave value. Figure 3.26 shows a comparison between MNM and full-wave results for the phase of S_{21} from 2.5 GHz to 3.5 GHz. The calculated results using MNM approach are in good agreement with calculated results using the full-wave method.

A fairly good agreement between the MNM approach, the full-wave method and experiment is obtained and this proves the accuracy of the MNM approach for gap-coupled rectangular patches with a thick cover layer.

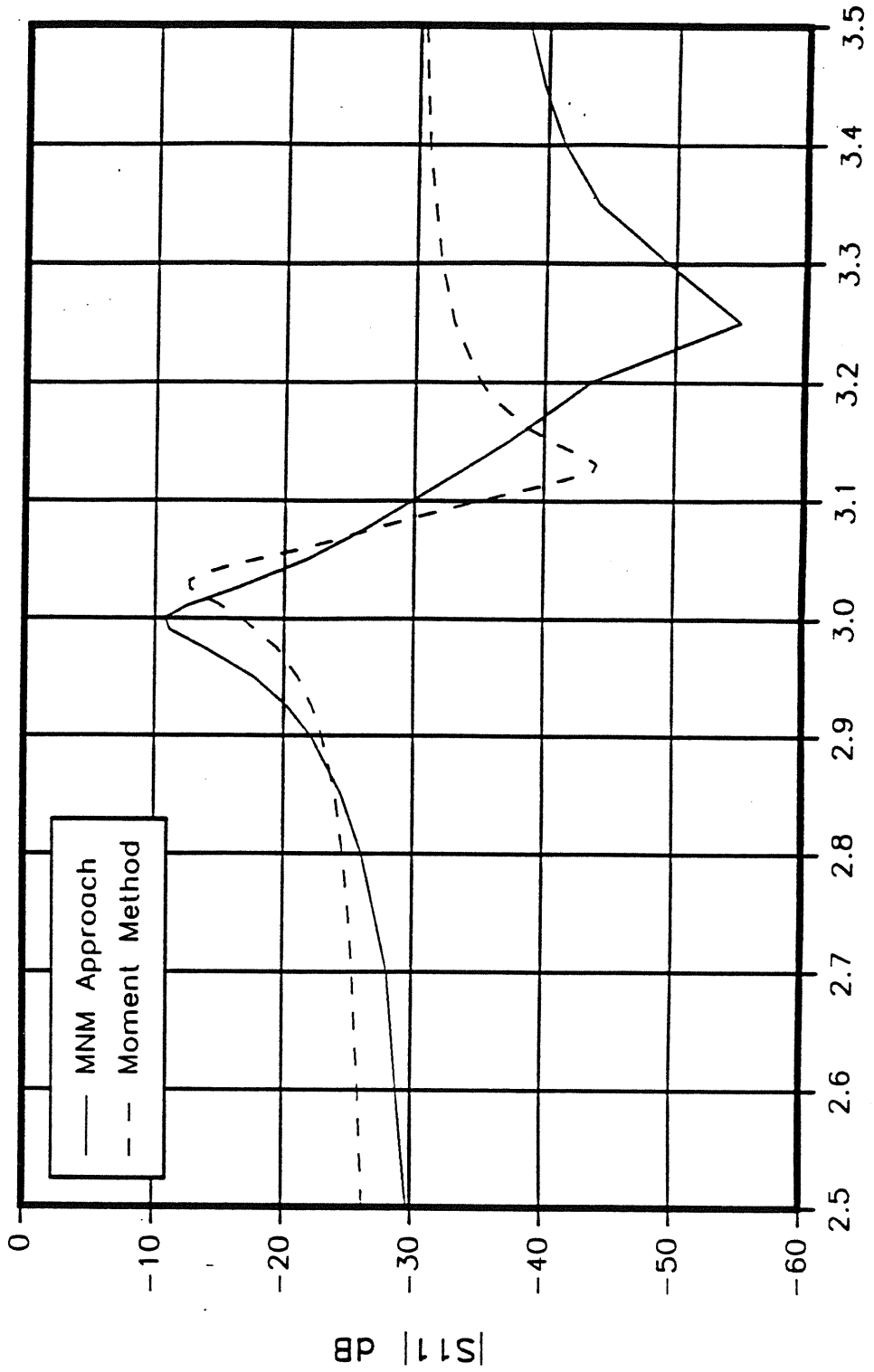

Figure 3.24. Comparison of calculated and measured values for $|S_{11}|$ of a rectangular gap-coupled patch wit a thick cover layer

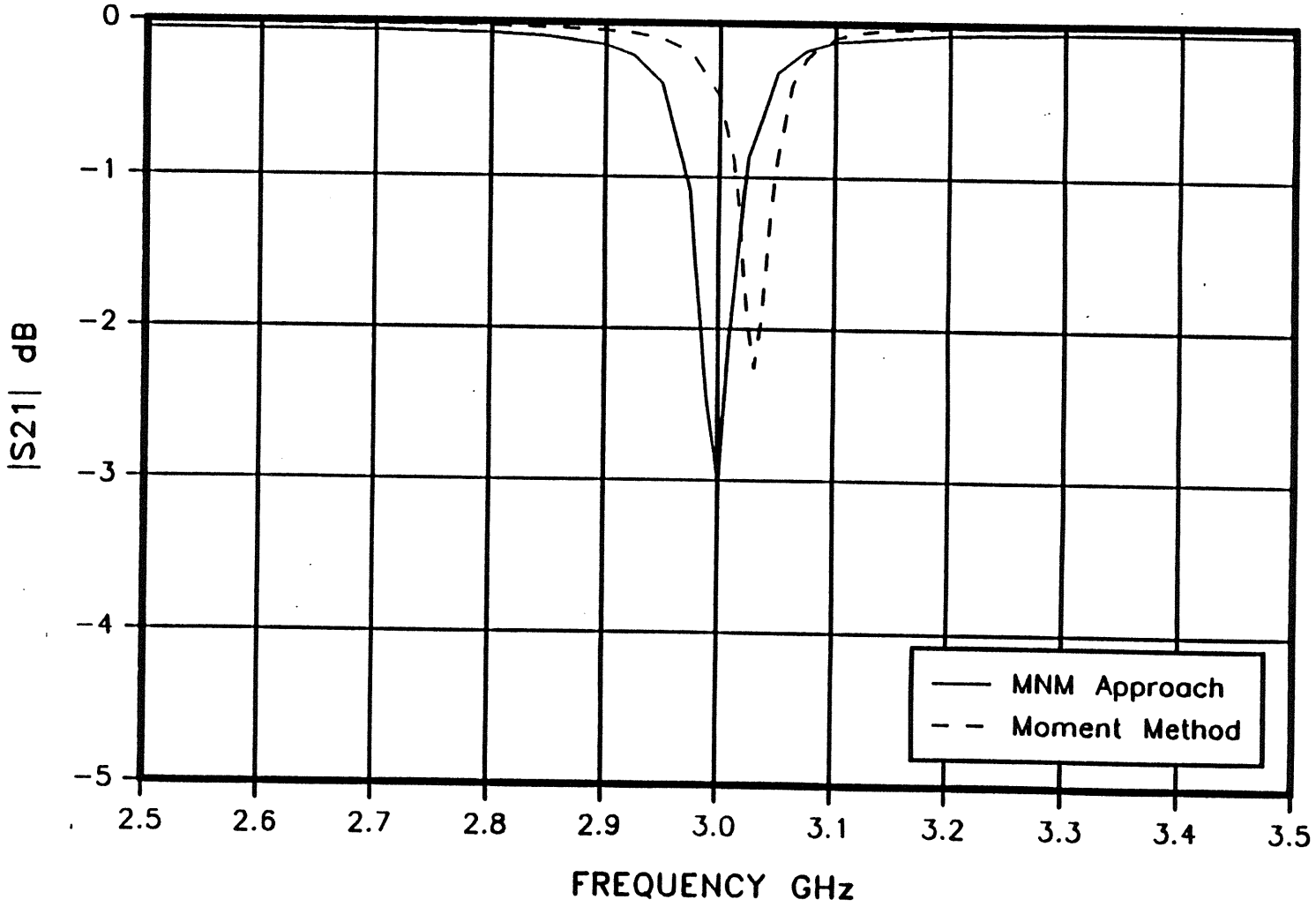

Figure 3.25. Comparison of calculated and measured values for $|S_{21}|$ of a rectangular gap-coupled patch with a thick cover layer

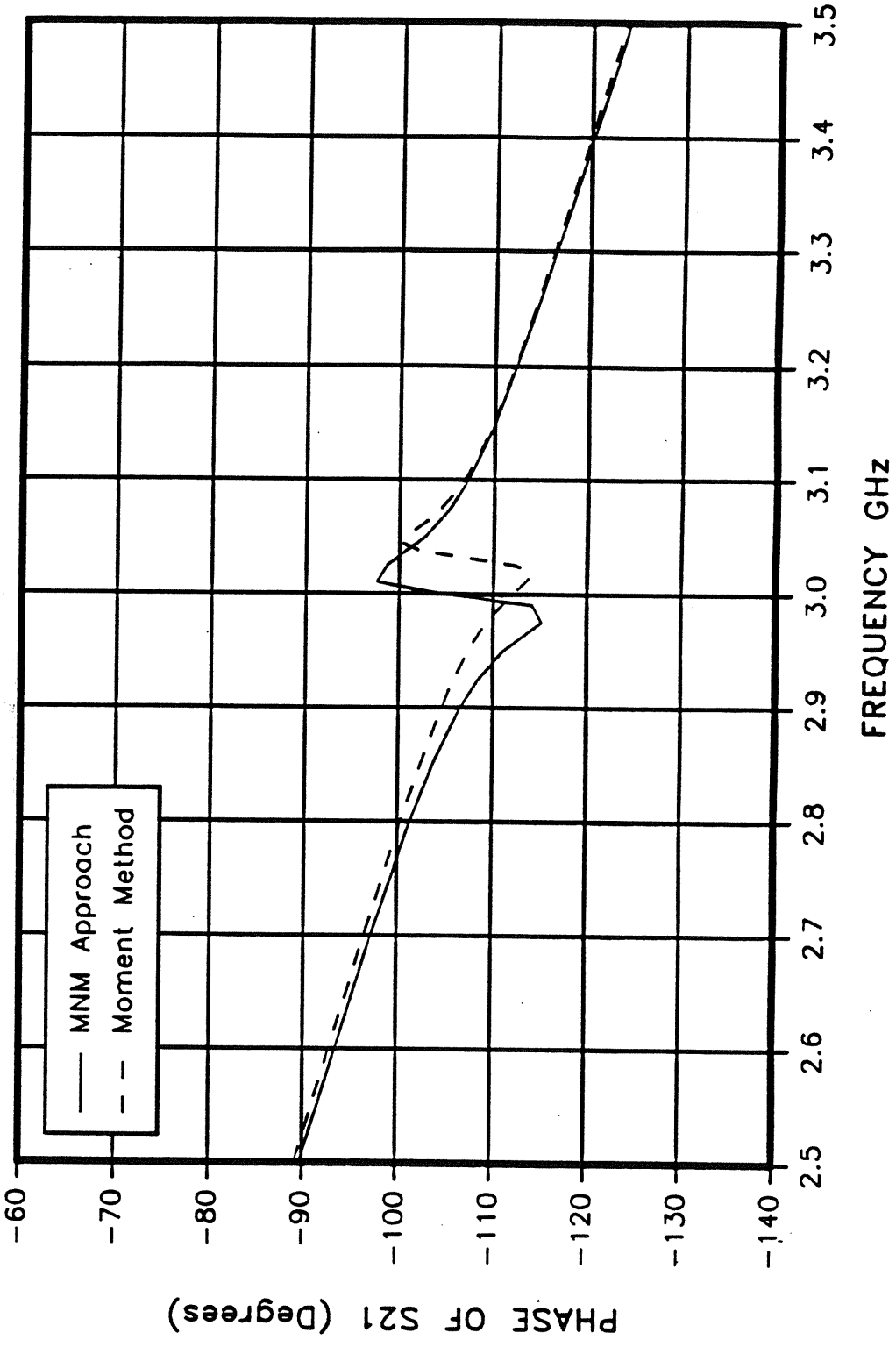

Figure 3.26. Comparison of calculated and measured values for phase of S_{21} of a rectangular gap-coupled patch with a thick cover layer

CHAPTER 4

MNM APPROACH FOR SERIES-FED ARRAYS

In this chapter, we discuss the extension of the MNM approach to the design and the analysis of linear arrays of gap-coupled rectangular microstrip patches. A configuration of a linear series-fed array of two-port gap-coupled patches is shown in Fig 4.1. In this configuration, the power is fed to the array at one end. A fraction of this input power is radiated by the first element, the remaining (less losses) is transmitted to the next element and so on. The power remaining at the far end of the array end is dissipated in a matched load. This array can be considered as a cascade of unit cells. Each unit cell (shown in Fig 4.2) consists of a rectangular microstrip patch gap-coupled to a section of a microstrip line and sections of lines connected to the input and output ports. In Section 1, a design methodology for series-fed arrays with and without cover layer is presented. The effects of array losses (dielectric and conductor) are included in the design. However, the effects of mutual coupling among array elements are neglected. Array analysis technique is given in Section 2. The design and analysis of a sample linear array without any cover layer is given in Section 3.

4.1 Array Design Methodology

A flow chart depicting the various steps involved in the design of the series-fed array is shown in Fig 4.3. This flow chart is identicial to the one used for series-fed arrays of directly-fed two-port patches [14]. Starting

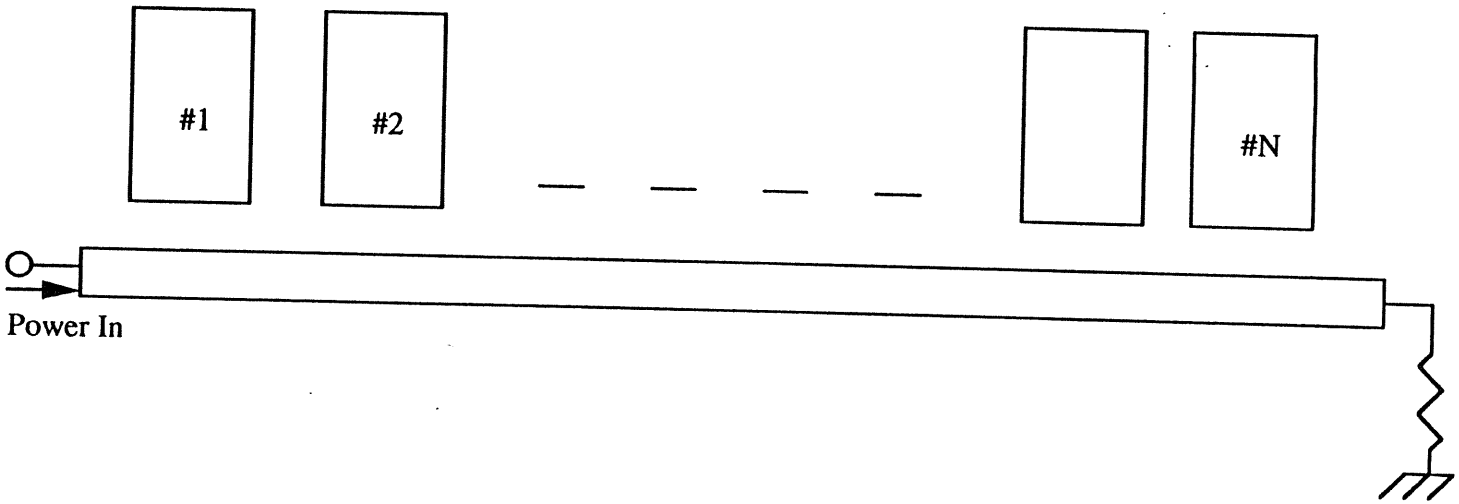

Figure 4.1. Configuration of a linear series-fed array of two-port gap-coupled rectangular microstrip patches

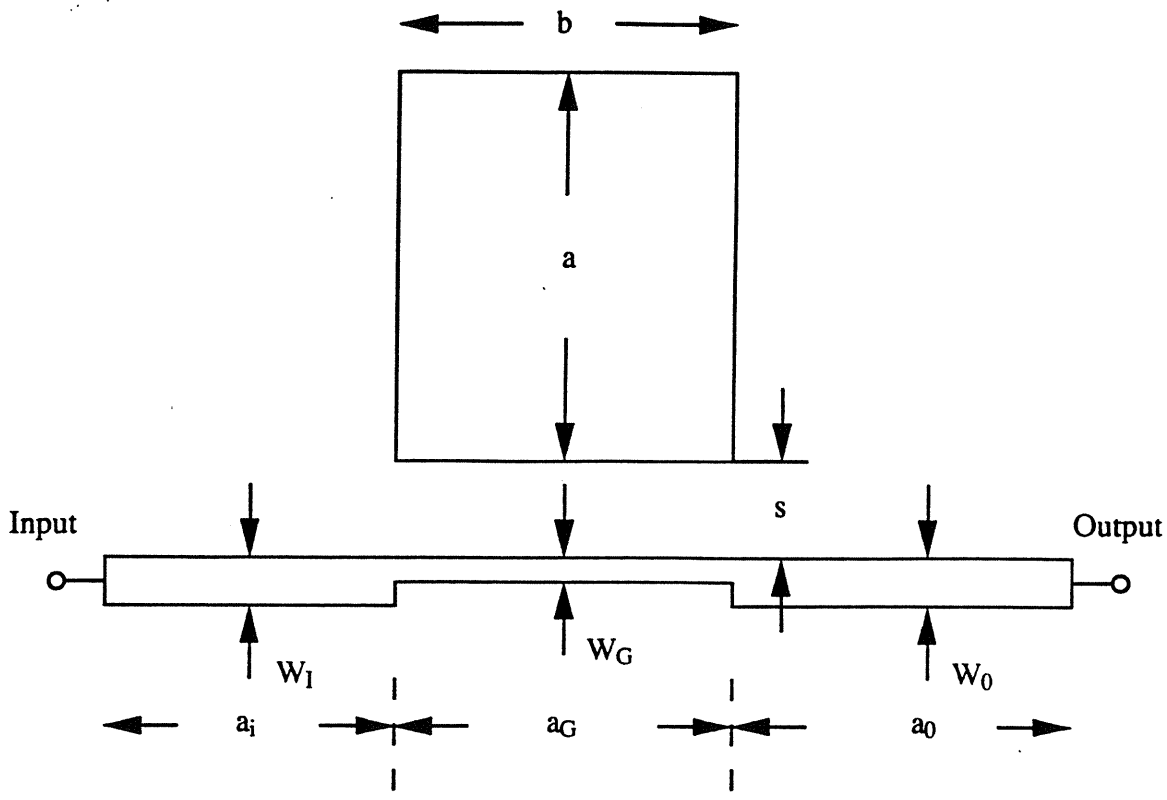

Figure 4.2: Typical unit cell in a series-fed array of Figure 4.1

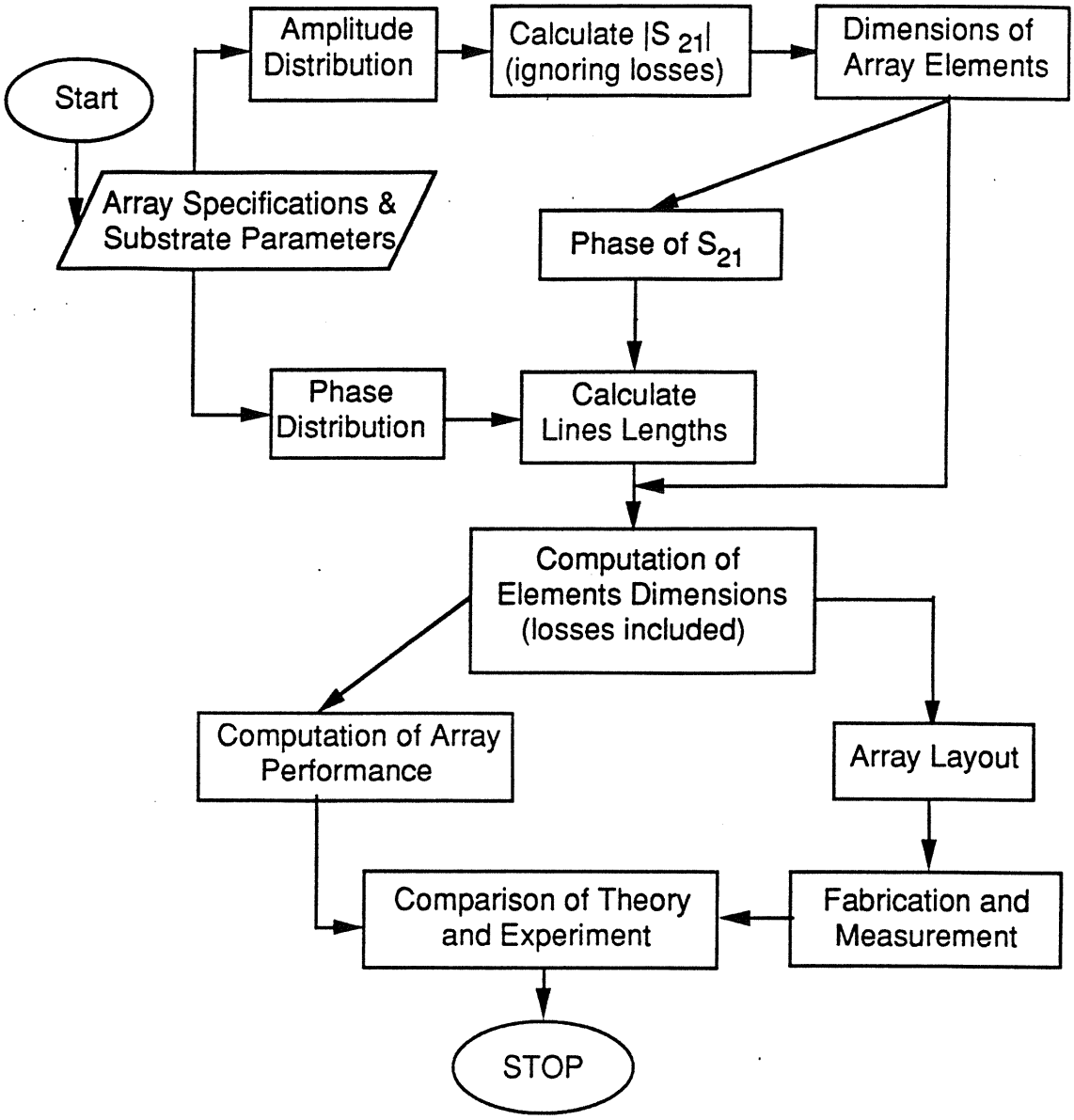

Figure 4.3. Flow chart for the CAD of series-fed linear arrays of gap-coupled rectangular patches

from the array specifications, the user selects the substrate parameters and the array amplitude (Taylor, Tchebyshev, etc..) and phase distributions. From the amplitude distribution, the required transmission coefficients for each of the two-port unit cells are computed. A method for computing the required transmission coefficients from the specified amplitude distribution of various units cells without considering array losses is discussed in [14].

The array losses are included in an iterative manner. Starting from the lossless case, unit cells are designed to meet the $|S_{21}|$ distribution. The losses associated with these unit cells are computed using the MNM approach. These losses are then used for computing the new $|S_{21}|$ distribution. Unit cells which satisfy the new $|S_{21}|$ distribution are designed and associated losses are computed. The process is repeated until the difference between the required and acheived values of $|S_{21}|$ has been minimized. A flow chart for design of unit cells when array losses are included is shown in Fig 4.4. A method for computing the required transmission coefficient of array unit cells from the amplitude distribution and including array losses is given in [14].

The CAD procedure for design of series-fed arrays of gap-coupled patches without cover layer is implemented in program ARSYNT. For the design of the series-fed array of gap-coupled patches, the program makes use of a look-up table containing the dimensions and computed losses of selected two-port patches. The look-up table contains a set of two-port patches having same feed line and patch widths but different values of gap width. A cubic spline interpolation is then used to find the dimensions of the unit cells for desired values of $|S_{21}|$. The CAD procedure for design of series-fed arrays of gap-coupled patches with a cover layer is implemented in program ARSYNTC.

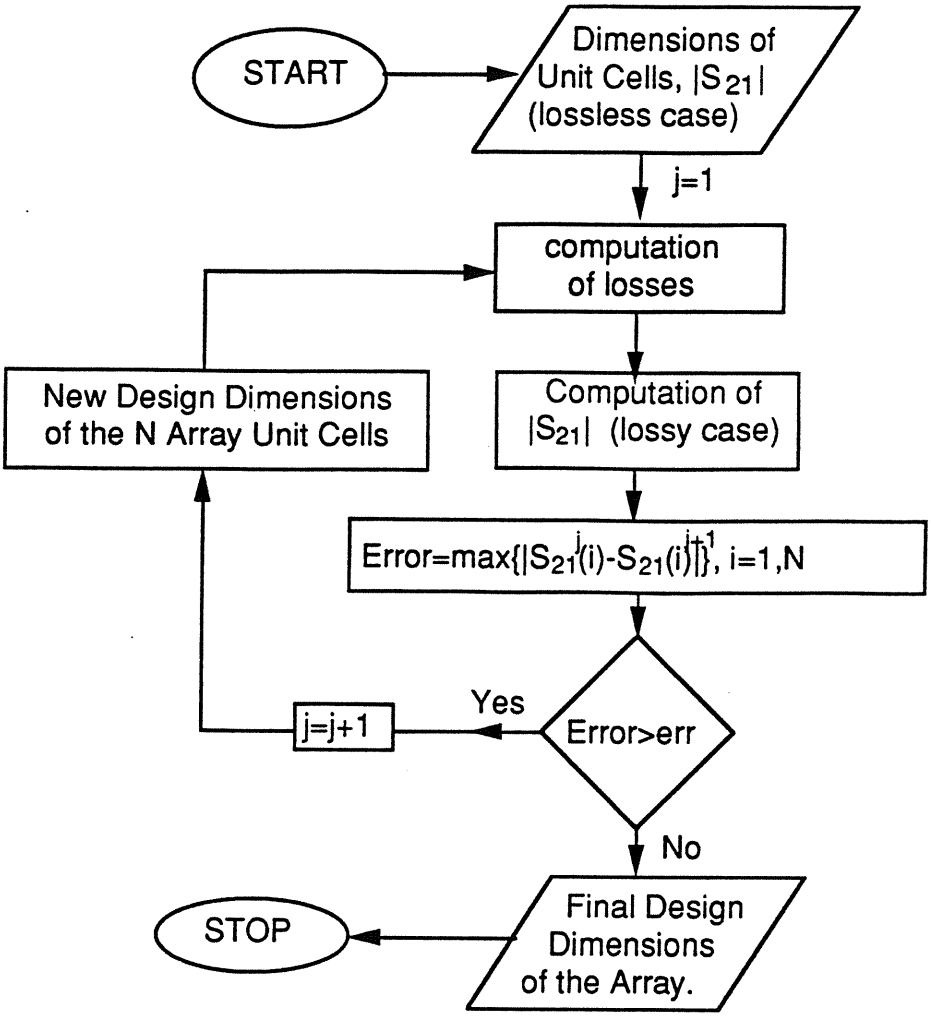

Figure 4.4: Flow chart for the design of unit cells when losses are included

For arrays with a cover layer, we need look-up table containing the values of mutual admittance between two magnetic current elements as a function of their spacing.

4.2 Array Analysis

Once the dimensions of the unit cells which yields the required array amplitude and phase distributions are obtained, the MNM approach is used to compute the Z-matrices of various unit cells. Then the segmentation method is used to combine these Z-matrices of the various unit cells to obtain the (2x2) Z-matrix characterization of the array as well as the input and the output currents at the input and output ports of various unit cells. These currents are needed for computing the voltage distribution along the radiating edges of the patches. The voltage distribution, thus evaluated, is used for the computation of the radiation characteristics of the array. The array analysis approach is similar to that for arrays with directly fed patches given in [14].

To obtain the currents and also the voltages at the ports of the unit cells, the external ports (input ports of the first unit cell and the output port of the last unit cell) and the connected ports (remaining ports) are grouped separately [14]. Using Kirchhoff's voltage and current laws for the connected ports, interconnection matrices for the voltages and the currents are obtained. Then, the application of the segmentation method yields the currents at the connected ports (in terms of currents at the external ports) as well as the Z-matrix characterization of the array with respect to the external ports.

The values of currents at the input and the output ports of the various unit cells are used to related the voltage distributions at the edges of the patches to the currents at the external ports of the array. The radiation characteristics

are obtained from this voltage distribution. This array analysis procedure is implemented in program ARRAY for the arrays without cover layer and in program ARRAYC for arrays with a thick cover layer.

4.3 Design Example and Computational Details

As an example of the use of the array design and analysis procedures described in the previous sections, we consider a 19-element series-fed array with a Taylor distribution. The side lobe levels are to be below -30 dB and the direction of the main beam is to be 30 degrees off-broadside. The operating frequency is 13 GHz. The substrate parameters for the array are: $\epsilon_r = 2.2$, h=1/64 inch, and $tan\delta = 9 \times 10^{-4}$ and without any cover layer. The array is terminated in a matched load with 5% of the input power fed to the array being dissipated in this load.

In this sample array, we select the patches to have the same width (b=3 mm). The width of the interconnecting lines is 0.588 mm (75 Ohms). In order to design the antennas we generate look-up tables for [L] and [C] parameters. The feed line is considered as conductor # 1 and the patch as conductor # 2 of width equal to the length of the patch. In each look-up table, the gap width is kept constant and [L] and [C] parameters are computed for discrete values of patch length 'a' ranging from 6.8 mm to 8.0 mm. Program DESIGN is then used to design sample two-port patches for every value of gap width from 15 mil to 175 mils. The design objective is to calculate (using optimization subroutine) the patch length which maximize the radiation from the patch. Then, the program computes the required load impedance at the output port which yields a real input impedance. Program DESIGN is also used to compute the losses in the patch.

The design of the linear series-fed array (using ARSYNT program) of two-port gap-coupled patches requires generating a look-up table containing the design dimensions and computed performance of sample two-port patches for various values of gap width. The design dimensions are: patch width, patch length, gap width, width of the coupling line. The required computed performance are: dielectric and conductor losses, magnitude and phase of transmission coefficient, required load at the output port for input match and corresponding value of input impedance. Starting from the amplitude distribution, program ARSYNT computes iteratively (including array losses) the required design dimensions of unit cells and required load impedances and corresponding input impedance of each patch. The interconnecting line is made of two sections of lines of different width. For example, the characteristic impedance of the first line section of interconnecting line between elements i and i+1 is selected to be equal to the load impedance at the output port of element #i. The second line section is a quarter-wave transformer to match the input impedance at element #(i+1) to the required load impedance at output of element #i. The length of the second section of interconnecting lines is a quarter wave at the center frequency. The length of the second section is adjusted to yield the required phase distribution.

A layout of the designed linear series-fed array is shown in Figures 4.5 to 4.7. Figure 4.5 shows a layout of the first element and the input matching network. The dimensions of the gap and the width and length of various sections of the matching network are also shown in the figure. The input line section is a 50 Ohms line. Figure 4.6 shows a layout and the dimensions of the last array element. Figure 4.7 shows a layout of two adjacent array elements.

The interconnecting lines are bend in order to accomodate then in the available spacing (half free space wavelength) between adjacent array elements. Values of various parameters shown in Fig. 4.7 are given in Tables 4.1-4.4.

Figures 4.8 and 4.9 show the computed E-plane and H-plane (parallel to the array axis) far-field patterns of the designed array using program ARRAY. The achieved SLL is -28.7 dB (compared to the specified value of -30 dB) and the beam direction is 29.5 degrees off-broadside (compared to the specified value of 30 degrees). The discrepancy between the specified and computed performance may be due to the effect of the element pattern in the H-plane on the linear array pattern.

The computed H-plane far-field patterns of the sample linear array from 12.6 GHz to 13.4 GHz are shown in Figs 4.10 to 4.15. Table 4.5 shows a summary of the computed array performance from 12.6 GHz to 13.4 GHz (6% bandwidth). From the results shown in Table 4.5 we note: i) The reflection coefficient at the input port of the array remains less than -32.77 dB over the frequency range. ii) The scan of the main beam over 3 % bandwidth (12.8-13.2 GHz) is only 3 degrees. iii) The 3% power dissipated in the load (square of $|S_{21}|$) increases rapidly as we move away from resonance. This means that the power being radiated by the array is decreasing as we move away from resonance (lower array efficiency). This is consistent with the results for single gap-coupled patches discussed in Chapter Three.

4.4 Array Sensitivity Analysis

Program ARRAY has also been used for the calculation of the sensitivities of the array performance with respect to various design parameters such as: dielectric constant, elements dimensions, etc. The method consists

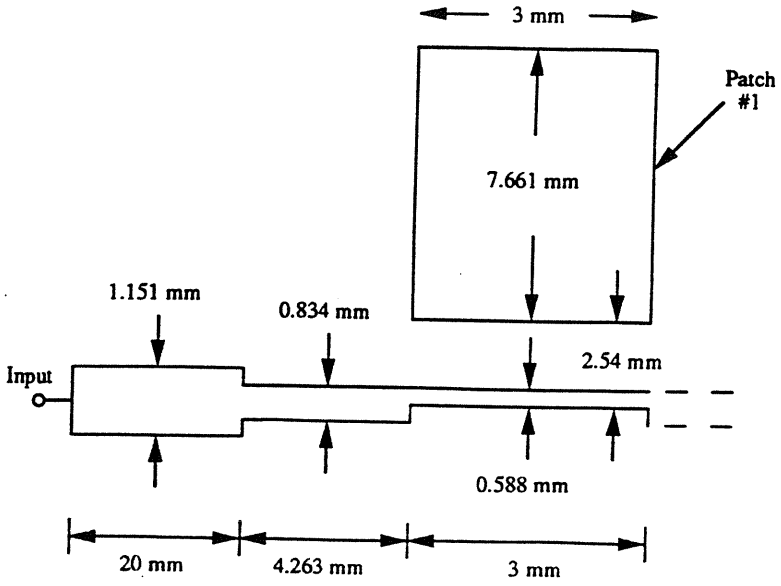

Figure 4.5. Design dimensions of first patch and input quarter-wave transformer

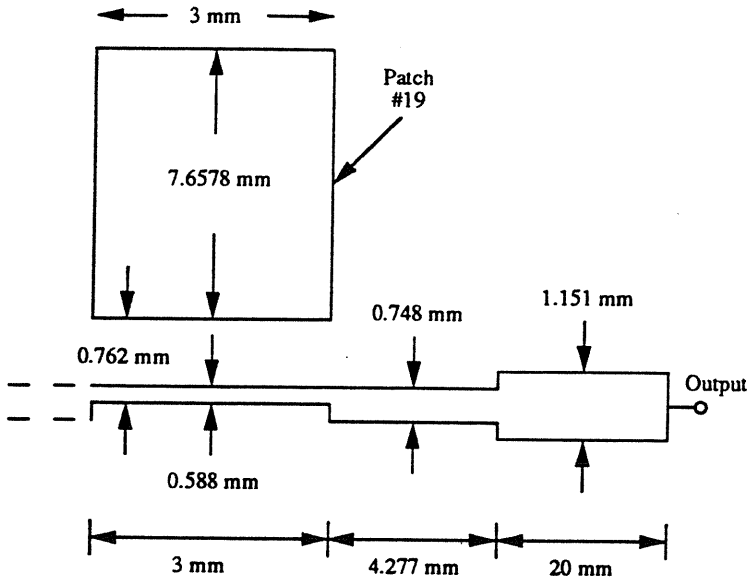

Figure 4.6. Design dimensions of last patch and output quarter-wave transformer

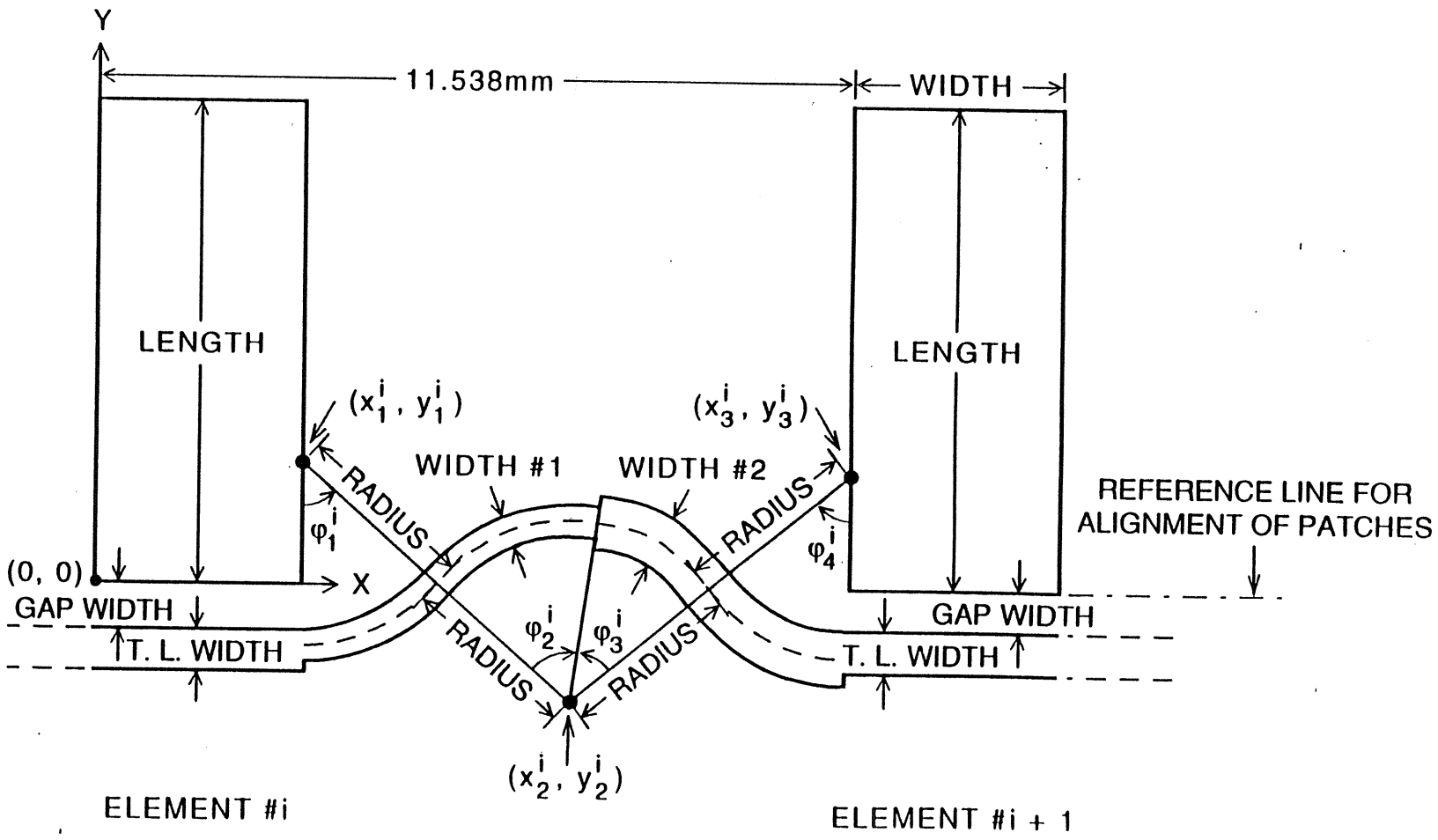

Figure 4.7: Layout of two adjacent array elements

Table 4.1: Design dimensions of gap-coupled rectangular patches

Patch #	Length (mm)	Width (mm)	Gap Width (mm)	Feed Line Width (mm)
1	7.661	3.0	2.540	0.588
2	7.662	3.0	2.263	0.588
3	7.662	3.0	1.834	0.588
4	7.661	3.0	1.462	0.588
5	7.660	3.0	1.186	0.588
6	7.659	3.0	1.008	0.588
7	7.658	3.0	0.883	0.588
8	7.658	3.0	0.767	0.588
9	7.656	3.0	0.681	0.588
10	7.652	3.0	0.619	0.588
11	7.650	3.0	0.5705	0.588
12	7.649	3.0	0.533	0.588
13	7.648	3.0	0.5077	0.588
14	7.647	3.0	0.4945	0.588
15	7.647	3.0	0.4993	0.588
16	7.649	3.0	0.5378	0.588
17	7.652	3.0	0.6191	0.588
18	7.657	3.0	0.7152	0.588
19	7.658	3.0	0.7617	0.588

Table 4.2: Design dimensions of interconnecting lines (dimensions are in mm)

Interconnecting Line #	Width #1	Width #2	Radius
1 - 2	0.5793	0.5824	2.6465
2 - 3	0.5769	0.5847	2.6531
3 - 4	0.5701	0.5881	2.6506
4 - 5	0.5582	0.5914	2.6475
5 - 6	0.5379	0.5924	2.6414
6 - 7	0.5155	0.5937	2.6388
7 - 8	0.4862	0.5950	2.6318
8 - 9	0.4549	0.5947	2.6328
9 - 10	0.4200	0.5905	2.6205
10 - 11	0.3832	0.5851	2.6094
11 - 12	0.3463	0.5764	2.5977
12 - 13	0.3135	0.5651	2.5865
13 - 14	0.2888	0.5537	2.5773
14 - 15	0.2756	0.5412	2.5715
15 - 16	0.2806	0.5775	2.5721
16 - 17	0.3181	0.5250	2.5847
17 - 18	0.3826	0.5432	2.606
18 - 19	0.4359	0.5668	2.622

Table 4.3. Values of coordinates of origin of curved sections of interconnecting lines

Element #	(x1, y1) mm	(x2, y2) mm	(x3, y3) mm
1 - 2	(3.00 , 0.183)	(7.369 , -3.169)	(11.538 , 0.092)
2 - 3	(3.00 , 0.101)	(7.426 , -2.826)	(11.538 , 0.527)
3 - 4	(3.00 , 0.532)	(7.402 , -2.421)	(11.538 , 0.895)
4 - 5	(3.00 , 0.906)	(7.364 , -2.092)	(11.538 , 1.165)
5 - 6	(3.00 , 1.186)	(7.324 , -1.848)	(11.538 , 1.337)
6 - 7	(3.00 , 1.373)	(7.301 , 1.686)	(11.538 , 1.459)
7 - 8	(3.00 , 1.506)	(7.291 , -1.542)	(11.538 , 1.567)
8 - 9	(3.00 , 1.633)	(7.275 , -1.424)	(11.538 , 1.649)
9 - 10	(3.00 , 1.729)	(7.261 , -1.323)	(11.538 , 1.705)
10 - 11	(3.00 , 1.798)	(7.251 , -1.229)	(11.538 , 1.746)
11 - 12	(3.00 , 1.854)	(7.242 , -1.145)	(11.538 , 1.777)
12 - 13	(3.00 , 1.897)	(7.235 , -1.074)	(11.538 , 1.796)
13 - 14	(3.00 , 1.925)	(7.229 , -1.022)	(11.538 , 1.806)
14 - 15	(3.00 , 1.939)	(7.232 , -0.996)	(11.538 , 1.802)
15 - 16	(3.00 , 1.932)	(7.215 , -1.017)	(11.538 , 1.771)
16 - 17	(3.00 , 1.888)	(7.206 , -1.117)	(11.538 , 1.703)
17 - 18	(3.00 , 1.796)	(7.208 , -1.280)	(11.538 , 1.649)
18 - 19	(3.00 , 1.689)	(7.229 , -1.412)	(11.538 , 1.577)

Table 4.4: Values of angles of curved sections of interconnecting lines

Interconnecting Line #	ϕ_1°	ϕ_2°	ϕ_3°	ϕ_4°
1 - 2	55.65	66.29	41.31	51.96
2 - 3	56.52	65.11	42.22	50.81
3 - 4	56.14	65.60	41.81	51.28
4 - 5	55.51	66.38	41.16	52.03
5 - 6	54.94	67.36	40.49	52.92
6 - 7	54.58	67.92	40.08	53.42
7 - 8	54.61	66.47	39.94	53.79
8 - 9	54.43	68.97	39.67	54.20
9 - 10	54.38	69.64	39.45	54.71
10 - 11	54.54	70.43	39.35	55.24
11 - 12	54.74	71.25	39.27	55.78
12 - 13	54.95	72.03	39.22	56.30
13 - 14	55.13	72.67	39.18	56.73
14 - 15	55.20	73.09	39.15	57.04
15 - 16	55.02	73.16	39.04	57.19
16 - 17	54.45	72.55	38.84	56.93
17 - 18	53.831	71.32	38.71	56.19
18 - 19	53.75	70.46	38.96	55.25

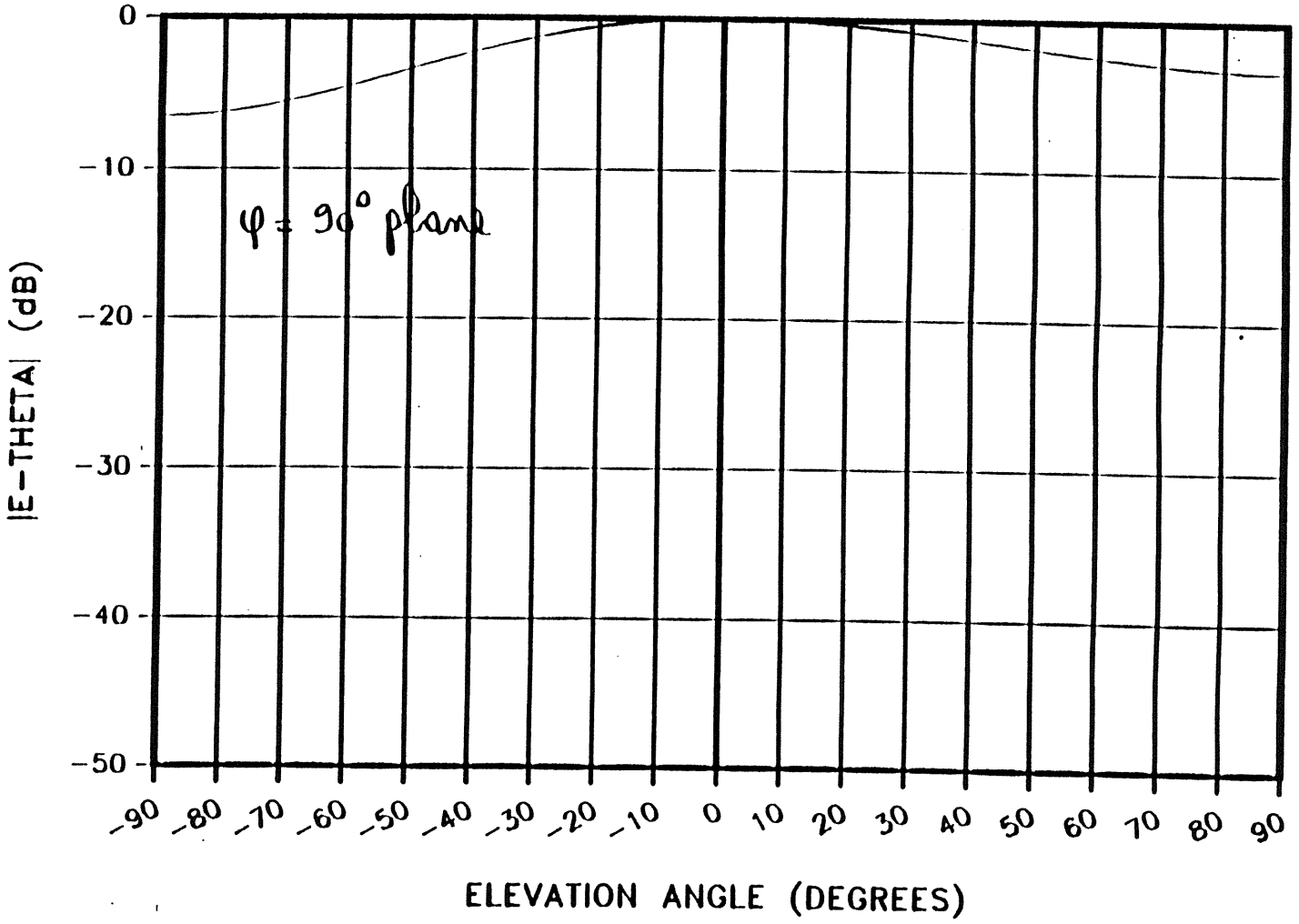

19-element array:
- Taylor Distribution:
- 30 dB SLL
- $\theta_0 = -30°$
- BW = 125°
- $\varepsilon_r = 2.2$
- h = 1/64"
  13 GHz

Figure 4.8. E-plane far-field pattern of 19-elements series-fed array of gap-coupled patches

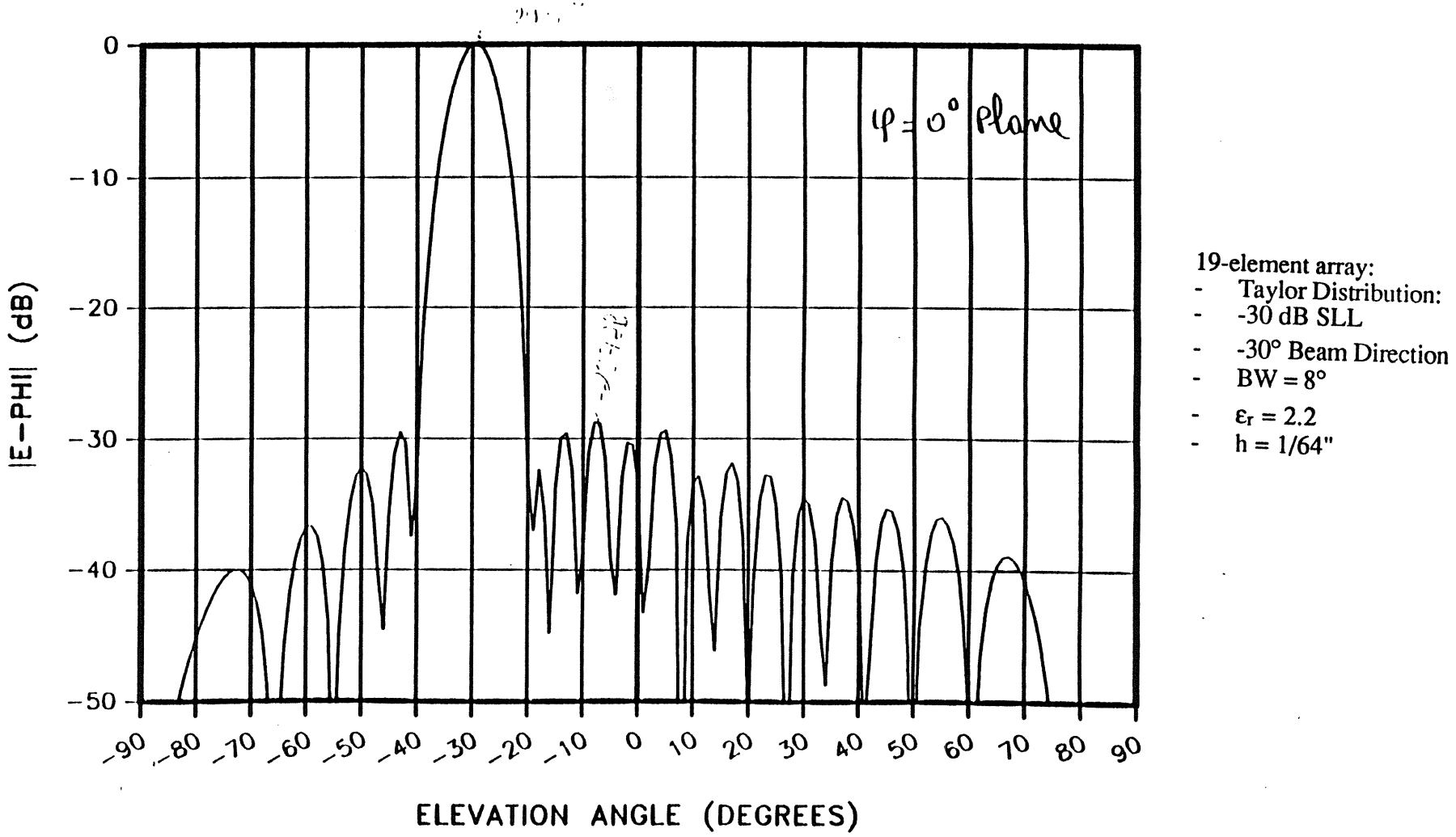

Figure 4.9. H-plane far-field pattern of 19-elements series-fed array of gap-coupled patches

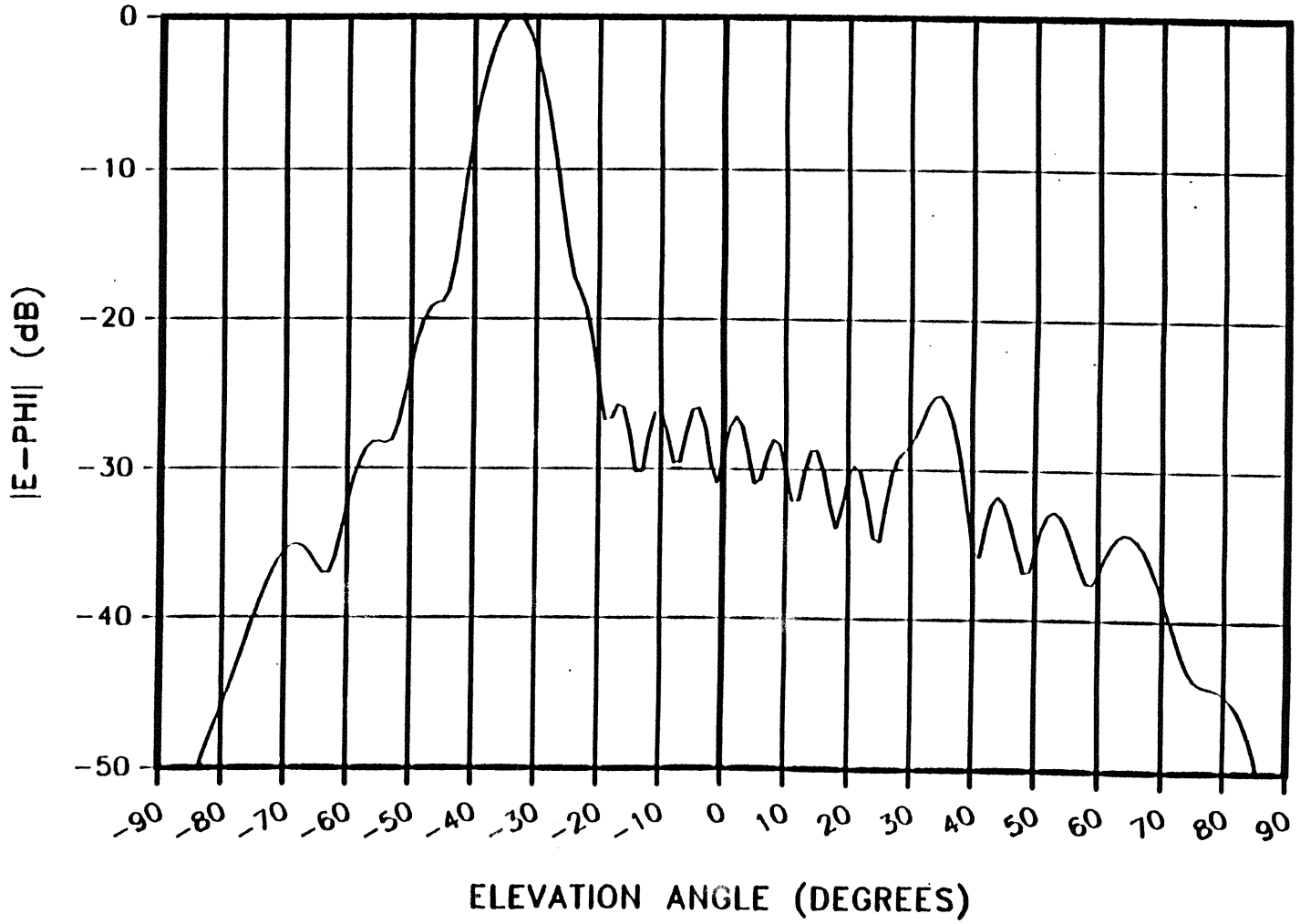

Figure 4.10. H-plane far-field pattern of 19-elements series-fed array of gap-coupled patches (f=12.6 GHz)

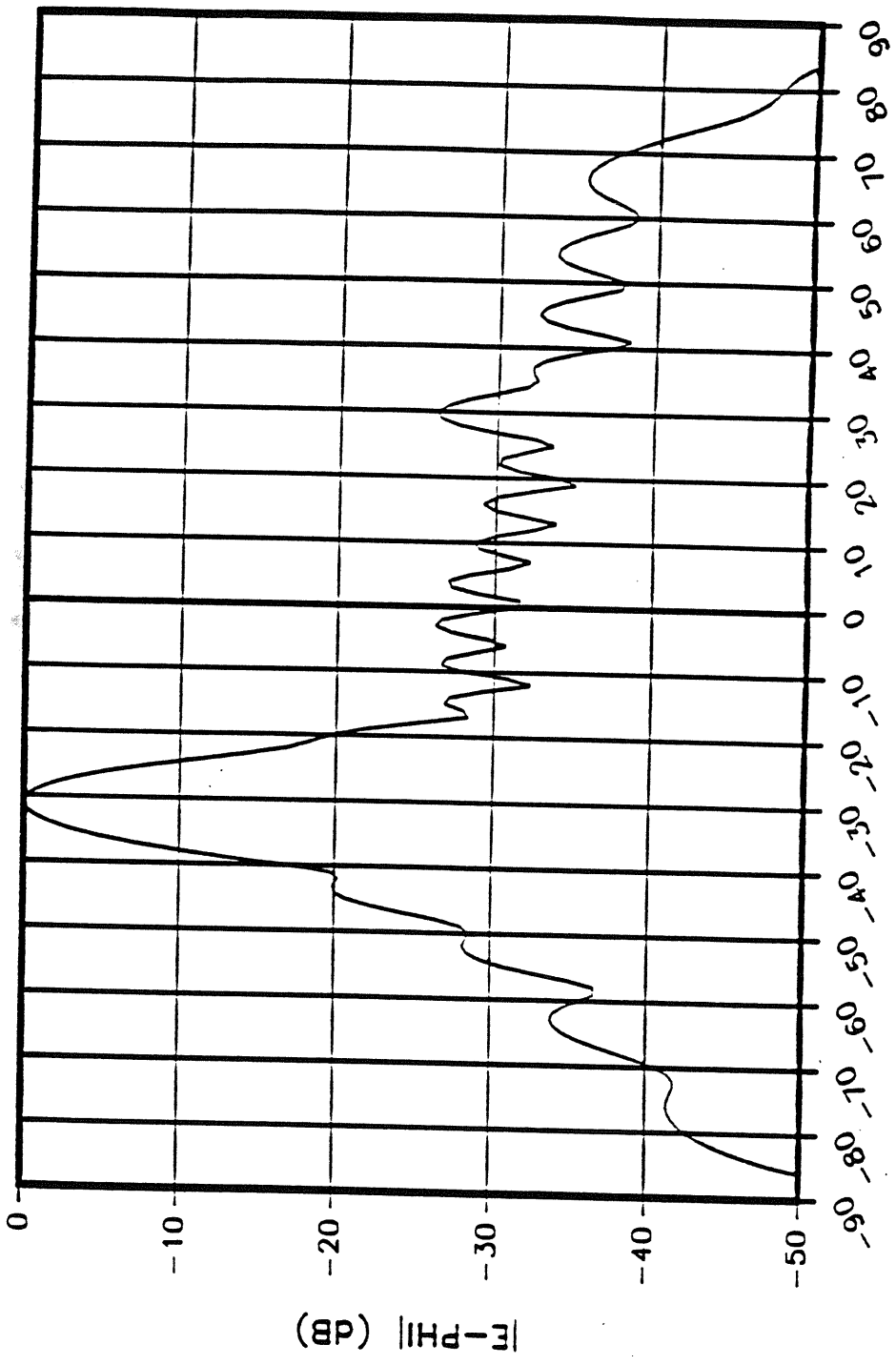

Figure 4.11. H-plane far-field pattern of 19-elements series-fed array of gap-coupled patches (f=12.8 GHz)

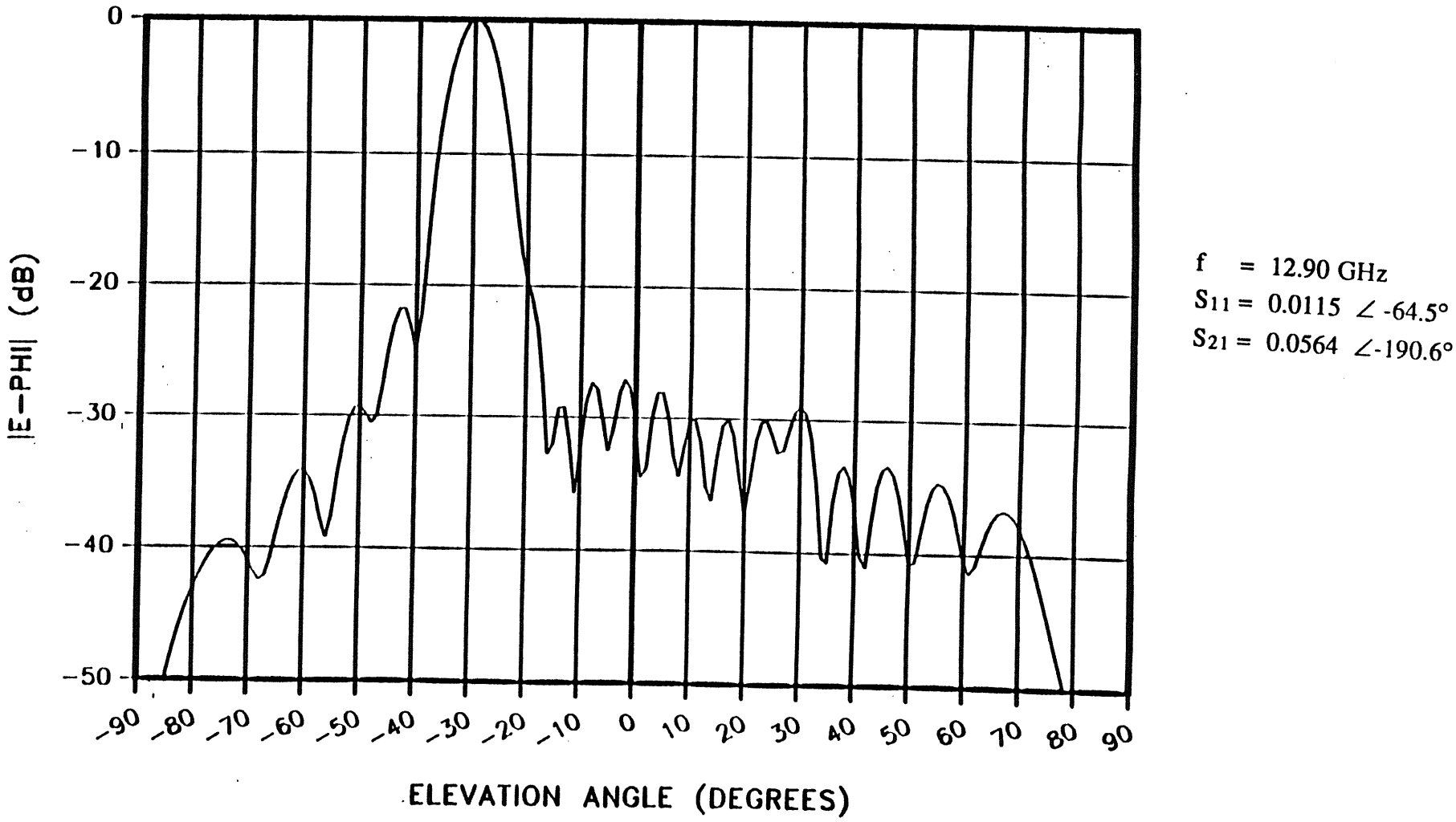

Figure 4.12. H-plane far-field pattern of 19-elements series-fed array of gap-coupled patches (f=12.9 GHz)

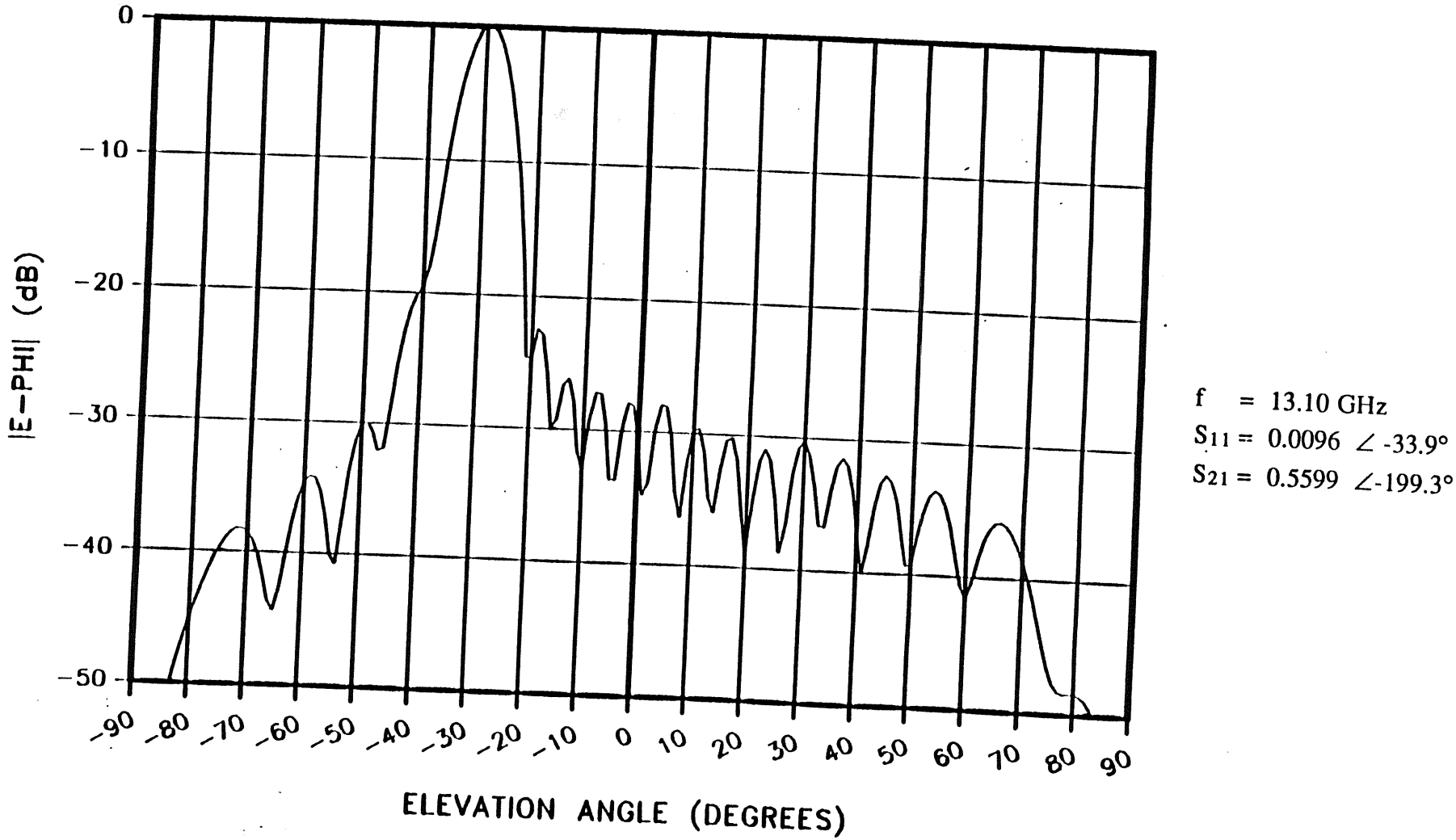

Figure 4.13. H-plane far-field pattern of 19-elements series-fed array of gap-coupled patches (f=13.1 GHz)

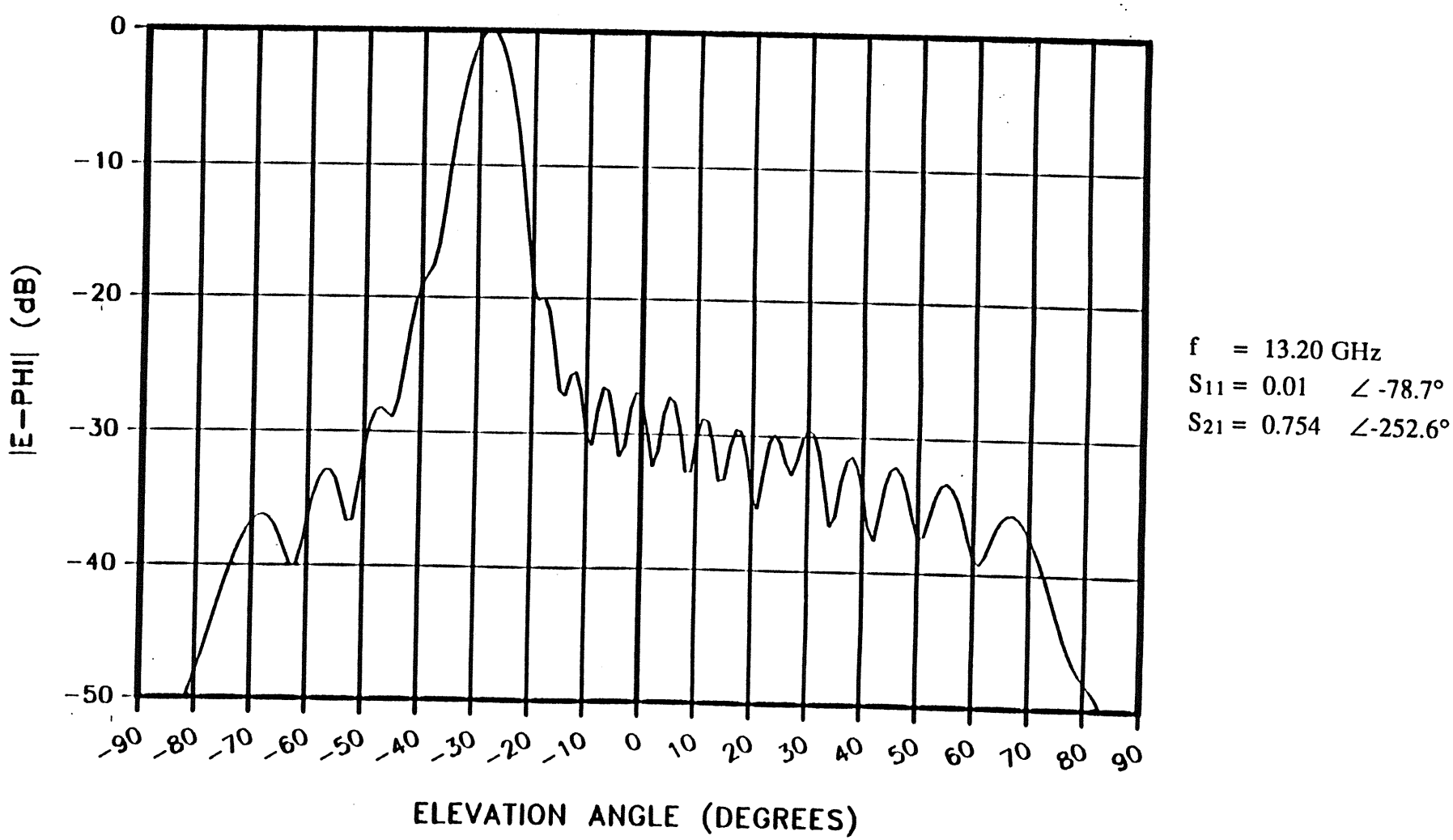

Figure 4.14. H-plane far-field pattern of 19-elements series-fed array of gap-coupled patches (f=13.2 GHz)

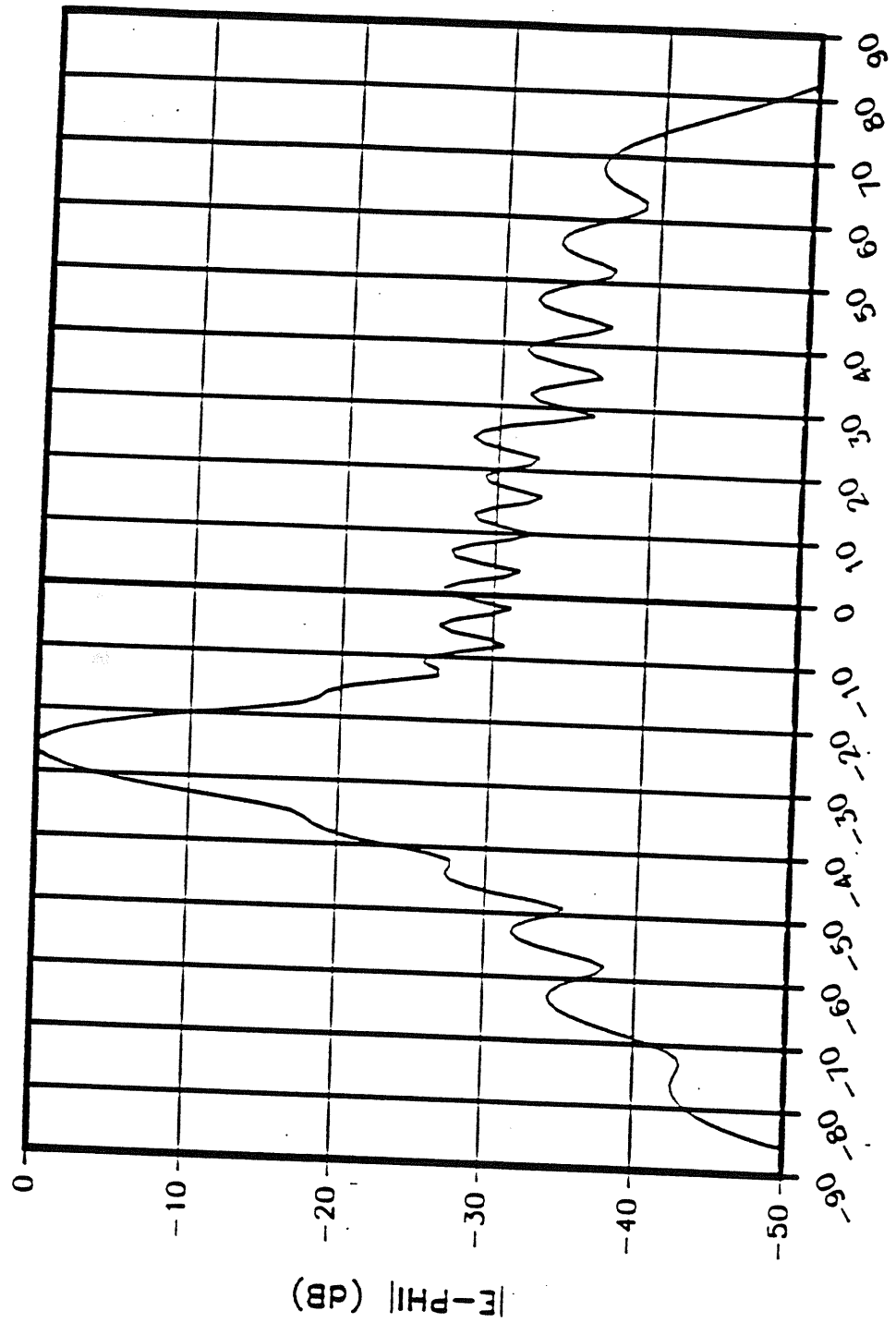

Figure 4.15. H-plane far-field pattern of 19-elements series-fed array of gap-coupled patches (f=13.4 GHz)

Table 4.5. Summary of calculated performance of the 19-element series-fed array of gap-coupled rectangular patches

F (GHz)	|S11| (dB)	Beam Direction	SLL (dB)	SLL* (dB)	|S21| (dB)
12.60	-32.77	-33.5°	-25.0	-17.0	-1.53
12.80	-36.54	-31.0°	-26.0	-19.0	-2.45
12.90	-38.78	-30.0°	-27.0	-22.0	-4.97
13.00	-44.88	-29.5°	-29.0	—	-13.0
13.10	-40.35	-29.0°	-23.0	-20.0	-5.04
13.20	-40.00	-28.0°	-26.0	-19.0	-2.45
13.40	-34.00	-26.0°	-26.0	-18.0	-1.55

* Close-in side lobe has emerged with main beam.

of evaluations of the array performance when the nominal values are slightly modified. A summary of normal array performance is given in Table 4.5.

4.4.1 Uncertainty in dielectric constant: Because of the narrow bandwidth of series-fed arrays of gap-coupled patches, the value of the substrate dielectric constant is a critical parameter in the design. Table 4.6 shows the effect of 1% increase in the value of dielectric constant on the array performance. The main effect is an increase in SLL and a shift in beam direction. It may be pointed out that a 1% increase in dielectric constant will cause the resonance frequency of patches to decrease by 0.5 % which should shift the center frequency of the array from 13 GHz to 12.935 GHz.

4.4.2 Uncertainty in elements dimensions: The measured dimensions of the array after fabrication are usually different from the designed dimensions. Table 4.7 shows the effect of 0.5 mil under-etching (1 mil increase in patch widths, patch lengths and widths of interconnecting lines and 1 mil decrease in gaps widths). As shown in Table 4.7, the effect consists of an increase in the side lobe level to -25 dB and a shift of main beam direction to -29 degrees. Again, a 1 mil increase in patch length lowers the resonance frequencies of the patches.

4.4.3 Uncertainty in [L] and [C] parameters: In the MNM approach, discussed in Chapter Three, the gap region between the feed lines and the patch is modeled in terms of a gap network. This network is characterized in terms of an admittance matrix. The admittance matrix consists of a capacitive part which accounts for the coupling due to the electric fields and an inductive part which accounts for the coupling due to the magnetic fields. The elements of the capacitive and inductive parts are computed from [C] and [L] parameters

Table 4.6. Effect of a 1% increase in dielectric constant on the performance of the 19-element array

Frequency (GHz)	|S11| (dB)	|S21| (dB)	SLL (dB)	Beam Direction
12.8	-35.2	-2.08	-18.0	-31.5°
13.0	-49.6	-9.37	-25.0	-28.0°
13.2	-40.4	-3.24	-18.5	-28.0°

of the corresponding coupled line configuration. Table 4.8 shows the effect of a 5 % increase in [C] parameters and 5 % decrease in [L] parameters. As shown in this table, this results in increases in SLL and the values of $|S_{11}|$ and $|S_{21}|$.

Table 4.7. Effect of a 1 mil increase in arrays dimensions and 1 mil decrease in gaps widths

Frequency (GHz)	|S11| (dB)	|S21| (dB)	SLL (dB)	Beam Direction
12.8	-39.84	-3.33	-18.0	-30.0°
13.0	-40.93	-10.1	-25.0	-29.0°
13.2	-45.3	-2.14	-18.0	-27.0°

Table 4.8. Effect of a 5% increase in [C] and 5% decrease in [L] on the performance of the 19-element array

Frequency (GHz)	|S11| (dB)	|S21| (dB)	SLL (dB)	Beam Direction
12.8	-33.57	-1.63	-18.0	-32.0°
13.0	-26.40	-1.37	-18.0	-30.0°
13.2	-35.49	-1.29	-18.5	-28.0°

CHAPTER 5

CONCLUDING REMARKS

A summary of the work described in this report is presented in this chapter.

5.1 Directly-Fed Patch

The analysis and the design of the directly-fed patch (shown in Figure 1.3) can be carried out using the MNM approach already developed in [6]. An approximate transmission line model has been presented in Chapter 2. Based on this model, computed performance of the patch is given. Results show that this configuration is not very suitable for array elements with very small values of fractional radiated power.

5.2 Gap-Coupled Patch

The multiport network model [6] has been extended to the analysis and design of gap-coupled patch shown in *Fig.* 1.2. Details of this modeling approach are given in Chapter 3. The modeling of the gap in terms of a multiport network model consisting of inductive and capacitive parts has been presented. The elements of the gap network are computed by modeling the gap-coupled configuration in terms of an asymmetric coupled line. [L] and [C] matrices of the asymmetric coupled line are evaluated using the software package in [12]. A flow chart depicting a step-by-step design approach for the

patch has also been given. A good agreement among MNM approach, full-wave method and experiment for a gap-coupled rectangular microstrip patch without a cover layer was obtained. A good agreement has also been obtained between MNM and full-wave analysis for a gap-coupled patch with a cover layer.

5.3 Series-fed arrays of gap-coupled patches

In Chapter Four, a computer-aided design and analysis procedure for linear series-fed arrays of gap-coupled patches (with and without a cover layer) has been described. The approach is similar to that used for series-fed arrays of directly-fed patches discussed in [14]. A software package for series-fed arrays, based on MNM approach, has been implemented on VAX. The software has been used for the design of a sample array of gap-coupled patches without a cover layer.

BIBLIOGRAPHY

[1] M. Danielsen and R. Jorgensen, 'Frequency scanning microstrip antennas,' IEEE Trans. Antennas Propagat., Vol. AP-27, pp. 146-150, March 1979

[2] T. Metzler, ' Microstrip series arrays', IEEE Trans. Antennas & Prpagation Vol. AP-29 No. 1, 1981.

[3] B. B. Jones, et al., 'The syntheses of shaped patterns with series-fed microstrip arrays', IEEE Trans. Antennas & Prpagation Vol. AP-30 No. 6, 1982.

[4] A. Benalla and K. C. Gupta, 'Design of a low side lobe level short series-fed linear arrays of microstrip patches', Electromagnetic Lab. Scientific Report No. 93, University of Colorado at Boulder, Oct. 1987.

[5] J. R. James, P. S. Hall and C. Wood, 'Microstrip antenna theory and design,' Peter Pereginus, London, 1981.

[6] A. Benalla and K. C. Gupta, 'Multiport network model and transmission characteristics of two-port rectangular microstrip patch antenna,' IEEE Trans. Antenna Propagation, Vol. AP-33, 1988, pp. 1337-13342.

[7] T. Okoshi, 'Planar circuits for microwave and lightwave,' Spring Verlag, Berlin, 1985.

[8] M. Kirshning, R.H. Jansen and N.H.L. Koster, 'Accurate model for open end effects of microstrip lines,' Electron. Lett., 1981, 17, pp. 123-125.

[9] E. Hammerstad and O. Jansen, 'Accurate models for microstrip computer-aided design,' 1980 IEEE MTT-S International Microwave Symposium Digest, Washington , 1980, pp 407-409.

[10] A. Benalla and K.C. Gupta, 'Multiport network approach for modeling the mutual coupling effects in microstrip patch antennas and arrays,' IEEE Trans. Antennas Propagat., Vol. AP-37, pp. 148-152. Feb. 1989.

[11] R. P. Jedlicka et al., 'Measured mutual coupling between microstrip antennas,' in Proc. Workshop Printed Circuit Antenna Technolo., Las Cruces, NM, Oct. 17-19, 1979, pp. 4.1-4.19

[12] A. Djordjevic et al., 'Matrix parameters for multiconductor transmission lines, Software and Users Manual,' Artech House, Inc. Norwood, MA, 1989.

[13] B. Bhat and S. K. Koul, 'Unified approach to solve a class of strip and microstrip like trnamsission lines', IEEE Trans. Microwave Theory and Techn., Vol. MTT-30, No. 5, May 1982.

[14] A. Benalla and K. C. Gupta, 'Design procedure for a linear series-fed array of microstrip patches covered with a thick dielectric layer', EM Lab. Scientific Report No. 100, University of Colorado at Boulder, Sept. 1989.

[15] W. H. Press et al., 'Numerical Recipes; The art of scientific computing', Cambridge University Press, 1988.

[16] A. Benalla and K. C. Gupta, 'Faster computation of Z-matrix for rectangular segments in planar microstrip circuits,' IEE Trans. Microwave Theory and Techniques, Vol. MTT-34, June 1986, pp. 733-736.

[17] I. Wollf and N. Knoppik, 'Rectangular and circular microstrip disk capacitors and resonators', IEEE Trans. Microwave Theory Techn., Vol. MTT-22, pp. 857-864, Oct. 1974.

[18] D. I. Wu et al., 'A highly accurate numerical modeling of microstrip junctions and discontinuities', Final Report, MIMICAD Center, University of Colorado, Boulder, 1990.